Fabrication, Structure, and Electron Emission of Single Carbon Nanotubes

Gongpu Zhao

A dissertation submitted to the faculty of the University of North Carolina at Chapel Hill in partial fulfillment of the requirements for the degree of Doctor of Philosophy in the Department of Physics and Astronomy.

Chapel Hill
2006

Approved by

Advisor: Professor Lu-Chang Qin

Reader: Professor Alfred Kleinhammes

Reader: Professor Paul Tiesinga

Reader: Professor Frank Tsui

Reader: Professor Otto Zhou

ABSTRACT

GONGPU ZHAO: Fabrication, Structure, and Electron Emission of Single Carbon Nanotubes

(Under the direction of Professor Lu-Chang Qin)

Carbon nanotubes possess many excellent field emission properties. An obstacle to these applications is that there is no simple and reproducible method to prepare a single carbon nanotube field emitter. In this dissertation, individual carbon nanotube field emitters have been fabricated in a two-step process involving (a) producing micron-size carbon fibers which contain single carbon nanotubes at their cores and (b) exposing the nanotubes by fracturing the fiber with mechanical forces and mounting the fiber to a copper ribbon with a groove. This fabrication method has the potential to be the production method for single carbon nanotube field emission point electron sources.

The cold field emission properties of single carbon nanotubes have been studied. These carbon nanotubes exhibit large field enhancement factors of 1.1×10^{7} m^{-1} and low turn-on fields of 1.1 V/μm. An empirical model has been developed to calculate the field enhancement factor of an open end nanotube attached on a carbon fiber. The lifetime measurements show that a single carbon nanotube can continuously emit electrons over 100 hours without significant current drops. The emission stability measurements show that the maximum current drift is 3.6%. It is also shown experimentally that a carbon nanotube has a

high reduced brightness 2.9×10^{8} $ASr^{-1}m^{-2}V^{-1}$, which is two orders of magnitude higher than those of the thermionic electron sources.

The thermal field emission properties of a single carbon nanotube have been systemically studied. It is found that there is a gap between the intermediate region and the field emission region which is not covered by either the Fowler-Nordheim theory or the Murphy-Good theory. We have developed an analytical equation that describes the thermal field emission behavior of a single carbon nanotube within the gap. The experimental results agree well with the theoretical predictions.

We also studied the effect of Cs doping on the field emission properties and electronic properties of a single nanotube. We found that the work function of the carbon nanotube was reduced from 4.8 eV to 3.7 eV by Cs doping.

ACKNOWLEDGEMENTS

I would like to express my deepest gratitude to my advisor Professor Lu-Chang Qin, who has provided me guidance and great encouragement. His encouragement has helped me go through a lot difficulties I met in the research and gives me the confidence to continue pursuing my career in physics. I want to extend my special thanks to Dr. Qi Zhang who has taught me how to use the transmission electron microscope. I also want to thank my group members, Zejian Liu, Han Zhang, Hakan Deniz, and Chengyan Xu, who have supported me all the time and shared valuable research ideas with me.

I also want to extend my special thanks to Professor Otto Zhou who has kindly allowed me to work in his laboratory to perform field emission measurements. He also has given me valuable instructions to my research. I also want to thank my entire committee, Professor Kleinhammes, Professor Jianping Lu, Professor Paul Tiesinga, Professor Frank Tsui, Professor Sean Washburn, Professor Yue Wu for their support.

TABLE OF CONTENTS

Chapter 1. Introduction

Carbon nanotubes have attracted intense attention in both scientific and industrial communities since their discovery [1]. These nanometric size structures have shown excellent mechanical properties and unique electrical properties. All researches have suggested that carbon nanotubes could be used as future high strength materials, field emission elements, field transistors and biosensors.

1.1 Structure

The electronic properties of a carbon nanotube depend strongly on its geometry structure. Therefore it is important to understand the geometry of carbon nanotubes [2,3,4,5]. A single wall carbon nanotube (SWNT) can be treated as one graphene sheet which is wrapped seamless around a chosen tubule axis. A chiral vector C_h

$$C_h = u\mathbf{a_1}+v\mathbf{a_2} \tag{1.1.1}$$

can be used to describe a carbon nanotube (Fig.1.1.1). The chiral vector is drawn between two equivalent points in the graphene sheet making an angle with the zigzag direction. A nanotube is formed by rolling the sheet into a tube with the chiral vector along the circumference, connecting the identical lattice points at both ends. A nanotube with indices (n, 0) is called a zigzag tube and it has chiral angle of 0°. A nanotube with indices (n, n) is called an armchair nanotube and it has a chiral angle of 30°. The 30° wedge of the graphene

sheet lies between the zigzag and armchair chiral vectors is called the 'irreducible wedge' [6]. This 30° wedge can cover all unique nanotube chiralities. The chiral angle of a nanotube of indices (u, v) is

$$\theta = \tan^{-1}[\frac{\sqrt{3}v}{v+2u}]. \tag{1.1.2}$$

The nanotube has a diameter $d=|C_h|/\pi$ and it can be expressed as

$$d = \sqrt{3}a_{C-C}\sqrt{u^2+v^2+uv}/\pi, \tag{1.1.3}$$

where $a_{C\text{-}C}$ is the carbon-carbon bond length (1.421 Å).

It is also important to find the periodicity along the tube axis, which is the minimum repeat distance defined by a translational vector T:

$$T = t_1\mathbf{a_1}+t_2\mathbf{a_2}, \tag{1.1.4}$$

where t_1, t_2 are related to u, v by

$$t_1 = \frac{2v+u}{d_R}, \tag{1.1.5}$$

$$t_2 = -\frac{2u+v}{d_R}, \tag{1.1.6}$$

and d_R is the greatest common divisor of $(2u+v)$ and $(2v+u)$.

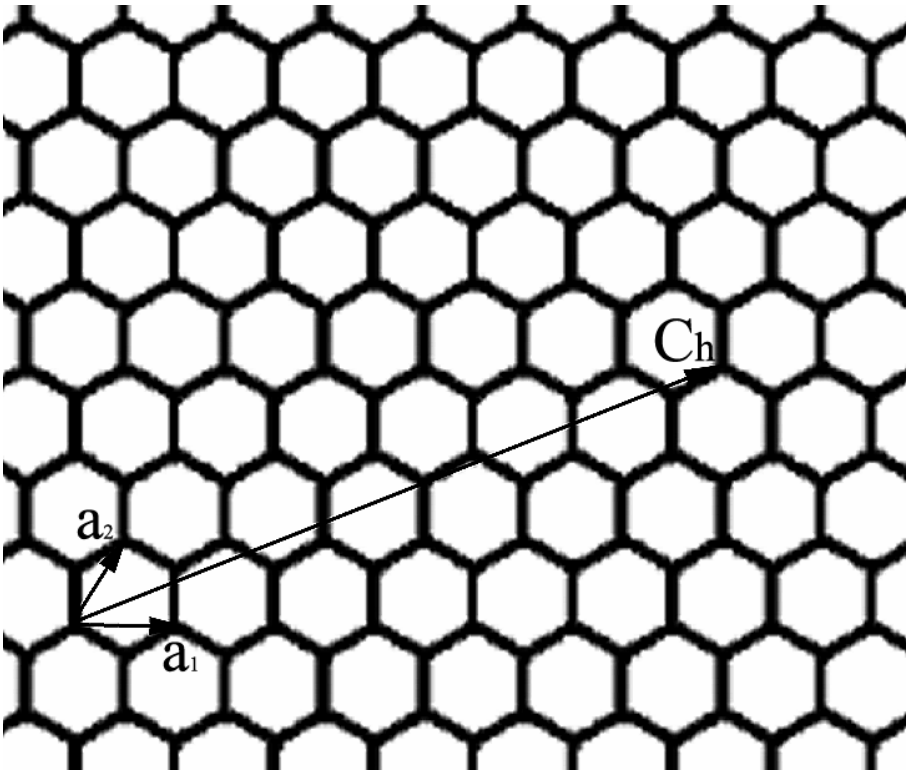

Fig. 1.1.1. The unrolled graphene layer and the chiral vector C_h which define a (5, 3) nanotube.

1.2 Electronic Properties

One fascinating aspect about a carbon nanotube is that its electronic properties directly depend on its one dimensional structure [7]. For a single wall carbon nanotube, the electronic wave function in the radial direction is confined by the monolayer thickness of the nanotube. The periodic boundary conditions for a 1D carbon nanotube of small diameter only permit a few wave vectors to exist in the circumferential direction and these wave vectors k_1 satisfy the relation $n\lambda=\pi d_t$, where $\lambda=2\pi/k_1$ is the de Broglie wave length and n = 1, 2, …, N. The electronic structure of a SWNT can be understood on the basis of the electronic structure of a graphene sheet, which is a zero gap semiconductor with the π and π* bands that are degenerate at the K-point (zone corner) of hexagonal Brillouin zone [8]. The one dimensional energy dispersion relation of a single wall carbon nantube is given by [9]:

$$E_{\mu}(k_2) = E_{g2D}(k_2 \frac{K_2}{|K_2|} + nK_1), \tag{1.2.1}$$

where K_1 denotes a discrete reciprocal unit wave vector along the circumferential direction and K_2 denotes a reciprocal lattice vector along the tube axis direction. For each discrete K_1 vector, a continuous wave vectors k_2 along the tube axis can be defined. So the energy dispersion curves will be a series of parallel lines which is discrete in the K_1 direction and continuous in the K_2 direction . When (u, v) satisfy the condition of $2u + v = 3q$, where q is an integer, one $k_2K_2/|K_2| + n K_1$ line will pass the K-point of the 2D Brillouin zone, where the π and π* bands are degenerate. Then the one dimensional energy bands have a zero energy gap and this nanotube will be metallic. If $2u + v \neq 3q$, no $k_2K_2/|K_2| + n K_1$ lines will pass through the K-point, and the one-dimensional energy bands will have a nonzero band gap, then this nanotube will be semiconducting [9, 10]. As the nanotube diameter increases,

more wave vectors become allowed in the circumferential direction, so that the nanotube becomes more two dimensional and the semiconducting gap starts to disminish.

The 1D electronic density of states shows sharp singularities due to the $(E-E_0)^{-1/2}$ van Hove singularities about every subband edge at energy E_0. For metallic nanotubes, there is a small, but non-vanishing density of states at the Fermi level and this density of states is independent of energy until the energies of the first subband edges of the valence and conduction band are reached. For semiconducting nanotubes, the density of states is zero through the band gap. The band gap energy equals to the energy difference (E_{11}) between the two van Hove singularities near the Fermi level (Fig.1.2.1). The band gap energy for a single wall semiconducting nanotube can be expressed as $E_g = 2\gamma_0 a_{C-C} / d$, where $\gamma_0 = 3.0 \pm 0.2$ eV is the nearest neighbour overlap energy [9]. For metallic SWNTs, the energy difference between the first two van Hove singularities $E^M{}_{11} = 6\gamma_0 a_{C-C} / d$ [9]. For all the SWNTs whose diameters d fall in the range $0.7 < d < 3.0$ nm, energy differences $E_{ii}(d)$ have been calculated and shown in reference 10 using $\gamma_0 = 2.9$ eV.

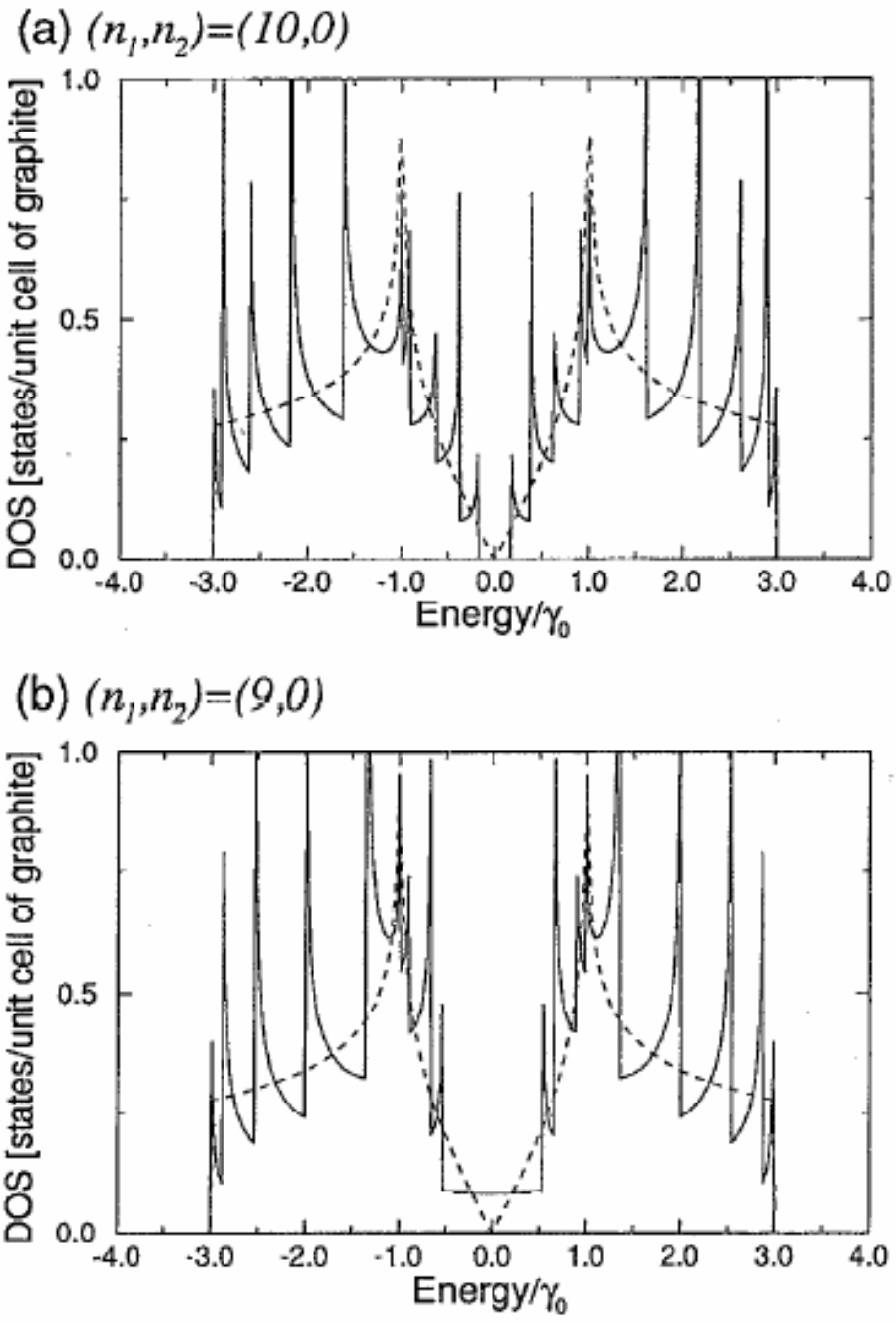

Fig. 1.2.1. (a) The calculated density of states for the (10, 0) tube. (b) The calculated density of states for the (9, 0) tube. Adapted from reference [4].

1.3 Synthesis

Since carbon nanotubes were discovered in 1991, different synthesis techniques have been widely explored during the past fifteen years. There are three major synthesis methods: arc-discharge, laser ablation and chemical vapor deposition (CVD). Each method has been optimized for SWNTs production and has its own merits.

The arc-discharge method has been proved to be a good method to produce SWNTs. The apparatus used to synthesize SWNTs is basically the same as that used to produce fullerenes. For example, a 4.2 % Ni and 1 % Y combination of catalysts was put in a small hole drilled in the center of a graphite anode and then arc-discharges were conducted by a 100 A current. In the reaction chamber, helium atmosphere was maintained at about 500 Torr [11]. The SWNTs produced by the arc-discharge method are similar to those produced by the laser ablation method. The collected carbon soots contain a large quantity of SWNT bundles.

Laser ablation was first developed by Smalley's group at Rice University in 1995 [12]. A tablet composed of graphite powders and metal catalysts is prepared first. Then a high power laser beam is used to scan the tablet surface to vaporize carbon and metal atoms. This method mainly produces single wall nanotube (SWNT) bundles. There are several parameters that can be adjusted to control the average diameter, yield, quality and purity. The yield increases with temperature and so does the diameters of SWNTs [13]. Also the catalysts have a great effect on the yield and quality. Bi-metallic catalysts perform better than single metal catalysts. Several bi-metallic catalysts have been widely studied. Ni/Y, Ni/Co, Pt/Rh, Ni/Fe all produce SWNTs in high yield [14,15,16]. The growth mechanism for laser ablation is still not fully understood. Several models have been proposed such as "scooter model" [17] and "precipitation model" [18]. Recently, in-situ optical emission spectroscopy has been adopted

to help understand the growth mechanism [19]. Now there is still no method that can control the chiral indices. If there is no preference, the ratio of semiconducting nanotubes to metallic nanotubes should be 2:1 [3].

Although laser ablation method can used to produce high quality SWNTs, there are some drawbacks. This method can not be used to synthesize SWNTs in large scale. The daily production is about 100 mg, which prevents its wide adoption in industry. The CVD method, on the other hand, can be used to produce carbon nanotubes in large scale [20]. Also the CVD method provides a chance to integrate nanotubes into the integrated circuits, which make it possible to produce nanotube-based electronic devices such as electron transistors and bio-sensors [21,22]. The CVD method can also be used to synthesize both SWNTs and multi-wall carbon nanotubes (MWNTs) [23]. Although the CVD methods can be different in growth conditions such as substrate, catalyst, feeding gas and temperature, it is believed that nanotubes grow as carbon precipitates from supersaturated metal catalysts [24,25].

1.4 Nanotube Characterization

Since the physical properties of nanotubes are highly dependent on their structure, it is important that the structure of nanotubes can be characterized accurately. Many methods have been used to characterize carbon nanotubes such as transmission electron microscopy (TEM), micro Raman spectroscopy, X-ray diffraction (XRD), atomic force microscopy (AFM), scanning tunneling microscopy (STM) and scanning electron microscopy (SEM).

Transmission electron microscopy:

Transmission electron microscopy is by far one of the most straightforward and powerful tools to characterize carbon nanotubes. A modern TEM using a high brightness electron beam (200 kV) can reach atomic resolution, which is fairly enough to accurately measure the nanotube morphology such as the diameter and length. A typical high resolution TEM (HRTEM) image is shown in Fig. 1.4.1(b). This image shows many materials in the SWNTs sample produced by a laser ablation method. Another advantage of TEM method is that, since the electron beam can penetrate the nanotube, the inner shells of MWNTs can be easily characterized, which is hard for other techniques such as STM. It is hard to get the atomic resolution TEM images of carbon nanotubes. The nanobeam electron diffraction (NBD) technique can also be used to characterize the atomic structure of carbon nanotubes. Benefiting from the modern technology, a fine (5 Å diameter) parallel electron probe can be obtained to illuminate a single nanotube and the diffracted electrons can then be collected with a high resolution CCD camera. Due to its special helical structure, the nanotube diffraction patterns are mainly composed of discrete layer lines. The chiral indices of both SWNTs and MWNTs can be extracted from the layer line spacing and intensities. Another advantage of the NBD technique is that, since electron diffraction pattern only depends on the periodicity of the structures, the atomic structures can be characterized even when the nanotubes are vibrating

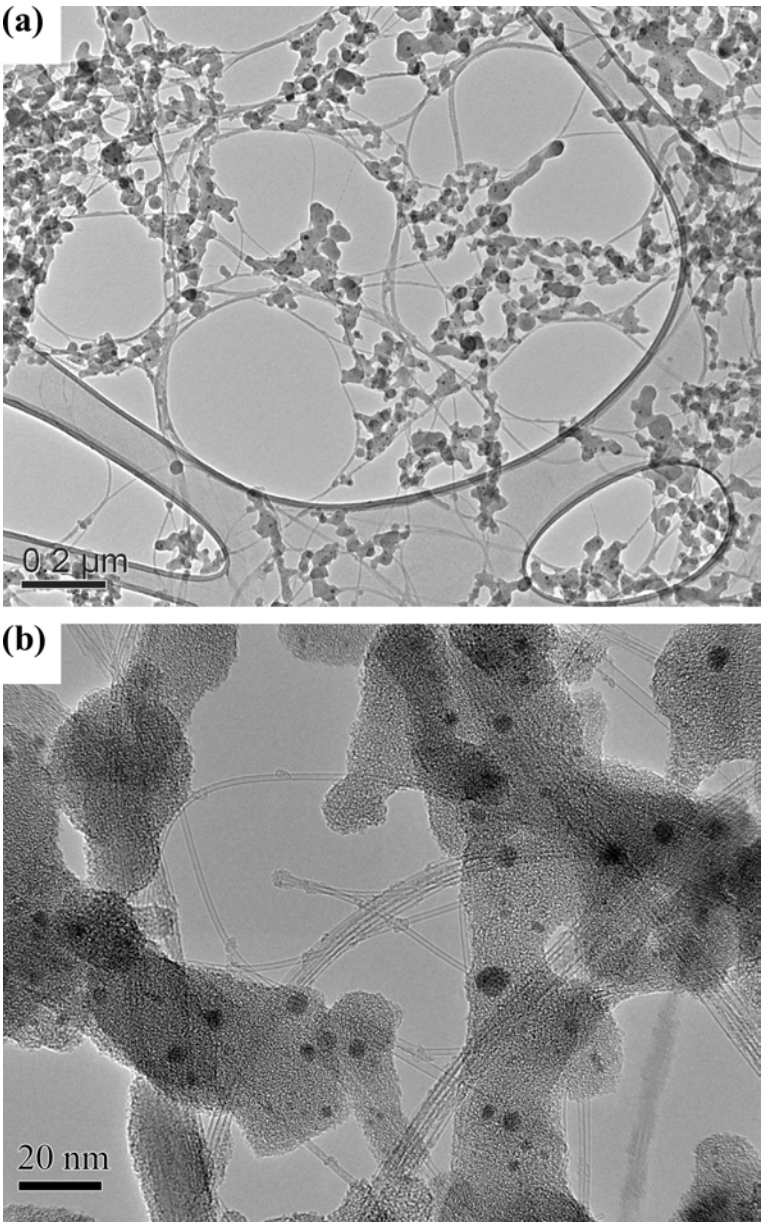

Fig.1.4.1. (a) Low magnification TEM image of SWNTs produced by Co/Si catalysts. (b) HRTEM image shows that SWNTs form long bundles and have an average diameter of 1.5 nm. The dark contrast clusters are metal nanoparticles, which are embedded in amorphous carbon.

X-Ray Diffraction:

X-Ray diffraction has been used to study the quality of laser ablation samples and the structure of SWNT bundles. Information such as average nanotube diameter, diameter distribution, and bundle size can be deduced from the x-ray diffraction data [26].

Raman Spectroscopy,

Raman spectroscopy can be used to study the high energy optical phonon modes in carbon nanotubes. Basically, phonons of well-defined frequencies of the nanotube are excited when incident photons are absorbed. Photons with a frequency equal to the difference between the incident photon frequency and phonon frequency are scattered and measured by using a spectrometer. Fig. 1.4.2 is a typical Raman spectrum obtained from a laser ablation SWNT sample. The peaks between 170 -260 cm^{-1} have been identified to reflect the radial breathing modes (RBM). In the RBM mode, carbon atoms are displaced in the radial directions. The RBM frequencies have shown strong dependence on the diameter of carbon nanotubes. Base on the experimental results and simulations, the RBM frequency is given by $w = 223.75(cm^{-1} \quad nm)/d(nm)$, where d is the nanotube diameter [27].

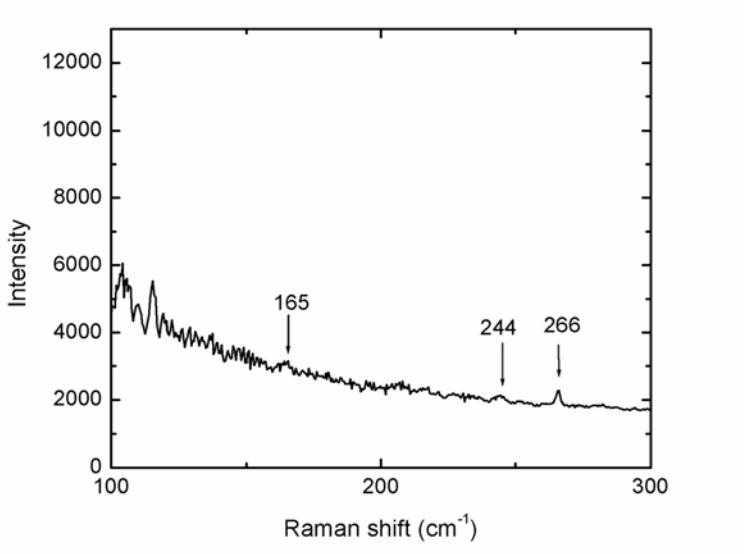

Fig. 1.4.2. Raman spectrum from SWNTs produced by laser ablation using Co/Si catalysts.

1.5 Objectives of This Work

Although nanotubes have been discovered for more than a decade, it is still difficult to handle due to their nanometric dimensions. We intend to develop an effective and reproducible method to fabricate individual carbon nanotubes. This method can be used to produce carbon nanotube-based high performance field emission electron sources in large scale for high precision analytical instruments such as the TEM and SEM. Although carbon nanotubes-based film emitters have been widely studied, field emission from a single carbon nanotube is still not fully understood. By far there is no one field emission measurement base on a single nanotube whose atomic structure has also been characterized. In this work we try to use the nanobeam electron diffraction technique to characterize the atomic structure of a single nanotube and test its field emission properties. This will help us understand the field emission properties of carbon nanotubes. This work will also help understand the field emission behaviors of carbon nanotube films. Due to its sp^2 covalent bonds, carbon

nanotubes can survive high temperature up to more than 2000 K and high electric field up to 6×10^7 V/cm, which makes them an ideal candidate to study thermal field emission. To the author's best knowledge, the thermal field emission properties of carbon nanotubes have not been well studied. In this work, we will also study the thermal field emission properties of a single carbon nanotube. One drawback for CNT-based field emitters is that the work functions are large (4.6 - 5.1 eV), which makes it harder for electrons to escape from the tip of carbon nanotubes. Recent experiments show that the Cs intercalation can dramatically reduce the work functions of SWNT bundles and MWNTs [28,29]. But it is still not clear how Cs doping affects the work function of a single MWNT. In this work, we will dope a single MWNT with Cs and measure the field emission properties of this Cs doped carbon MWNT. Changes in work function are monitored by comparing the slopes of the Fowler-Nordheim (F-N) plots before and after Cs doping. The brightness of a single MWNT is also measured and compared to the traditional point electron sources in this work.

1.6 References

[1] S. Ijima, *Nature* **354**, 56 (1991).

[2] M. S. Dresselhaus, G. Dresselhaus, and P. C. Eklund, *Science of Fullerenes and Carbon Nanotubes* (Academic, New York, 1996).

[3] R. Saito, G. Dresselhaus, and M. S. Dresselhaus, *Physical Properties of Carbon Nanotubes* (Imperial College Press, London, 1998).

[4] M. S. Dresselhaus and P. C. Eklund, *Advances in Physics* **49**, 705 (2000).

[5] M. S. Dresselhaus and M. Endo, "Relation of nanotube to other carbon materials", in *Carbon Nanotubes: Synthesis, Structure, Property and Applications*, M. S. Dresselhaus, G. Dresselhaus, and P. Avouris, (Springer - Verlag, Berlin, 2001).

[6] P. J. F. Harris, *Carbon Nanotubes and Related Structures: New Materials for the 21st Century* (University Press, Cambridge, 1999).

[7] H. Hamada, S. Sawada, and A. Oshiyama, *Phys. Rev. Lett.* **68**, 1579 (1992).

[8] G. S. Painter and D. E. Ellis, *Phys. Rev. B* **1**, 4747 (1970).

[9] R. Satio, G. Dresselhaus, and M. S. Dresselhaus, *Phys. Rev. B* **61**, 2981 (2000).

[10] H. Kataura, Y. Kumazawa, Y. Maniwa, I. Umezu, S. Suzuki, Y. Ohtsuka, and Y. Achiba, *Synthetic Met.* **103**, 2555 (1999).

[11] C. Journet, W. K. Maser, P. Bernier, A. Loiseau, M. L. de la Chapelle, S. Lefrant, P. Deniard, R. Lee, and J. E. Fischer, *Nature* **388**, 756 (1997).

[12] T. Guo, P. Nikolaev, A. Thess, D. T. Colbert, and R. E. Smalley, *Chem. Phys. Lett.* **243**, 49 (1995).

[13] S. Bandow, S. Asaka, Y. Saito, A. M. Rao, L. Grigorian, E. Richter, and P. C. Eklund, *Phys. Rev. Lett.* **80**, 3779 (1998).

[14] Y. Saito, Y. Tani, N. Mitsushima, A. Kasuya, and Y. Nishina, *Chem. Phys. Lett.* **294,** 593 (1998).

[15] S. Seraphin and D. Zhou, *Appl. Phys. Lett.* **64**, 2087 (1994).

[16] L. -C. Qin and S. Iijima, *Chem. Phys. Lett.* **269**, 65 (1997).

[17] A. These, R. Lee, P. Nikolaev, H. Dai, P. Petit, J. Robert, C. Xu, Y. H. Lee, S. G. Kim, A. G. Rinzler, D. T. Colbert, G. E. Scuseria, D. Tomanek, J. E. Fischer, and R. E. Smalley, *Science* **273**, 483 (1996).

[18] R. Sen, S. Suzuki, H. Kataura, and Y. Achiba, *Chem. Phys. Lett*. **349**, 383 (2001).

[19] A. A. Puretzky, D. B. Geohegan, X. Fan and S. J. Pennycook, *Appl. Phys. Lett*. **76**, 182 (2000).

[20] A. M. Cassell, J. A. Raymakers, J. Kong, H. Dai, *J. Phys. Chem. B* **103**, 6484 (1999).

[21] A. Javey, J. Guo, Q. Wang, M. Lundstrom, and H. Dai, *Nature* **424**, 654 (2003).

[22] C. Staii, A. T. Johnson, Jr., M. Chen, and A. Gelperin, *Nano. Lett*. **5**, 1774 (2005).

[23] W. Z. Li, S. S. Xie, L. X. Qian, B. H. Chang, B. S. Zou, W. Y. Zhou, R. A. Zhao, and G. Wang, *Science* **274**, 1701 (1996).

[24] R. T. K. Baker and P. S. Harris, "Formation of Filamentes Carbon," in *Chemistry and Physics of Carbon*, Eds. P. L. Walker and P. A. Thrower, (Marcel Dekker, New York, 1978), vol. **14.**

[25] G. G. Tibbetts, *J. Cryst. Growth* **66**, 632 (1984).

[26] B. Gao, C. Bower, J. D. Lorentzen, L. Fleming, A. Kleinhammes, X. P. Tang, L. E. McNeil, Y. Wu, and O. Zhou, *Chem. Phys. Lett*. **327**, 69 (2000).

[27] A. M. Rao, E. Richter, Shunji Bandow, Bruce Chase, P. C. Eklund, K. A. Williams, S. Fang, K. R. Subbaswamy, M. Menon, A. Thess, R. E. Smalley, G. Dresselhaus, and M. S. Dresselhaus, *Science,* **275**, 187 (1997).

[28] S. Suzuki, Y. Watanabe, T. Kiyokura, K. G. Nath, T. Ogino, S. Heun, W. Zhu, C.Bower, and O. Zhou, *Surf. Rev. Lett.* **9**, 431 (2002).

[29] S. Suzuki, C. Bower, Y. Watanabe, and O. Zhou, *Appl. Phys. Lett.* **76**, 4007 (2000).

Chapter 2. Theory of Field Emission

2.1 Theory of Cold Field Emission

The phenomenon of extraction of electrons from cold metals by intense electric field was first observed in 1901 [1]. An approximate theory was first developed by Schottky [2]. Benefiting from the improved experimental results [3,4] and early theoretical works [5,6], Fowler and Nordheim developed a straightforward theory in 1928 basing on modern quantum mechanics and Sommerfeld's free electron theory of metals [7]. The Fowler-Nordheim (F-N) theory has been widely adopted to explain field emission related phenomena. During the past century, a lot modifications and improvements have been added to the original Fowler-Nordheim theory such as the image force [8, 9], Miller-Good approximation [10], Zener effect [11], and the space charge effect [12].

Field emission can be defined as a process that electrons tunnel through the bended traditional forbidden barrier into the vacuum under strong electrostatic forces. For a metal with a 5.0 eV work function at room temperature, the electric field needs to be higher than 0.3 V/Å in order to make appreciable electrons tunnel through the surface potential barrier. The lower the work function, the easier it is for electrons to tunnel through the surface potential barrier. The current density of emitted electrons can be expressed as

$$J(F,\phi) = \int_0^\infty N(W)D(W)dW \,, \tag{2.1.1}$$

where *N(W)* is the electron supply function which defines the number of electrons incident on a surface of unit area per unit time with a kinetic energy *W* normal to the surface and *D(W)* is the transmission function which defines the fraction of electrons penetrating the potential barrier and escaping to the vacuum. The electron supply function was evaluated by Nordheim according to Sommefeld's theory as [13]

$$N(W) = \frac{4\pi mkT}{h^3} \ln\{1 + \exp[-\frac{W - \zeta}{kT}]\} \tag{2.1.2}$$

with Fermi energy ζ, Boltzmann constant k, Planck's constant h, electron mass m and absolute temperature T. *D(W)* was also evaluated using the matching wave function method by solving the one dimensional wave equations [7]:

$$\frac{d^2\psi}{dx^2} + \frac{8\pi^2 m}{h^2}(W - \phi - \zeta + eFx)\psi = 0 \ \ (\mathrm{x} > 0), \tag{2.1.3}$$

$$\frac{d^2\psi}{dx^2} + \frac{8\pi^2 m}{h^2} W\psi = 0 \, (\mathrm{x} < 0) \tag{2.1.4}$$

with work function ϕ, electric field F and electric charge e. The transmission function *D(W)* was found to be:

$$D(W) = \frac{4\{W(\phi + \zeta - W)\}^{1/2}}{\phi + \zeta} \exp[\frac{-4k(\phi + \zeta - W)^{3/2}}{3F}]. \tag{2.1.5}$$

Fowler and Nordheim found the final current density to be:

$$J(F, \phi) = \frac{6.2 \times 10^{-6} (\zeta / \phi)^{1/2}}{\phi + \zeta} F^2 \exp[\frac{-2.1 \times 10^8 \phi^{3/2}}{F}] \ \ \mathrm{Acm^{-2}} \tag{2.1.6}$$

for F in V/cm and ϕ in eV. Eq. (2.1.6) refers to $T = 0$, but it also works at room temperature. This equation is different from what we used today because the image charge effect is neglected when solving the wave function. In reality, the surface potential will not change

suddenly from the Fermi energy to the vacuum level (Fig. 2.1.1). Instead, the true surface potential barrier should be $V(x) = \phi + \zeta - \frac{e^2}{4x} - eFx$ [8,9].

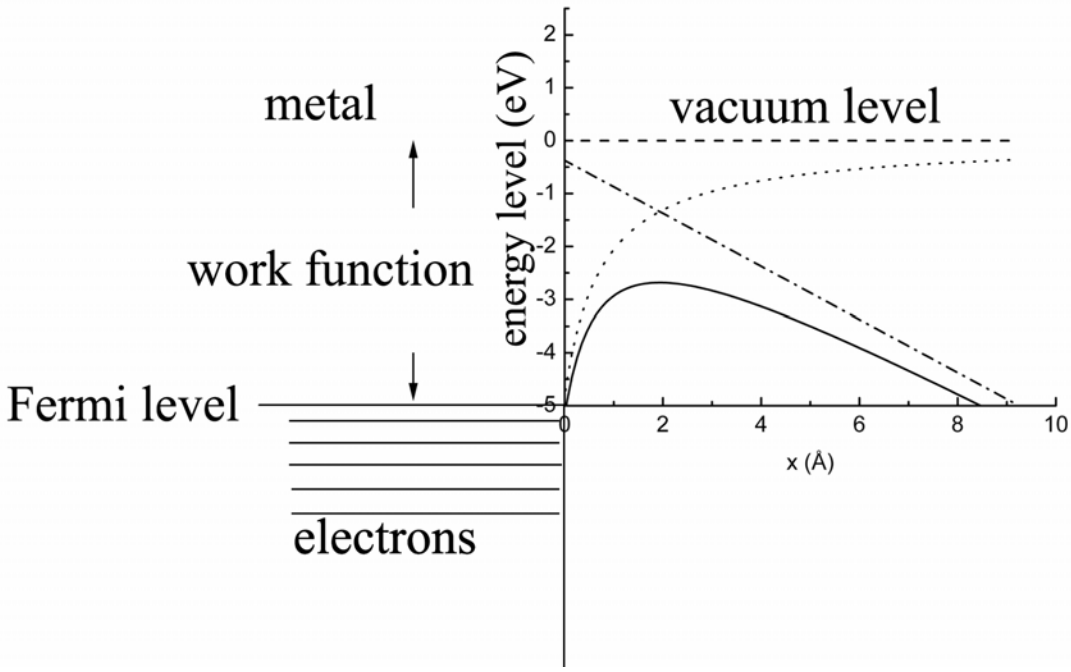

Fig. 2.1.1. Sufrace potential barrier with image potential correction (solid line) and without image potential correction (dash dot line) diagram at a metal (with a 5 eV work fucntion) surface in the presence of a 0.5 V/Å electric field. Dot line is the image potential.

Due to the complexity of the true surface potential function *V(x)*, the Schrödinger equation can not be reduced to one of the standard mathematical physics equations. Instead, the WKB approximation was used to solve the transmission function [14,15,16,17]. The WKB transmission function for an electron of energy *W* transversing a barrier from x_1 to x_2 is:

$$D_{WKB} = \exp[-2\int_{x_1}^{x_2} |k(x)|dx] \tag{2.1.7}$$

with $k(x) = \{2m/\hbar^2[V(x)-W]\}^{1/2}$ $k(x)=\{(2m/\hbar^2)[V(x)-W]\}^{1/2}$. The WKB transmission function with the classical image potential correction was then [14]:

$$D_{WKB}(W) = \exp[-c + \frac{W-\zeta}{d}], \tag{2.1.8}$$

with

$$c = \frac{4}{3}(\frac{\phi^{3/2}}{eF})(\frac{2m}{\hbar^2})^{1/2} v(y), \tag{2.1.9}$$

$$d^{-1} = (\frac{2\phi^{1/2}}{eF})(\frac{2m}{\hbar^2}) t(y), \tag{2.1.10}$$

and

$$y = (e^3F)^{1/2}/\phi, \tag{2.1.11}$$

where *v(y)* and *t(y)* are slowly varying functions related to certain elliptic functions [14, 15]. The "standard result" was then obtained by inserting Eq. (2.1.8) into Eq. (2.1.1) [18]:

$$J(T=0,F,\phi) = \frac{e^3F^2}{8\pi h\phi t^2(y)} \exp[-\frac{8\pi(2m)^{1/2} v(y)}{3he} \frac{\phi^{3/2}}{F}]. \tag{2.1.12}$$

To a good approximation, $t^2(y)=1.1$ and $v(y)=0.95-y^2$, leading to a simplified equation [19]:

$$J(T=0,\phi) = 1.5\times10^{-6} \frac{F^2}{\phi} \exp[\frac{10.4}{\phi^{1/2}}] \exp[-6.44\times10^7 \frac{\phi^{3/2}}{F}] \text{ Acm}^{-2} \tag{2.1.13}$$

for F in V/cm and ϕ in eV.

2.2 Field Emission at Different Temperature

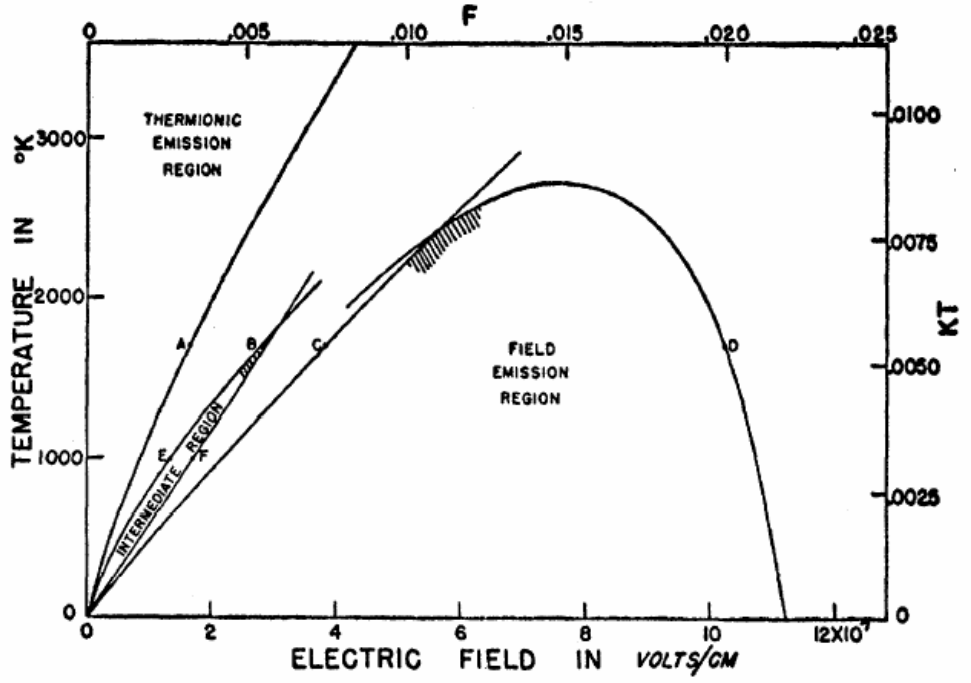

Fig. 2.2.1 The three emission zones for a 4.5 eV work function. Adapted from reference 27.

Although Eq.(2.1.12) and Eq. (2.1.13) are derived for the condition $T = 0$, both equations are valid under 1000 K for high work function (4 - 6 eV) metals. Field emission theories at different temperatures have also been studied. The first qualitative prediction of temperature effect on field emission was given by Houston in 1929 [20]. In 1942, Guth and Mullin adopted a series expansion method to study the temperature effect on field emission [21]. In 1954, Dolan and Dyke used a numerical method to study the field emission at fields between 10^7 and 10^8 V/cm and temperatures up to 3000 K [22]. In Dolan and Dyke's work, the current density was expressed as

$$J(T,F,\phi) = \frac{4\pi mkT}{h^3}\int_{-\infty}^{\infty} A(T,\varepsilon)D(F,\varepsilon)d\varepsilon\,, \tag{2.2.1}$$

with

$$A(T,\varepsilon) = \ln\{1 + Exp[-\varepsilon / kT]\} \tag{2.2.2}$$

and

$$D(F,\varepsilon) = \exp[-6.85\times10^{7}(\phi-\varepsilon)^{3/2} v(y)/F], \tag{2.2.3}$$

where ε is the difference between the electron energy and the Fermi level. This form of transmission function was first used by Sommerfeld and Bethe [23]. In 1955, Dyke found Eq. (2.2.1) agreed well with experimental results at several fields and temperatures in the ranges $2.5\times10^7 < F < 7\times10^7$ V/cm and 300 °C < T < 2000 °C based on electronic pulse technique [24]. For field emission at moderate temperature, Good and Mueller showed [25]

$$J(T,F,\phi) = J(0,F,\phi)\frac{\pi kT/d}{\sin(\pi kT/d)} \tag{2.2.4}$$

with

$$d = \frac{heF}{4(2m\phi)^{1/2}t(y)} = \frac{9.76\times10^{-9}F}{\phi^{1/2}t(y)}. \tag{2.2.5}$$

Eq. (2.2.4) is accurate when $p = kT/d < 0.7$ and breaks down when $p = kT/d = 1$ [26].

In 1956, Murphy and Good studied the electron emission phenomena from a unified point of view [27]. In this work, the electron emission was divided into three zones in terms thermionic emission, field emission and emission in the intermediate region (Fig. 2.2.1). Each of these zones was governed by different equations in terms of the Richardson-Schottky equation, the Fowler-Nordheim (F-N) equation (Eq. (2.1.4), Eq. (2.2.12)) and the Murphy-Good (M-G) equation. Murphy and Good found there was a new type of dependence of emitted current density on temperature and electric field, which applied in a narrow region between thermionic emission and field emission. In Murphy and Good's work, a general current density expression was developed as

$$J(T,F,\varsigma)=\frac{4\pi mkT}{h^3}\int_{-W_a}^{W_l}\frac{\ln\{1+\exp[-(W-\zeta)/kT]\}}{1+\exp[(4/3)\sqrt{2}(F\hbar^4/m^2e^5)^{-1/4}y^{-3/2}v(y)]}dW + \frac{4\pi mkT}{h^3}\int_{W_l}^{\infty}\ln\{1+\exp[-(W-\zeta)/kT]\}dW, \tag{2.2.6}$$

which works at any electric field and temperature [27]. Converting to the Hartree units for convenience, J is redefined to be the current density divided by $m^3e^9\hbar^{-7} = 2.37\times10^{14}$ Acm^{-2}; F to mean electric field divided by $m^2e^5\hbar^{-4} = 5.15\times10^9$ V/cm; and ζ, kT, W, Wa, W_l to mean the corresponding energies divided by $me^4\hbar^{-2}$ = 27.2 eV. In these terms, the emitted current density can be expressed as

$$J(T,F,\varsigma)=\frac{kT}{2\pi^2}\int_{-W_a}^{W_l}\frac{\ln\{1+\exp[-(W-\zeta)/kT]\}}{1+\exp[(4/3)\sqrt{2}(F)^{-1/4}y^{-3/2}v(y)]}dW + \frac{kT}{2\pi^2}\int_{W_l}^{\infty}\ln\{1+\exp[-(W-\zeta)/kT]\}. \tag{2.2.7}$$

By applying the following two approximations

$$\ln\{1+\exp[-(W-\zeta)/kT]\}\cong\exp[-(W-\zeta)/kT], \tag{2.2.8}$$

and

$$\{1+\exp[(4/3)\sqrt{2}F^{-1/4}y^{-3/2}v(y)]\}^{-1}=\exp[-(4/3)\sqrt{2}F^{-1/4}y^{-3/2}v(y)], \tag{2.2.9}$$

the current density can be described by

$$J=\frac{kT}{2\pi^2}\int_{-W_a}^{W_l}\exp[-\frac{W-\zeta}{kT}-\frac{4\sqrt{2}v(y)}{3F^{1/4}y^{3/2}}]dW+\frac{kT}{2\pi^2}\int_{W_l}^{\infty}\ln\{1+\exp[-(W-\zeta)/kT]\}dW\,. \tag{2.2.10}$$

Eq. (2.2.10) can be conveniently evaluated by the saddle point method and will lead to the current density in the intermediate region:

$$J=\frac{F}{2\pi}(\frac{kTt(y)}{2\pi})^{1/2}\exp[-\frac{\phi}{kT}+\frac{F^2\Theta(y)}{24(kT)^3}] \tag{2.2.11}$$

with

$$\Theta(y) = 3t^{-2}(y) - 2v(y)t^{-3}(y), \tag{2.2.12}$$

and

$$y = 8(kT)^2 t^2 (F^{1/2}/-\eta)/F^{3/2}, \tag{2.2.13}$$

where η is the energy at the peak of the integrand and t can be put equal to one as a first approximation.

In 1966, Christov developed a general theory of electron emissions from metals [28]. In Christov's work, the current density is evaluated as

$$J = Q_1 J_{F-N} + Q_2 J_{M-G} + Q_3 J_{R-S} \tag{2.2.14}$$

where $J_{F\text{-}N}$, $J_{M\text{-}G}$, $J_{R\text{-}S}$ are the current densities from the field emission region, the intermediate region, the thermionic emission region, respectively, and Q_1, Q_2, Q_3 are the corresponding factors determined by Eq. (4a, 4b, 4c), Eq. (5a), Eq. (6a, 6b, 6c) in reference 28.

2.3 Field Emission Properties of Carbon Nanotubes

After carbon nanotubes have been discovered, three groups reported field emission from CNTs at low turn-on fields and high current densities [29,30,31]. These experiments have inspired a strong interest in studying the field emission properties of CNTs. There are several techniques to mount a single CNT to a supporting tip. In 1995, Rinzler et al. mounted a single CNT onto a support tip using a micromanipulator and an optical microscope [31]. Due to the limited resolution of the optical microscope, it was hard to tell the difference between an individual CNT or a small CNT bundle. de Jonge developed a more precise method to mount an individual CNT to a tungsten tip by using a piezo-driven nanomanipultor in an

SEM [32, 33]. Other similar methods were used to mount nanotubes on scanning probe tips [34,35]. Individual CNTs could also be picked up by the atomic force microscope tips [36].

The electrons emitted from an open carbon nanotube form a ring-like pattern [37,38]. On the other hand, a CNT with a cap produces a bright spot on the phosphor screen [37, 38]. Sometimes, the emission patterns from clean capped CNTs show certain symmetry which can be explained by the cap structure. Comparing to other traditional point electron source, the CNTs have been proved to possess high reduced brightness, which is defined as

$$B_r = \frac{I}{\Omega \pi r_v^2 U} \tag{2.3.1}$$

with solid angle Ω , virtual source radius r_v and beam potential U. The virtual source is the area from which the electrons appear to originate when their trajectories are traced back [39]. The virtual source size measurements have been realized by operating CNTs as point source in a point-projection microscope [40, 41]. It has been found that the CNTs have a reduced brightness between 1.3×10^9 and 2.5×10^9 $Am^{-2}sr^{-1}V^{-1}$, which is one order of magnitude higher than that of the state-of-the-art Schottky emitters [42]. Also carbon nanotubes have shown long lifetime up to 16 months at a current of 100 nA, a 10^{-10} Torr vacuum level and 800 K temperature [43]. Due to their extreme small dimensions, the emission stability of carbon nanotubes is very sensitive to absorptions. The emission stability of a few percents was obtained by practicing an initial cleaning and operating the CNTs under 10^{-10} Torr vacuum level at 800 K [41]. Carbon nanotubes can also be operated at low vacuum level 10^{-7} Torr at the cost of stability. The energy distribution of CNTs has also been studied. As expected, CNTs shown a low energy spread of 0.2 – 0.3 eV [32,44,45,46].

2.4 References

[1] R. F. Earhart, *Phil. Mag.* **1**, p. 147 (1901).

[2] W. Schottky, *Z. Physik* **14**, 80 (1923).

[3] R. A. Milikan and C. F. Eyring, *Phys. Rev.* **27**, 51 (1926).

[4] R. A. Milikan and C. C. Lauritsen, *Proc. Nat. Ac. Sci.* **14**, 45 (1928).

[5] O. W. Richardson, *Proc. Roy. Soc. Lond. A* **117**, 719 (1928).

[6] W. V. Houston, *Z. Physik* **47**, p. 33 (1928).

[7] R. H. Fowler and L. W. Nordheim, *Proc. Roy. Soc. Lond. A* **119**, 173 (1928).

[8] D. M. Newns, *J. Chem. Phys.* **50**, 4572 (1969).

[9] J. W. Gadzuk, *Phys. Rev. B* **1**, 2110 (1970).

[10] E. C. Kemble, *The Fundamental Principles of Quantum Mechanics* (McGraw-Hill, New York, 1937), p. 100.

[11] C. Zener, *Proc. Roy. Soc. Lond. A* **145**, 523 (1934).

[12] J. P. Barbour, W. W. Dolarn, J. K. Trolan, E. E. Martin, and W. P. Dyke, *Phys. Rev.* **92**, 45 (1953).

[13] L. W. Nordheim, *Loc. Cit.* Eq. (11).

[14] L. W. Nordheim, *Proc. Roy. Soc. Lond. A* **121**, 626 (1928).

[15] R. F. Burgess, H. Kroemer, and J. M. Houston, *Phys. Rev.* **90**, 515 (1953).

[16] L. I. Schiff, *Quantum Mechanics* (McGraw-Hill, New York, 1949), p. 178.

[17] E. Merzbacher, *Quantum Mechanics* (Wiley, New York, 1961), p. 121.

[18] R. D. Young, *Phys. Rev.* **113**, 110 (1959).

[19] C. A. Spindt, I. Brodie, L. Humphrey, and E. R. Westerberg, *J. Appl. Phys.* **47**, 5248 (1976).

[20] W. V. Houston, *Phys. Rev.* **33**, 361 (1929).

[21] E. Guth and C. J. Mullin, *Phys. Rev.* **61**, 339 (1942).

[22] W. W. Dolan and W. P. Dyke, *Phys. Rev.* **95**, 327 (1954).

[23] A. Sommerfeld and H. Bethe, *Handbuch der Physik* (Springer-Verlag, Berlin, 1933) Vol. **24**, p. 441.

[24] W. P. Dyke, J. P. Barbour, E. E. Martin, and J. K. Trolan, *Phys. Rev.* **99**, 1192 (1955).

[25] R. H. Good Jr. and E. W. Mueller, *Handbuch der Physik* (Springer-Verlag, Berlin, 1956) Vol. **21**, p. 176.

[26] L. W. Swanson and A. E. Bell, *Advances in Electronics and Electron Physics*, (Academic Press, New York and London, 1973), Vol. **32**, p. 303.

[27] E. L. Murphy and R. H. Good, Jr., *Phys. Rev.* **102**, 1464 (1956).

[28] S. G. Christov, *Phys. Status. Solidi* **17**, 11 (1966).

[29] L. A. Chernozatonskii, Y. V. Gulyaez, Z. Y. Kosakovskaya, I. N. Sinitsyn, G. V. Torgashov, Yu. F. Zakharchenko, E. A. Fedorov, and V. P. Val'chuk, *Chem. Phys. Lett.* **75**, 3129 (1995).

[30] W. A. de Heer, A. Chatelain, and D. Ugarte, *Science* **270**, 1179 (1995).

[31] A. G. Rinzler, J. H. Hafner, P. Nikolaev, L. Lou, S. G. Kim, D. Tomanek, P. Nordlander, D. T. Colbert, and R. E. Smalley, *Science* **269**, 1550 (1995).

[32] N. de Jonge and N. J. van Druten, *Ultramicroscopy* **95**, 85 (2003).

[33] N. de Jonge, Y. Lam, and M. Kaiser, *Nano Lett.* **3**, 1621 (2003).

[34] H. Nishijima, S. Akita, and Y. Nakayama, *Jpn. J. Appl. Phys.* **38**, 7247 (1999).

[35] Y. Nakayama, H. Nishijima, S. Akita, K. I. Hohmura, S. H. Yoshimura, and K. Takeyasu, *J. Vac. Sci. Technol. B* **18**, 661 (2000).

[36] J. H. Hafner, C. L. Cheung, T. H. Oosterkamp, and C. M. Lieber*, J. Phys. Chem. B* **106**, 743 (2001).

[37] Y. Saito, K. Hamaguchi, K. Hata, K. Uchida, Y. Tasaka, F. Ikazaki, M. Yumura, A. Kasuya, and Y. Nishina, *Nature* **389**, 554 (1997).

[38] K. Hata, A. Takakura, and Y. Satio, *Surf. Sci.* **490**, 296 (2001).

[39] J. F. Hainfeld, *Scan. Electron Microsc.* **1**, 591 (1977).

[40] N. de Jonge, Y. Lamy, K. Schoots, and T. H. Oosterkamp, *Nature* **420**, 393 (2002).

[41] N. de Jonge, *J. Appl. Phys.* **95**, 673 (2004).

[42] L. W. Swanson and G. A. Schwind, *Handbook of charge particle optics* (CRC Press, Boca Raton, FL, 1997), p. 77.

[43] N. de Jonge and J. M. Bonard, *Phil. Trans. R. Soc. Lond. A* **362,** 2239 (2004).

[44] J. M. Bonard, J. P. Salvetat, T. Stockli, L. Forro, and A. Chatelain, *Appl. Phys. A* **69**, 245 (1999).

[45] M. J. Fransen, T. L. van Rooy, and P. Kruit, *Appl. Surf. Sci.* **146**, 312 (1999).

[46] O. Groening, O. M. Kuettel, C. Emmenegger, P. Groening, and L. Schlapbach, *Appl. Phys. Lett.* **69**, 476 (1996).

Chapter 3. Synthesis and Characterization of Single Carbon Nanotubes

Chemical vapor deposition method has been used to synthesize carbon fibers since the 1970's [1-3]. It has been believed that in the CVD process, carbon atoms from the decomposition of hydrocarbon gases defuse into the catalyst particles and precipitate as a cylinder from either the top (top mode) or the bottom (root mode) of the catalyst particles [3]. Since the discovery of carbon nanotubes in 1991, CVD method has been optimized to produce both SWNTs [4,5,6] and MWNTs [7,8,9]. Compared to the laser ablation and the arc-discharge methods, CVD can be used to synthesize CNTs in large scale in a more controllable manner. By controlling the catalysts, gas pressure, flow rate, different hydrocarbon gases and substrates, different types of carbon nanotubes can be synthesized [10,11,12]. In this chapter, we will present a simple and controllable method to produce single MWNTs by using a two-step CVD method.

3.1 CVD Synthesis of Individual MWNTs

3.1.1 Experimental

The experiments were carried out in a CVD system. The reaction chamber was a 1-inch diameter quartz tube. It could be heated up to more than 1400 °C by an electric tube furnace with a temperature control unit. The flow rates of feeding gases such as methane, hydrogen

and argon were controlled independently by flow meters. The pressure in the reaction chamber was kept at 1 atmosphere.

We adopt a two-step CVD method to produce carbon fibers with CNTs embedded inside [13]. Alumina plates with dimensions 1×1 cm^2 (from Fisher Sci.) were used as the substrates. A glass cutter was used to cut as many as possible parallel and vertical lines on the substrate surface. These lines would help the catalyst stay on the substrate. Then the substrate was carefully cleaned by sonicating it in ethanol for 20 min. One molar ferric nitrate ($Fe(NO_3)_3$) aqueous solution was deposited on the alumina substrate, which was left to dry in air before being baked in an oven at 120 °C for 20 min. The ferric nitrate should form a dark yellow film and be well adhered to the alumina. The substrate was then put in an alumina boat and positioned at the center of the quartz tube. The reaction chamber was vacuumed until the pressure was below 1 Torr. Argon gas was allowed to flow at 100 ml/min to keep the pressure at 1 atmosphere. Then the furnace was heated to 900 °C in 20 min under the Ar atmosphere. After the tube reactor reached 900 °C, methane (10% mixed with Ar) and hydrogen (5% mixed with nitrogen) were introduced into the reactor chamber at flow rates of 480 ml/min and 80 ml/min, respectively. The furnace was heated continuously to 1200°C in 25 min. After the furnace reached 1200 ^oC, the hydrogen supply was switched off and the system was kept running for 1 more hour with only methane flowing through the reaction chamber. Afterwards, the methane and power were turned off, and the system was allowed to cool to the room temperature in Ar. Micron-sized carbon fibers were then grown on the substrate. These fibers were well-aligned and inclined toward the direction of gas flow. The substrate was placed in water and sonicated for 10 min before dropping the solution onto the TEM grids. The microstructure of fiber and nanotubes was examined in TEM (JEM-2010F).

3.1.2 Results and Discussion

After taking the substrate out of the chamber, micron sized carbon fibers could be seen on them. These carbon fibers were well aligned and inclined toward to the flow direction. Several concentrations of ferric nitrate ($Fe(NO_3)_3$) aqueous solutions were tested and we found that the concentrations between 1 mole/L and 1.5 mole/L produced the highest yield. Catalysts should be uniformly deposited on the substrate and allowed to dry slowly. After the catalyst-deposited substrate was left to dry in air overnight, baking it at 120°C in an oven helped form a layer of dark yellow uniform thin film on the alumina substrate. This catalyst film should be well adhered to the substrate and not go off easily. In the process of heating the substrate to 900 °C, the Ar flow rate should be below 100 ml/min to avoid blowing the catalysts away.

The flow rate of methane has a strong effect on the diameter distribution of carbon fibers. The direct experimental proof is that, when putting a substrate in the alumina boat, the fibers grown at the bottom of the substrate had smaller diameters than those grown on the top of the substrate. This can be explained by the fact that the gas flow rate at the bottom of substrate was lower than that at the top of the substrate due to the blockage effect of the boat. The diameter of the carbon fibers (0.5 - 10 μm) can be controlled by adjusting the flow rate of methane and the reaction time.

Hydrogen also played an important role in the process of nanotube and fiber growth. A small amount of hydrogen could greatly reduce the formation amorphous carbon. CVD experiments without hydrogen mainly produced fiber-like structures made of amorphous carbon, which were very fragile and could be hardly to be picked up. A large amount of

hydrogen was also not good for the fiber growth. For example, CVD experiments with a methane/hydrogen flow rate ratio of 2:1 produced very few thin fibers on the substrate. In our experiments, we used CH_4/H_2 flow rate ratio of 6:1 to produce strong and clean carbon fibers.

The second step heating between 900 ^oC and 1200 ^oC was also very important. In this process, methane decomposed rapidly. A layer of dark amorphous carbon could be observed on the quartz tube wall in less than 1 min when the chamber temperature was higher than 1150 ^oC. These carbon atoms were deposited on the surface of carbon nanotubes and formed pyrolytic carbon layers.

3.2 SEM Characterization

Scanning electron microscopy (SEM) was used to study the morphology of carbon fibers. The carbon fibers were scratched off the substrate and dispersed on a silicon substrate for SEM imaging. Fig. 3.2.1 shows the cross section of a carbon fiber. SEM images have shown these carbon fibers are mainly composed of a layered structure (Fig. 3.2.1). The whole carbon fiber could be formed in two steps. In the first step, an individual nanotube was grown from a catalyst (Fig. 3.2.2 and Fig. 3.2.3). In the second step, carbon atoms from the decomposition of methane were deposited on the nanotube and formed a pyrolytic carbon layer and wrapped the nanotube in the core (Fig.3.2.2). Once a carbon fiber was fractured, a nanotube would extrude from the fiber due to its higher toughness (Fig. 3.2.3).

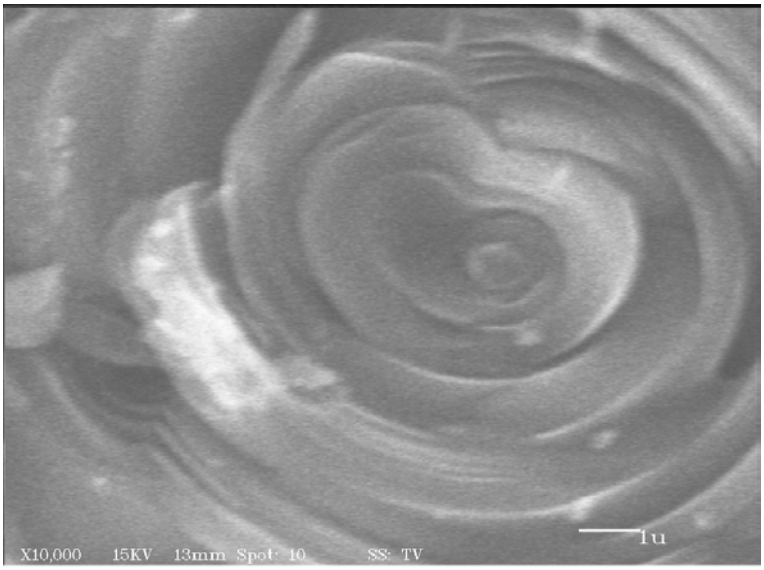

Fig. 3.2.1. SEM image of the cross section of a carbon fiber. It shows that the carbon fiber mainly composed of multi-layer pyrolytic carbons.

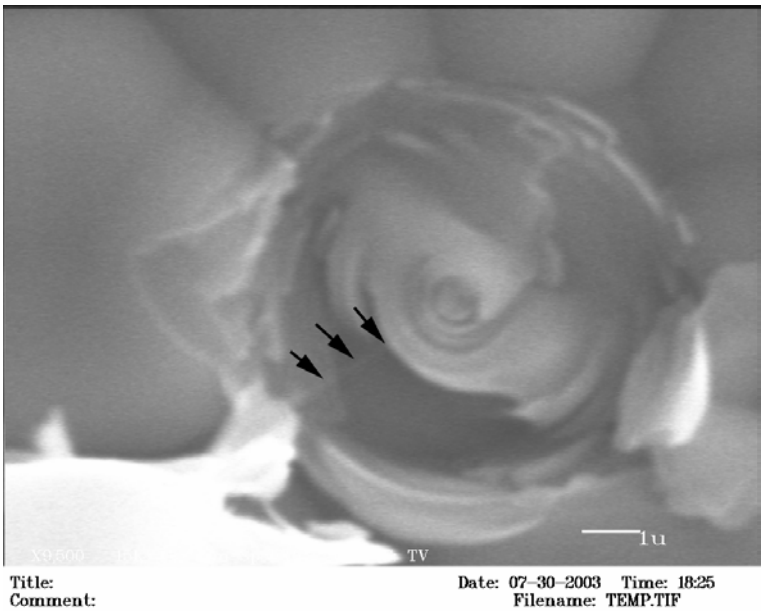

Fig. 3.2.2 SEM image of the cross section of a fractured carbon fiber. A single carbon nanotube (indicated by dark arrows) extrudes from the center of the carbon fiber.

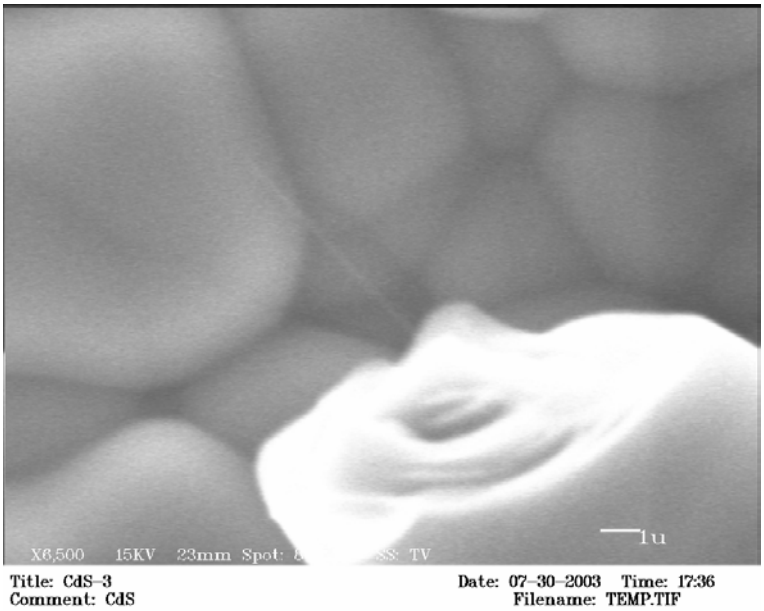

Fig. 3.2.3. A ~ 6 μm long carbon nanotube extrudes from a carbon fiber with 10 μm diameter.

3.3.3 TEM Characterization

High resolution TEM imaging was also used to study the microstructure of both the carbon nanotubes and the fibers. Fig. 3.3.1 is an HRTEM image of the pyrolytic carbon layer of a fiber. It shows that the layer is mainly composed of graphite of different orientation with dimensions of a few nanometers and amorphous carbon. Since both amorphous carbon and graphite are good conductors, the whole carbon fiber will have a good electrical conductivity.

HRTEM images review that all the nanotubes embedded inside the fibers are MWNTs. The thinnest CNT observed is a double wall carbon nanotube (DWNT). The nanotubes grown in this way have a rather large diameter distribution and could have from 2 walls to as many as 20 walls. We have used the TEM to examine 25 nanotubes and found that 23 (92%) nanotubes have diameters in the range from 3 nm to 12 nm with an average diameter of 6 nm (Fig. 3.3.2). Fig. 3.3.3 shows a twelve-wall carbon nanotube lying on the holey carbon film. The HRTEM studies of the cap structure of nanotubes showed a great diversity. Both conical cap and flat cap were observed and are shown in Fig. 3.3.4(a and b).

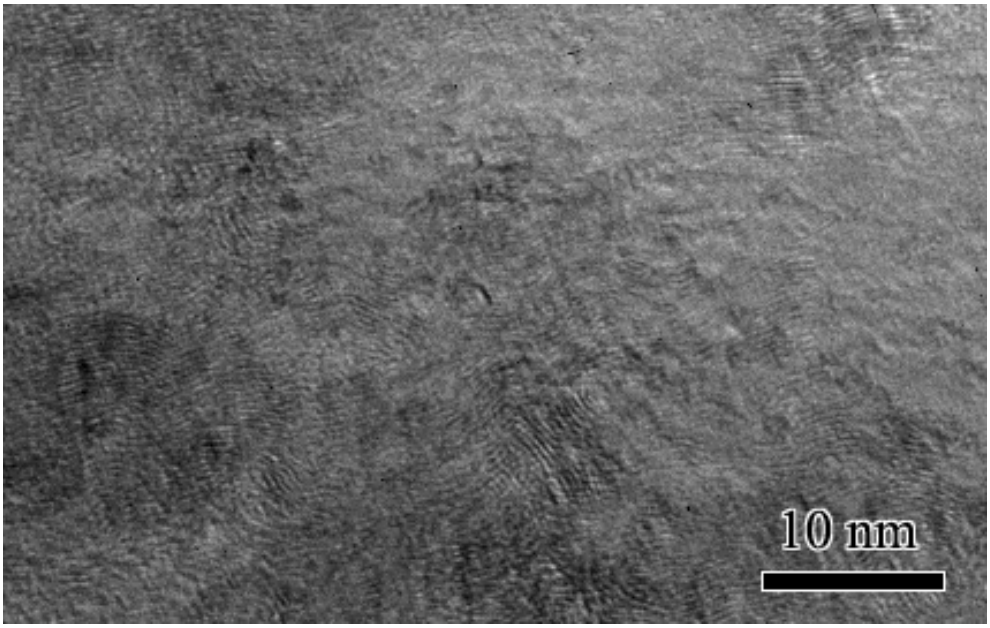

Fig. 3.3.1 HRTEM image of a pyrolytic carbon layer around an embedded single MWNT. It shows that the pyrolytic carbon layer is mainly composed of graphite domains of different orientations and amorphous carbon.

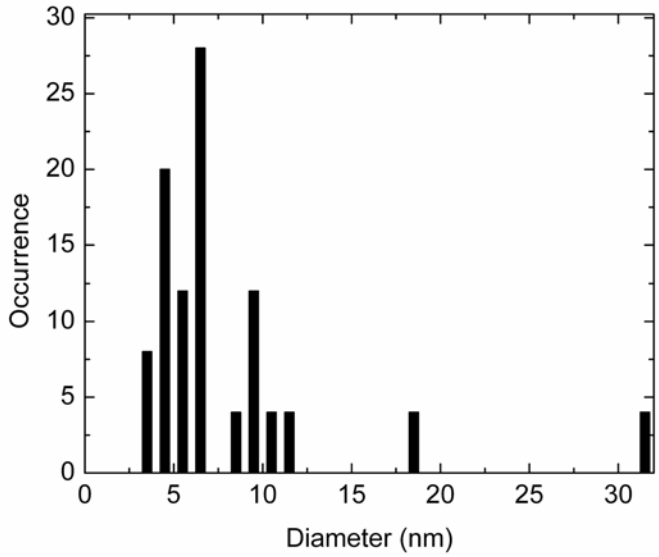

Fig. 3.3.2. Diameter distribution of 25 individual nanotubes extruded from the carbon fibers. Twenty three (92%) nanotubes have diameters in the range from 3 nm to 12 nm with an average diameter of 6 nm.

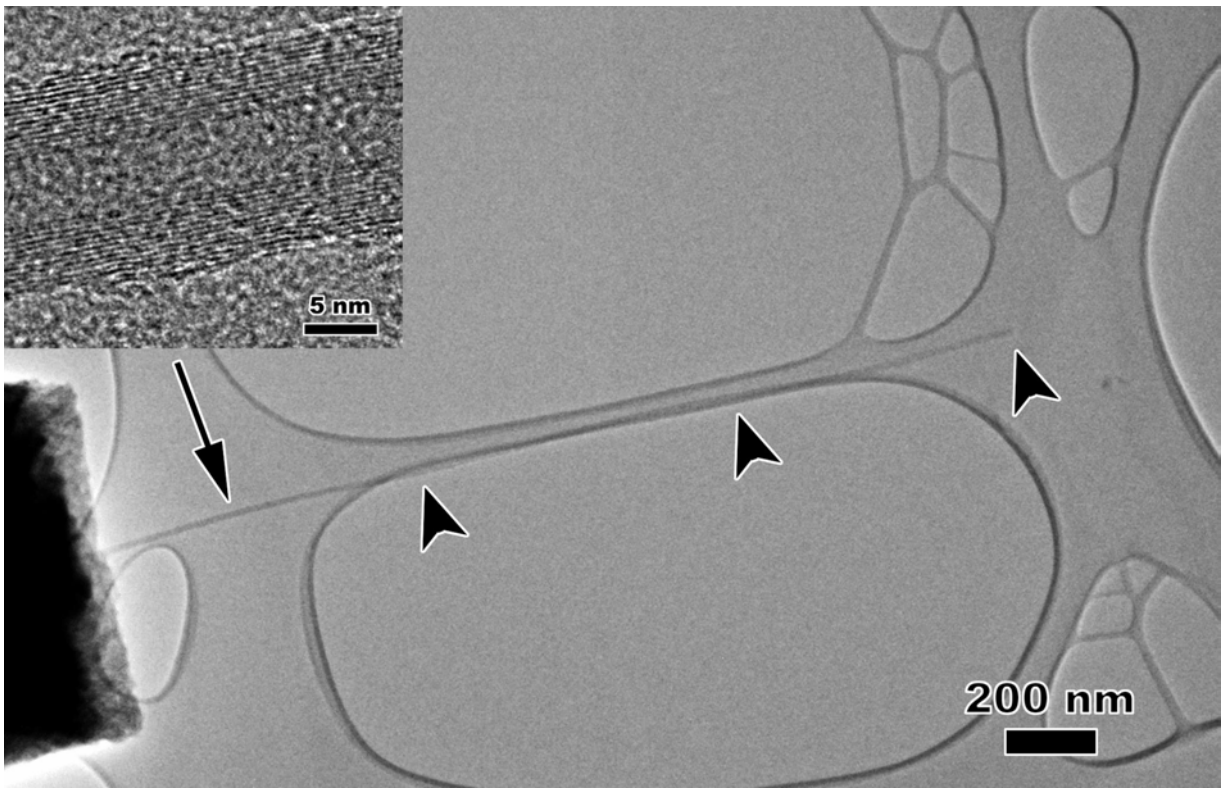

Fig. 3.3.3. A single nanotube extrudes from a micron-sized fiber fractured by sonication. The nanotube is 11.5 nm in diameter and 2 μm in length. The inserted HRTEM image indicates that this MWNT has 12 walls.

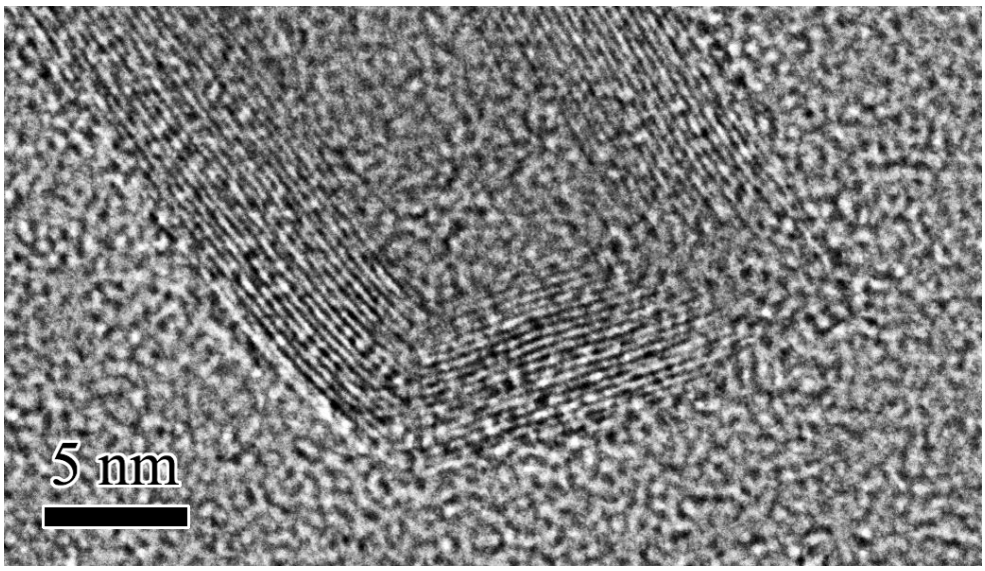

Fig. 3.3.4(a)

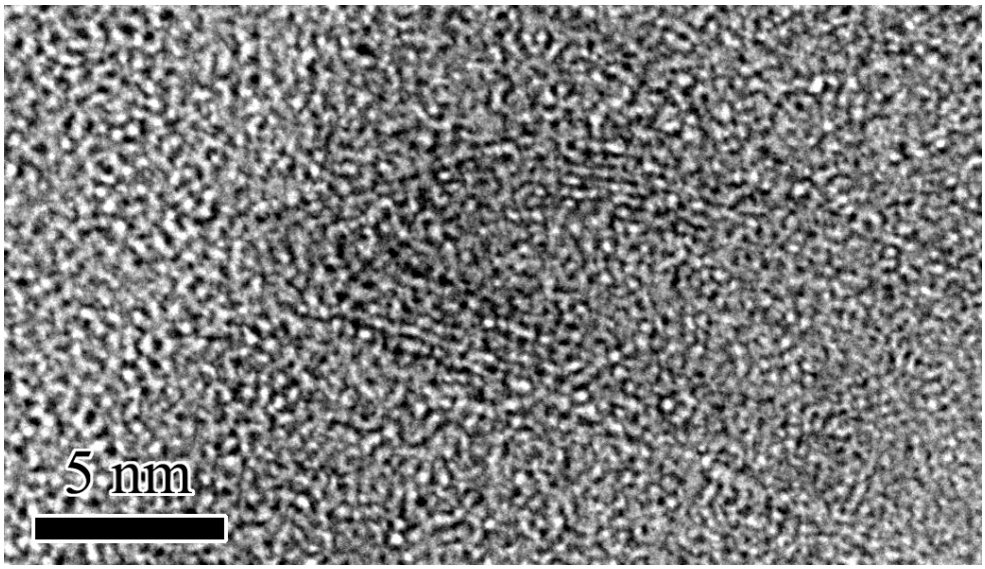

Fig. 3.3.4(b)

Fig. 3.3.4. (a) HRTEM image of a flat capped MWNT grown inside a carbon fiber. (b) HRTEM image of a seven-walled carbon nanotube with a conical cap grown inside a carbon fiber.

3.4 Nanobeam Diffraction Theory

Although there are several techniques that can be used to characterize the atomic structure of SWNTs, the electron diffraction techniques shows an explicit advantage in atomic structures determination of MWNTs over the other techniques. The first theoretical approach to explain the electron diffraction from carbon nanotubes was obtained by Qin based on CCV theory in 1994 [14] and followed by Lucas in 1996 [15]. The CCV theory was developed to study the α -helix molecules in 1952 [16].

In Qin's work, the structure factor of a carbon nanotube was described as

$$F(R,\Phi,l) = \sum_{n=-\infty}^{n=\infty} B_n(R,\Phi)T_{nl} \tag{3.4.1}$$

with

$$B_n(R,\Phi) = \sum_{n=-\infty}^{n=\infty} \exp[in(\Phi+\frac{\pi}{2})]J_n(\pi dR), \tag{3.4.2}$$

$$T_{nl} = \sum_j f_j \exp[2\pi i(\frac{nx_j}{\pi d}+\frac{lz_j}{c})], \tag{3.4.3}$$

$$c = \sqrt{3}C_h / M, \tag{3.4.4}$$

where f is the atomic scattering amplitude of carbon for electrons, c is the periodicity of the carbon nanotube along tube axis and M is the maximum common divisor of $(2u+v)$ and $(2v+u)$. A (u, v) nanotube can be formed by u identical helices and each helix can be decomposed to two monoatomic helices. Adding the structure factors of all carbon helices leads to [17, 18]:

$$F(R,\Phi,l) = \frac{4\pi^2 d}{3\sqrt{3}a_{C-C}^2}\sum_{m,n} fx_{uv}(n,m)\gamma_{uv}(n,m)J_n(\pi dR)\exp[in(\Phi+\frac{\pi}{2})], \tag{3.4.5}$$

with

$$x_{uv}(m,n) = 1 + \exp[2\pi i \frac{n + (2u+v)m}{3u}] \tag{3.4.6}$$

and

$$\gamma_{uv} = \frac{1 - \exp[-2\pi i(n+mv)]}{1 - \exp[-2\pi i(n+mv)/u]} = \begin{cases} u, & if \quad (n+mv)/u = \text{int}. \\ 0, & otherwise. \end{cases} \tag{3.4.7}$$

where d is the diameter of the carbon nanotube, $a_{C\text{-}C}$ is the C-C bond length and n, m, and l are all integers that governed by a selection rule:

$$l = \frac{(u+2v)n + 2(u^2 + v^2 + uv)m}{uM}. \tag{3.4.8}$$

The diffraction intensity is given by

$$I(R,\Phi,l) = \mid F_{uv}(R,\Phi,l) \mid^2. \tag{3.4.9}$$

Eq. (3.4.5) indicates that there will be a series of discrete layer lines along the Z direction whose intensities are mainly modulated by Bessel functions. For the equatorial layer line ($l = 0$), the intensity is mainly dominated by the zero order Bessel function. The three principle layer lines labeled as $l_1 = (2u+v)/M$, $l_2 = (u+2v)/M$, $l_3 = (u-v)/2M$ have layer line spacings $D_1 = l_1/c$, $D_2 = l_2/c$, $D_3 = l_3/c$. The intensities of three principle layer lines are governed by three dominate Bessel functions whose orders are $n_1 = -v$, $n_2 = u$, and $n_3 = -(u+v)$, respectively [19]. Based on these relations, the v/u ratio can be expressed as [19]

$$\frac{v}{u} = \frac{2D_2 - D_1}{2D_1 - D_2} \tag{3.4.10}$$

For MWNTs with N concentric shells, the structure factor can be obtained by summing all the structure factors from each shell as [20,21,22]:

$$F(R,\Phi,l) = \frac{4\pi^2}{3\sqrt{3}a_{C-C}^2} \sum_j^N f d_j \delta(Z - \frac{l_j}{c_j}) \sum_{m,n} f x_j(n,m) \gamma_j(n,m) J_n(\pi d_j R) \exp[in(\Phi + \frac{\pi}{2})] \exp[i\varphi_j], \tag{3.4.11}$$

where d_j, c_j are the diameter and axial periodicity of the jth shell and φ_j specifies the phase shift of the jth shell relative to the reference shell.

Experimental

The NBD experiments were carried out in a JEM-2010F (equipped with a field emission gun) operated at 80 kV, which would reduce the radiation damage to the carbon nanotubes. The field emission gun has an advantage of having high brightness and can provide a higher beam intensity which is important due to the small diffraction cross section of carbon nanotube. A 10 μm condenser aperture was used to form a fine and parallel electron probe of 40 nm diameter. A small condenser aperture would also reduce the brightness of the central spot and reveal more useful information on the equatorial layer line. A high resolution 2K×2K CCD camera was used to collect the diffraction patterns. The camera length was set at 30 cm and the exposure time was usually between 30 and 60 sec.

Analysis

For a single MWNT extruded from a carbon fiber, HRTEM images with lattice resolution usually can not be obtained due to the thermal vibrations of the carbon nanotube. Electron diffraction which is not so sensitive to the real space location can be used to study the atomic structure of MWNTs even when they are vibrating.

The procedure for atomic structure determination of a MWNT is

(a) Estimate the inner and outer diameter of the MWNT;

(b) Identify the principal layer lines l_1 and l_2 for each shell;

(c) Measure the layer line spacing D_1 and D_2 for each shell;

(d) Calculate the *v/u* ratio using Eq. (3.4.10);

(e) Find possible chiral indices and apply the wall spacing constraint within the estimated diameter range;

(f) Simulate the equatorial layer line intensity to determine the accurate number of walls and single out the possible chiral indices for each shell;

(g) Use diffraction symmetry to assist determining the chiral indices of each shell.

We demonstrate this procedure by analyzing an experimental electron diffraction pattern (Fig. 3.4.1). First, the layer line spacings D_1 and D_2 were measured and the *v/u* ratios were calculated to be 0.3793, 0.3810, 0.3846, 0.3889, 0.3913, 0.3929, 0.4000 and 0.4091 using Eq. (3.4.10). After the *v/u* ratio is determined, all the possible chiral indices in the estimated diameter range were listed in Table 3.4.1. The inner and outer diameters of the MWNT were carefully estimated to be about 4 nm and 8 nm, respectively from the high magnification TEM image. Applied the wall spacing constraint, which was that the wall spacing between two neighbor shells should be between 0.30 nm and 0.4 nm, and singled out all the possible sets of configurations (Table 3.4.2). In order to further determine the number of shells, an equatorial layer line intensity simulation would be helpful. The scatting factor for the equatorial layer line is [21]:

$$F(R) = f\sum_{i}^{N} d_i J_0(\pi d_i R)\,. \tag{3.4.12}$$

N is the number of shells. The equatorial line intensity was calculated by using $I(R) = |F(R)|^2$ and the atomic scattering factor of carbon f was calculated by using the Doyle-Turner equation [23]:

$$f(s) = \sum_{i=1}^{n} a_i \exp[-b_i s^2] + c\,, \tag{3.4.13}$$

where a_i, b_i, and c are parameters determined by a curve fitting procedure and are listed in reference 23. We found the calculated equatorial layer line intensity from a MWNT with 5 shells whose diameters were 4.326 nm, 5.04 nm, 5.606 nm, 6.3 nm or 6.357 nm, 6.996 nm, respectively, and the corresponding chiral indices were (44, 18), (52, 20), (58, 22), (65, 25) or (65, 26), (72, 28), agreed well with the experimental equatorial layer line intensity profile (Fig. 4.3.2).

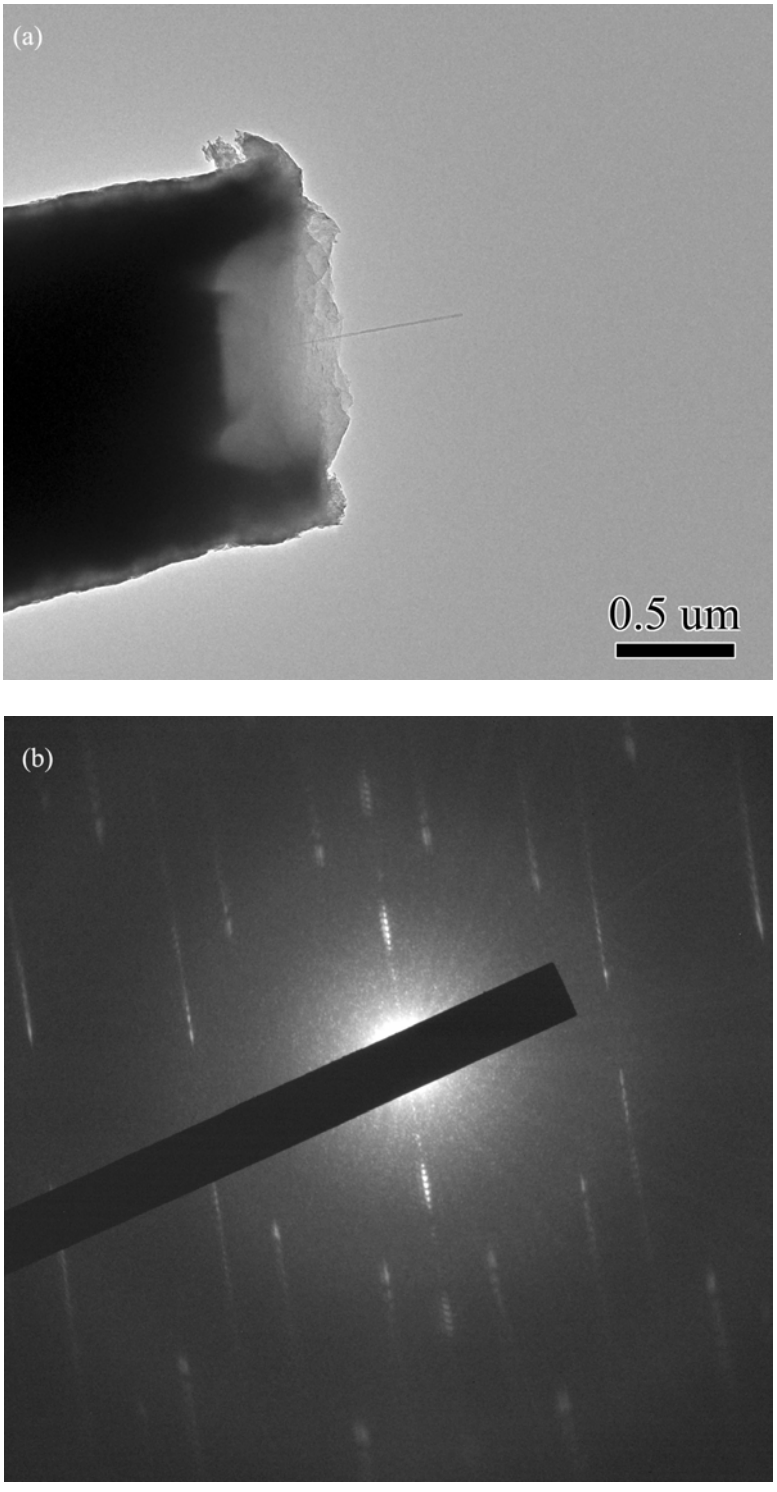

Fig. 3.4.1 (a) Low magnification TEM image of a single MWNT extruding from a carbon fiber with a 1.3 μm diameter. The inner and outer diameter of this MWNT was estimated to be about 4 nm and 8 nm, respectively. (b) The corresponding nanobeam electron diffraction pattern. This pattern suggests all the shells have close v/u ratios.

Table 3.4.1. possible *v/u* ratios and diameters (chiral indices).

v/u	diameter (nm)
0.3793	2.803 (29, 11), 5.606 (58, 22), 8.409 (87, 33)
0.3846	3.78 (39, 15), 5.04 (52, 20), 6.3 (65, 25)
0.3889	3.498 (36, 14), 5.274 (54, 21), 6.996 (72, 28)
0.3913	2.238 (23, 9), 4.476 (46, 18), 6.714 (69, 27)
0.3929	2.727 (28, 11), 5.454 (56, 22), 8.181 (84, 33)
0.4000	3.912 (40, 16), 4.401(45, 18), 4.89 (50, 20), 5.379 (55, 22), 5.868 (60, 24), 6.357 (65, 26), 6.846 (70, 28)
0.4091	4.326 (48, 18), 6.489 (66, 27)

Table 3.4.2. Possible combinations of diameter (chiral indices) for each shell.

list of possible diameters and chiral indices (nm) for each shell
3.78 (39, 15), 4.401 (45, 18), 5.04 (52, 20), 5.606 (58, 22), 6.357 (65, 26), 6.996 (72, 28)
3.78 (39, 15), 4.401 (45, 18), 5.04 (52, 20), 5.606 (58, 22), 6.300 (65, 25), 6.996 (72, 28)
4.326 (44, 18), 5.04 (52, 20), 5.606 (58, 22), 6.300 (65, 25), 6.996 (72, 28)
4.326 (44, 18), 5.04 (52, 20), 5.606 (58, 22), 6.357 (65, 26), 6.996 (72, 28)
4.401 (45, 18), 5.04 (52, 20), 5.606 (58, 22), 6.300 (65, 25), 6.996 (72, 28)
4.401 (45, 18), 5.04 (52, 20), 5.606 (58, 22), 6.357 (65, 26), 6.996 (72, 28)
4.89 (50, 20), 5.606 (58, 22), 6.3 (65, 25), 6.996 (72, 28)
4.89 (50, 20), 5.606 (58, 22), 6.357 (65, 26), 6.996 (72, 28)

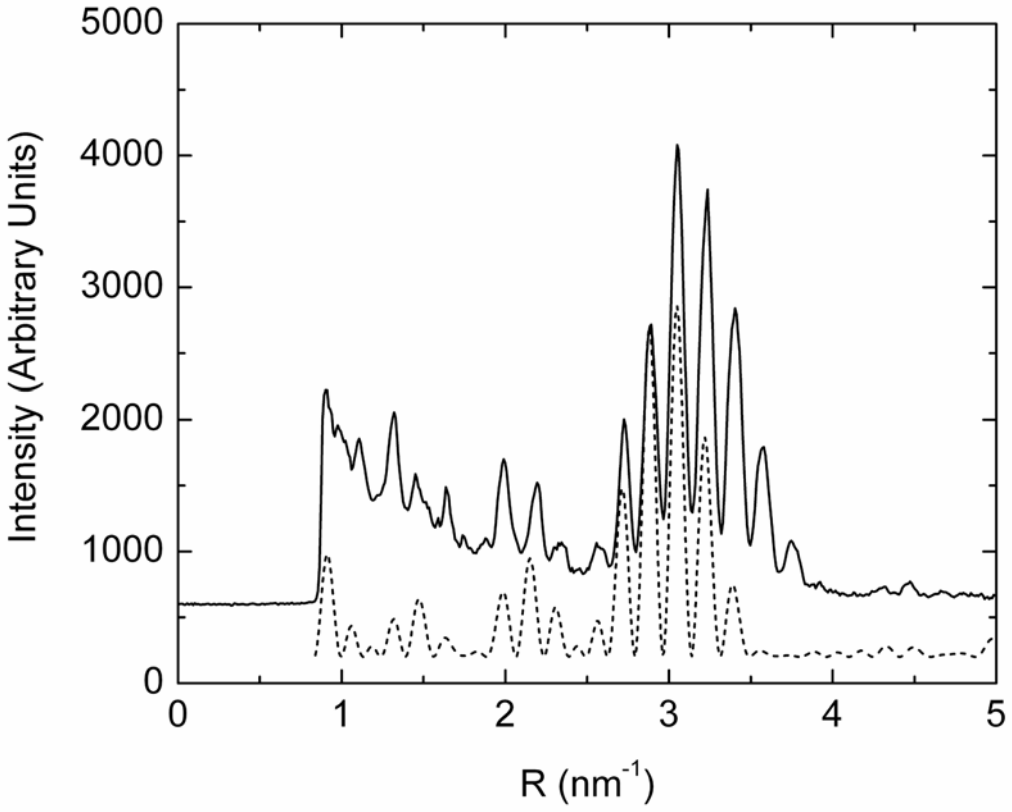

Fig. 3.4.2 Simulated (dot line) and experimental (solid line) equatorial layer line intensity profile for the MWNT shown in Fig. 3.4.1(a).

In order to unambiguously determine the chiral indices of the fourth shell, we examined the intensities of the first layer line. If the chiral indices of the fourth layer line is (65, 26), no two shells will have the same helicity. Then the whole pattern should have 2mm symmetry [21]. But the first layer line does not possess 2mm symmetry which suggests that there were two shells of the same helicity and electrons scattered from these two shells interfered with each other. Since the intensities of the first layer line are mainly governed by the νth order Bessel function, the diffraction intensities from the 2nd and 4th shells which have the same helicity are [22]

$$I_{24}(R,\Phi,l_1) = x_0^2 f^2 \{| d_2 J_{v_2}(\pi d_2 R)|^2 + | d_4 J_{v_4}(\pi d_4 R)|^2$$

$$+ 2 d_2 d_4 J_{v2}(\pi d_2 R) J_{v_4}(\pi d_4 R) \cos[(v_4 - v_2)(\Phi + \pi/2) + \Delta\varphi]. \quad (3.4.14)$$

It suggests that, when v_4-v_2 is an odd number, $I(R,\Phi,l_1) \neq I(R,\Phi+\pi,l_1)$, which means the first layer line will not possess 2mm symmetry. Therefore we can determine the fourth shell will be (65, 25). In order to further test this, the first layer line intensity profile is simulated. We should mention that, although only two shells have the same *v/u* ratio, the positions of the first layer lines from all the shells are really close. Practically we use

$$I(R,\Phi,l_1) = x_0^2 f^2 \sum_{i=1,3,5} | d_i J_{v_i}(\pi d_i R)|^2 + I_{24}(R,\Phi,l_1) \quad (3.4.15)$$

to simulate the first layer line intensity profile and the result is plotted in Fig. 3.4.3 (a, b). This calculated intensity profile agrees well with the experimental intensity profile, suggesting that this MWNT consisted of five shells whose chiral indices are (44, 18), (52, 20), (58, 22), (65, 25), and (72, 28), respectively. The atomic structure of each shell is listed in Table 3.4.3.

Table 3.4.3. Atomic structure of the MWNT shown in Fig. 3.4.1(a) determined from the electron diffraction pattern shown in Fig. 3.4.1(b).

Shell No.	*v/u*	(*u*, *v*)	Diameter (nm)	Helicity	Metallicity
1	0.4091	(44, 18)	4.326	16.39°	M
2	0.3846	(52, 20)	5.040	15.61°	S
3	0.3793	(58, 22)	5.606	15.44°	M
4	0.3846	(65, 25)	6.300	15.61°	S
5	0.3889	(72, 28)	6.996	15.75°	S

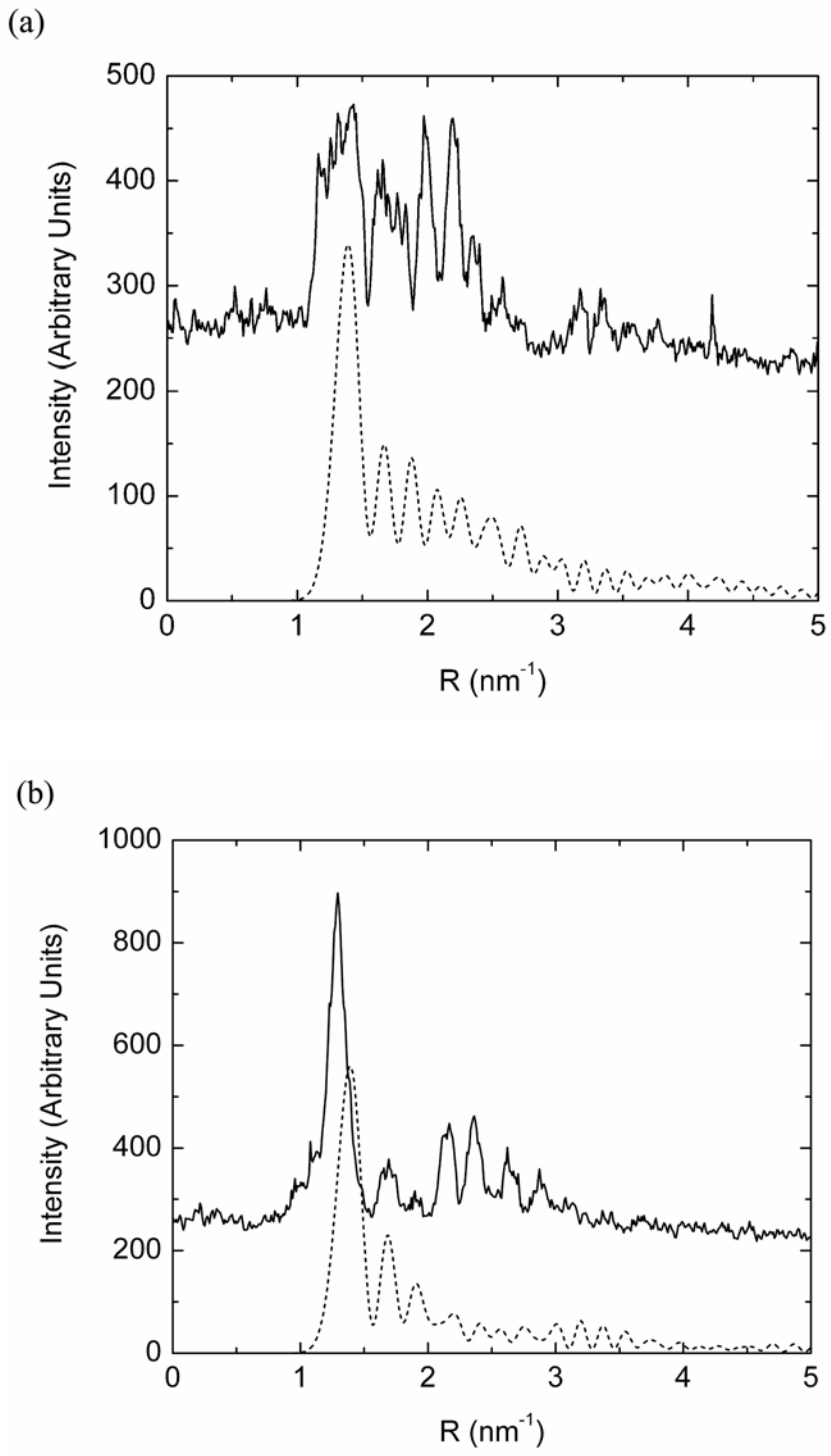

Fig. 3.4.3 (a) Experimental (solid line) and simulated (dot line) first layer line intensity profile $I(R, \Phi+\pi, l_1)$. (b) Experimental (solid line) and simulated (dot line) first layer line intensity profile $I(R, \Phi, l_1)$.

3.5 References

[1] R. T. K. Baker, M. A. Barber, P. S. Harris, F. S. Feates, and R. J. Waite, *J. Catal.* **26**, 51 (1972).

[2] R. T. K. Baker, P. S. Harris, R. B. Thomas, and R. J. Waite, *J. Catal.* **30**, 86 (1973).

[3] R. T. K. Baker, *Carbon* **27**, 315 (1989).

[4] H. M. Cheng, F. Li, X. Sun, S. D. M. Brown, M. A. Pimenta, A. Marucci, G. Dresselhaus, and M. S. Dresselhaus, *Chem. Phys. Lett.* **289**, 602 (1998).

[5] L. An, J. M. Owens, L. E. McNeil, and J. Liu, *J. Am. Chem. Soc.* **124**, 13688 (2002).

[6] W. Kim, H. C. Choi, M. Shim, Y. Li, D. Wang, and H. J. Dai, *Nano. Lett.* **2**, 703 (2002).

[7] C. J. Lee, J. Park, S. Han, and J. Ihm, *Chem. Phys. Lett.* **337**, 398 (2001).

[8] H. Kind, J. M. Bonard, C. Emmenegger, L. O. Nilsson, K. Hernadi, E. M. Schaller, L. Schlapbach, L. Forro, and K. Kern, *Adv. Mater.* **11**, 11246 (1999).

[9] H. Dai, J. Kong, C. Zhou, N. Franklin, T. Tombler, A. Cassell, S. Fan, and M. Chapline, *J. Phys. Chem. B* **103**, 11246 (1999).

[10] Y. J. Yoon, J. C. Bae, H. K. Baik, S. J. Cho, S, -J, Lee, K. M. Song, and N. S. Myung, *Chem. Phys. Lett.* **366** 109 (2002).

[11] M. J. Bronikowski, P. A. Willis, D. T. Colbert, K. A. Smith, and R. E. Samlley, *J. Vac. Sci. Technol. A* **19**, 1800 (2001).

[12] W. C. Ren and H. M. Cheng, *J. Phys. Chem. B* **109**, 7169 (2005).

[13] L. -C, Qin, and S. Iijima, *Mater. Lett.* **30**, 311 (1997).

[14] L. -C, Qin, *J. Mater. Res.* **9**, 2450 (1994).

[15] A. A. Lucas, V. Bruynincks, and Ph. Lambin, *Europhys. Lett.* **35**, 355 (1996).

[16] W. Cochran, F. H. C. Crick, and V. Vand, *Acta Cryst.* **5**, 581 (1952).

[17] Ph. Lambin and A. A. Lucas, *Phys. Rev. B* **56**, 3571 (1997).

[18] Z. Liu and L. -C. Qin, *Chem. Phys. Lett.* **400**, 430 (2004).

[19] Z. Liu, Q. Zhang, and L. -C. Qin, *Phys. Rev. B* **71**, 245413 (2005).

[20] S. Amelinckx, A. Lucas, and P. Lambin, *Rep. Prog. Phys.* **62**, 1471 (1999).

[21] Z. Liu and L. -C, Qin, *Chem. Phys. Lett.* **402**, 202 (2005).

[22] Z. Liu, Q. Zhang, and L. -C Qin, Appl. Phys. Lett. **86** 191903 (2005).

[23] P. A. Doyle and P. S. Turner, *Acta. Cryst. A* **24**, 390 (1968).

Chapter 4. Cold Field Emission Properties of a Single Carbon Nanotube

4.1 Introduction

Carbon nanotubes have attracted much attention as a candidate for field emitters due to their nanometric dimensions and robust structure since 1995 [1-3]. In carbon nanotubes, each carbon atom is bound to three other carbon atoms by sp^2 covalent bonds. As a result, nanotubes can stand intense elelctric field and high temperature. It has also been reported that carbon has one of the lowest sputter coefficients which is an advantage for a field emission electron source [4]. Recently a tremendous amount of effort has been made to study the field emission properties of carbon nanotubes. Experimental results have shown that carbon nanotubes possess many excellent field emission properties such as low turn-on field [1,2,3], high field enhancement [1,2,3], narrow energy distribution [5,6,7], long lifetime [8,9], stable emission current [10], and high brightness [11, 12].

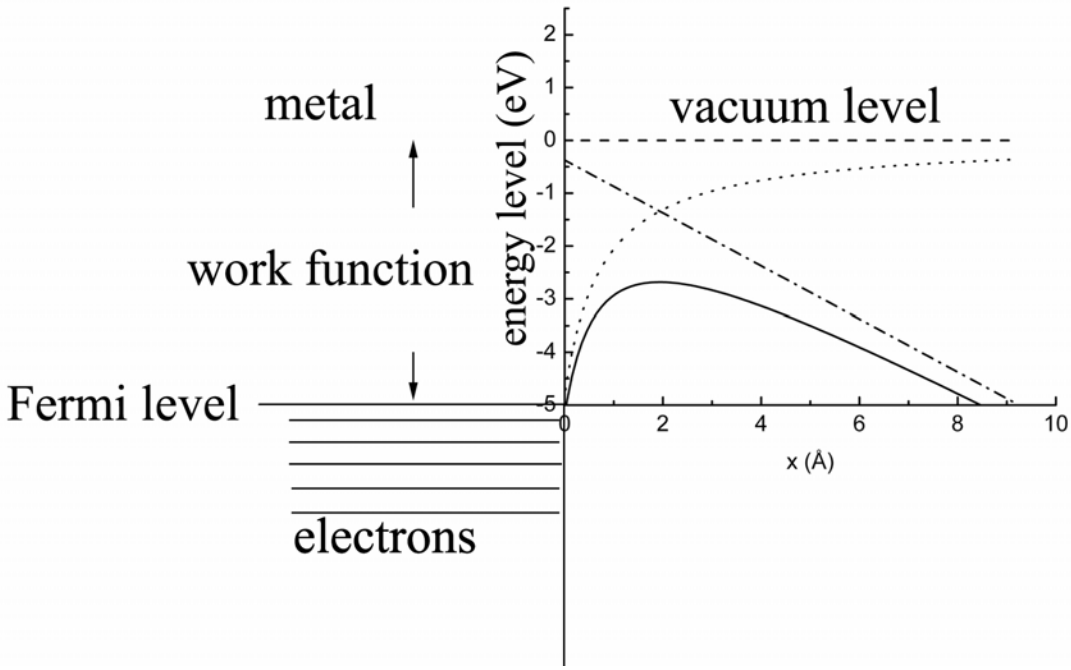

Fig. 4.1.1. Surface potential barrier with image potential correction (solid line) and without image potential correction (dash dot line) diagram at a metal (with a 5 eV work function) surface in the presence of a 0.5 V/Å electric field. Dot line is the image potential.

Field emission is a process in which electrons tunnel through the traditional bent forbidden barrier into the vacuum under an intense electric field. The Fowler-Nordheim (F-N) theory has been developed to interpret this phenomenon based on the free metal theory [13,14]. Although nanotubes can be either metallic or semiconducting, the Fowler-Nordheim (F-N) theory has been adopted to study the electron emission from the carbon nanotubes. For a metal with work function ϕ, the emission current density can be expressed as a function of the electric field at zero temperature [14]:

$$J(T=0,F,\phi)=\frac{e^3F^2}{8\pi h\phi t^2(y)}Exp[-\frac{8\pi(2m)^{1/2}v(y)}{3he}\frac{\phi^{3/2}}{F}] \tag{4.1.1}$$

with

$$F=\beta V\ . \tag{4.1.2}$$

Although Eq. (4.1.1) was developed for zero temperature, it is fairly accurate at room temperature. To a good approximation, $t^2(y)=1.1$ and $v(y)=0.95-y^2$ lead to a more straightforward equation [15]:

$$J(T=0,F,\phi)=1.5\times10^{-6}\frac{F^2}{\phi}\exp[\frac{10.4}{\phi^{1/2}}]\exp[-6.44\times10^7\frac{\phi^{3/2}}{F}]\ \text{Acm}^{-2} \tag{4.1.3}$$

for F in V/cm and ϕ in eV. Plugging Eq. (4.1.2) into Eq. (4.1.3), and applying the natural logarithm, we can obtain

$$\ln(\frac{I}{V^2})=-6.44\times10^7\frac{\phi^{3/2}}{\beta}\frac{1}{V}+\ln(1.5\times10^6A\frac{\beta^2}{\phi})+\frac{10.4}{\phi^{1/2}}, \tag{4.1.4}$$

where A is the emission area. A $Ln(I/V^2)$ *vs.* V^{-1} plot (F-N plot) will generate a straight line if the emission mechanism follow the F-N theory. The slope of the F-N plot will be

$-6.44\times10^{7}\phi^{3/2}/\beta$ and the y-intercept will be $\ln[1.5\times10^{-6}A\beta^{2}/\phi]+10.4/\phi^{1/2}$. If the work function is known, then the field enhancement factor β and the emission area A can be calculated from the slope b and the y-intercept y_{int} of F-N plot as

$$\beta = -\frac{6.44\times10^{7}\phi}{b} \text{ cm}^{-1} \tag{4.1.5}$$

and

$$A = \frac{\phi}{1.5\times10^{-6}\beta^{2}} Exp[y_{\text{int}} - \frac{10.4}{\sqrt{\phi}}] \text{ cm}^{2} \tag{4.1.6}$$

for ϕ in eV.

4.2 Fabrication and Manipulation of Single Nanotube Field Emitters

The field emission properties of carbon nanotube films have been widely studied. However, these same properties of single nanotubes are still not well studied due to the difficulties in fabricating single nanotube field emitters. In 1995, Rinzler et al. mounted a single CNT onto a support tip using micromanipulators and an optical microscope [3]. Due to the limited resolution of the optical microscope, it was hard to tell the difference between an individual CNT or a small CNT bundle. de Jonge developed a more precise method to mount an individual CNT to a tungsten tip by using a piezo-driven nanomanipultor in an SEM [7,16]. Other similar methods were used to mounts nanotubes on the scanning probe tips [17,18]. An individual CNT could also be picked up by atomic force microscope (AFM) tip [19].

In Chapter 3, we have established a CVD method to fabricate a fiber-CNT structure. We have developed an efficient and precise method to fabricate single carbon nanotube field emitters with good controllability. In order to make the nanotube well aligned, a copper

ribbon, coated with conductive carbon glue, with a small groove is used as the support. When this support was carefully approaching the free end of a fiber, we positioned the fiber to be in the groove by using a micromanipulator. After the fiber was positioned parallel to the groove and firmly attached to it, the copper support was moved to the opposite direction until the fiber was fractured. Then the entire structure was examined in a transmission electron microscope (TEM) using a custom-designed sample holder due to the large size of support structure. This custom-designed sample holder has an extra groove at the center, which is connected with the 3 mm diameter hole where the grid is usually held (Fig. 4.2.1). The copper ribbon support structure can be positioned inside the groove and the carbon fiber is position at the center of the hole so that the CNT can be exposed to electron beam for imaging. We have demonstrated the effectiveness of this method by mounting 10 CNTs on the support structure. The corresponding length and diameter of each CNT has been measured and listed in Table 4.2.1. Nine CNTs have diameters between 4 nm and 12 nm, which suggest a rather narrow diameter distribution. The angles of the CNTs relative to the support structures were also measured. Eight CNTs are within a 10º cone angle, which suggests that this method has a good controllability over the alignment.

Fig. 4.2.2(b) shows the morphology of an individual multi-wall carbon nanotube extruding from the carbon fiber from which the length, diameter, and wall number were characterized. High-resolution transmission electron microscopy (HRTEM) images revealed that this carbon nanotube is 24 nm in diameter and 4.4 μm in length. It has 20 walls with a wall thickness of 7.8 nm. Although the nanotube end could not be imaged clearly due to thermal vibrations, the field emission pattern showed a ring-like structure, suggesting that this nanotube had an open end. When emerging from a surface potential barrier, the electrons

have very little kinetic energy and therefore will follow the lines of force. Since the field emitters are conductors and have an equipotential surface, all the lines of force are orthogonal to the emitters' surface and diverge radially outwards from the emitter's tip. Ideally, electrons emitted from an open-end nanotube tip are radially accelerated and form a circular ring on the phosphor screen. The HRTEM images also revealed that the nanotube was well crystallized, attributed to the high synthesis temperature. It is usually desirable to have a well-crystallized nanotube in order to obtain an emitter of long emission lifetime [20].

Table 4.2.1. The length l, diameter d and angle θ relative to the axis of support structure from 10 mounted individual MWNTs.

Mounted MWNT	L (μm)	d (nm)	θ°
1	0.7	7.3	2
2	0.5	12	4
3	4.4	24	5
4	1.1	8	9
5	1.4	6	1
6	1.1	4	4
7	0.5	5.5	14
8	0.3	6.5	8
9	1.4	10	13
10	2.6	11	3

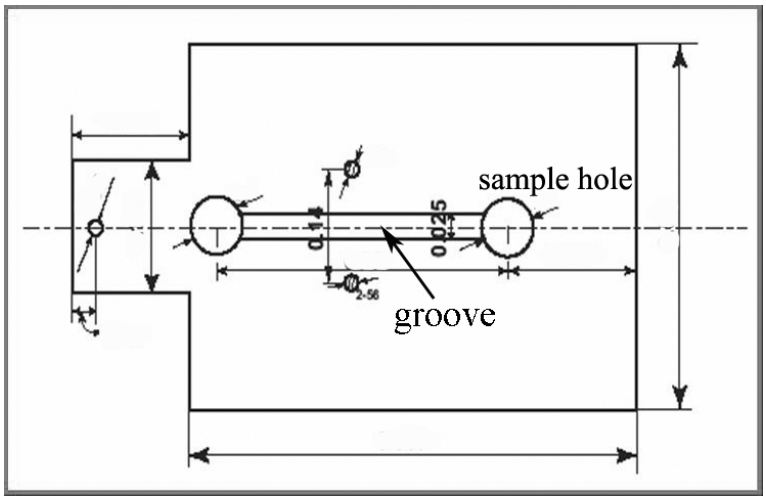

Fig. 4.2.1 The custom-designed JEM-2010F holder for imaging the fiber-CNT on a copper ribbon, which is positioned in the groove so that the fiber is located at the center of the sample hole.

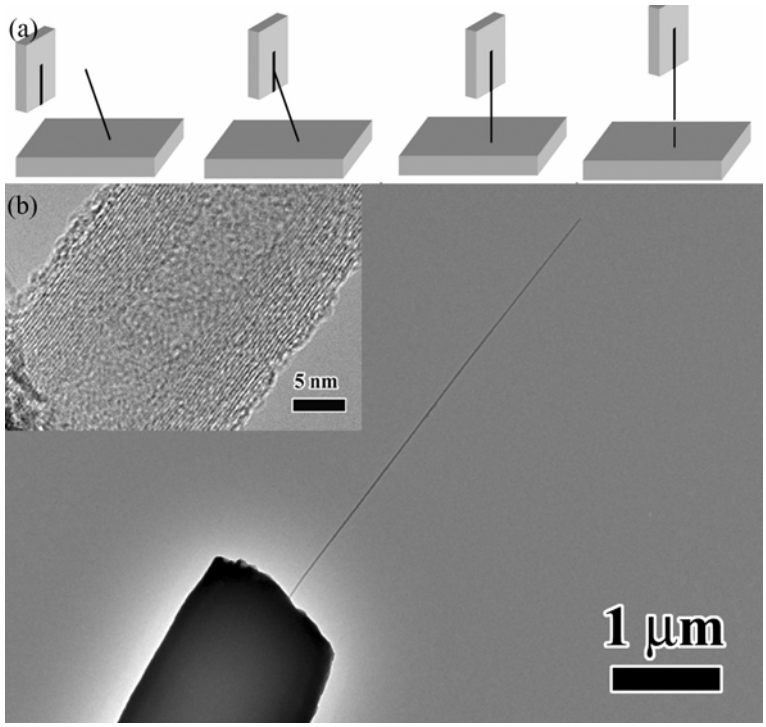

Fig. 4.2.2 (a) Schematic depicting the process by which a carbon fiber was fractured, picked up and aligned with a copper ribbon, which has a pre-carved groove on it. (b) Morphology of a single CNT emitter, in which a multi-wall carbon nanotube was extruded from a carbon fiber. The inset HRTEM image reveals that this MWNT has 20 well crystallized walls, 24 nm diameter and 4.4 μm length.

The field emission properties and optical properties depend strongly on the length of the carbon nanotube. For a nanotube standing between two parallel electrodes, the field enhancement factor is [21, 22]:

$$\beta = 1.2\left(2.15 + l/r\right)^{0.9} / d\,, \tag{4.2.1}$$

where d is the inter-electrode distance, r is the radius of the nanotube and h is the nanotube length. For a longer nanotube, it will have a larger field enhancement factor and a lower turn-on field, which is the electric field it needs to extract a 10 nA current. But a longer nanotube will also have larger vibration amplitudes that can result in poor beam coherence and larger virtual source [23]. For future applications as a point source in the electron microscopes, it is important that the electrons emitted from the CNTs have a high degree of coherence. This is because the coherence can improve the high resolution phase contrast image [24]. The vibrations will also reduce brightness dramatically. We have developed an in-situ TEM cutting technique to control the length of carbon nanotubes. The JEM-2010F was operated at 200 kV in the nanobeam electron diffraction (NBD) mode. A 0.7 nm diameter electron probe was used to cut the nanotube. First, the electron probe was positioned at the edge of the nanotube. Then the beam was moved across the nanotube at a speed of 3 nm/min. Fig. 4.2.3 showed that this process cut a nanotube body completely into two halves and made the neighbor walls connected by bridging carbon atoms. These bridging carbon atoms eliminated the tangling bonds and were expected to improve the emission stability.

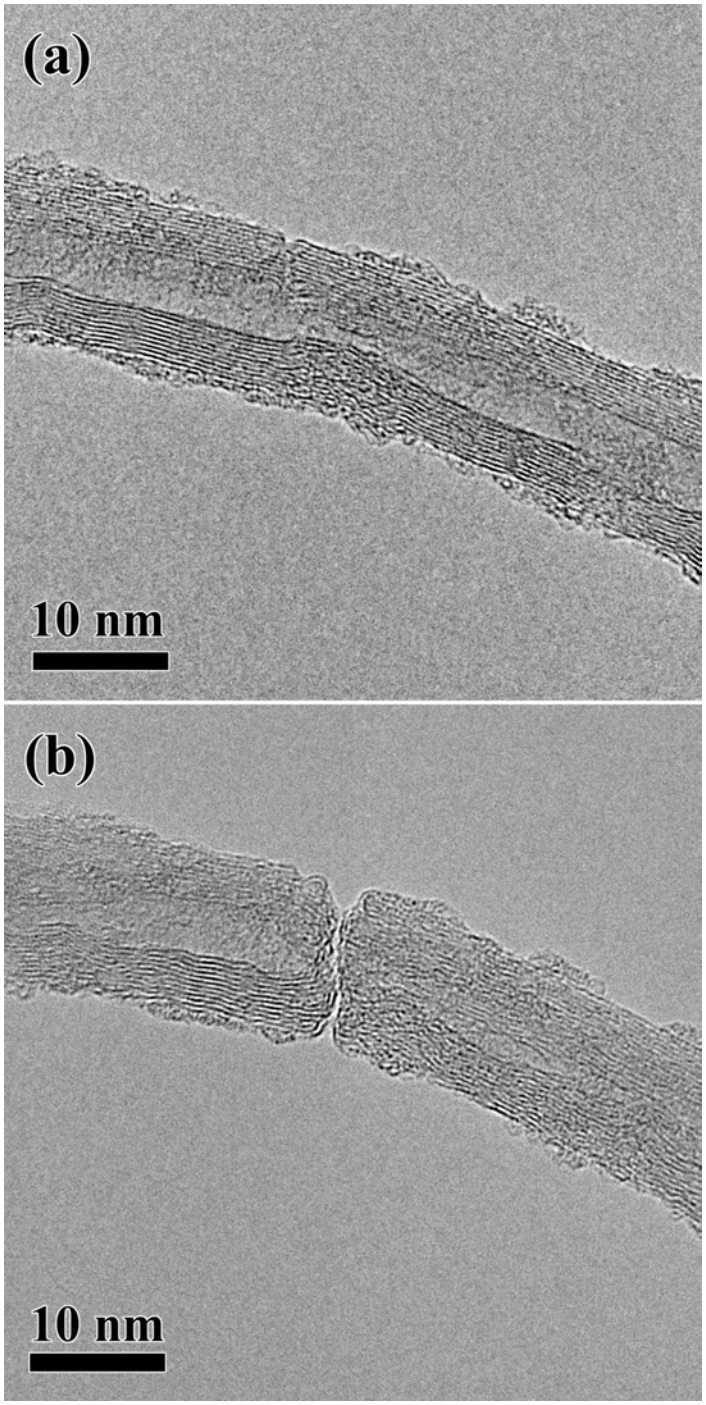

Fig. 4.2.3 (a) HRTEM image a MWNT. (b) The corresponding MWNT was cut by a 0.7 nm diameter electron probe and the cutting process made the neighbor walls connected by bridging carbon atoms.

4.3 Cold Field Emission Measurements

The field emission measurements were carried out in a vacuum chamber operated at 10^{-7} – 10^{-8} Torr. The vacuum chamber is baked overnight. The fiber-CNT structures attached to the copper ribbon were carefully positioned 300 μm from the anode under a calibrated optical microscope.

Field emission measurements at room temperature were carried out on four single CNTs. Fig. 4.3.1(a, b) shows the I-V curves and corresponding F-N plots of CNT No. 1 – 3, respectively. The TEM images of CNT No.1 - 4 are shown in Fig. 4.3.2(a, b, c, d), respectively. All three curves follow the Fowler-Nordheim theory in the low current range. Systemic deviations from the F-N model are also observed in the high current range. These deviations correspond to a strong saturation in the range of 1.5 μA to 3 μA. These deviations are not due to space charge effect because the saturation current density is only 1.8×10^{6} A/cm^2, which is an order of magnitude lower than the space charge limit. This strong saturation may be due to the low carrier density at the Fermi level [25]. The maximum stable current we draw from an individual MWNT emitter is 3.5 μA. A measurement of 10 μA was also recorded, but it was not stable and dropped back to 3.5 μA quickly.

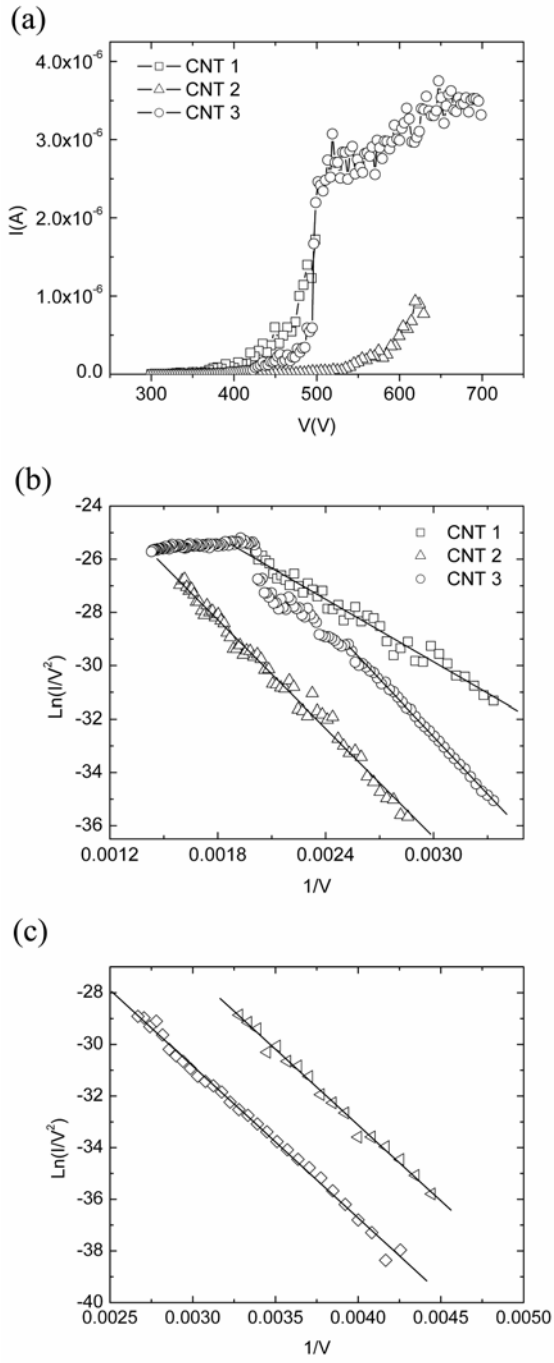

Figure 4.3.1 (a) Field emission measurement of three individual MWNTs (CNT No. 1-3) at room temperature. The emission current was measured as a function of the extraction voltage. The TEM images of CNT No.1 - 3 are shown in Fig. 4.3.2(a, b,c), respectively. (b) Corresponding Fowler-Nordheim plots and linear fits to the Fowler-Nordheim plots from CNT No. 1 - 3. (c) The F-N plot from CNT No. 4 (Fig. 4.3.2(d)) before (triangle) and after (square) cleaning.

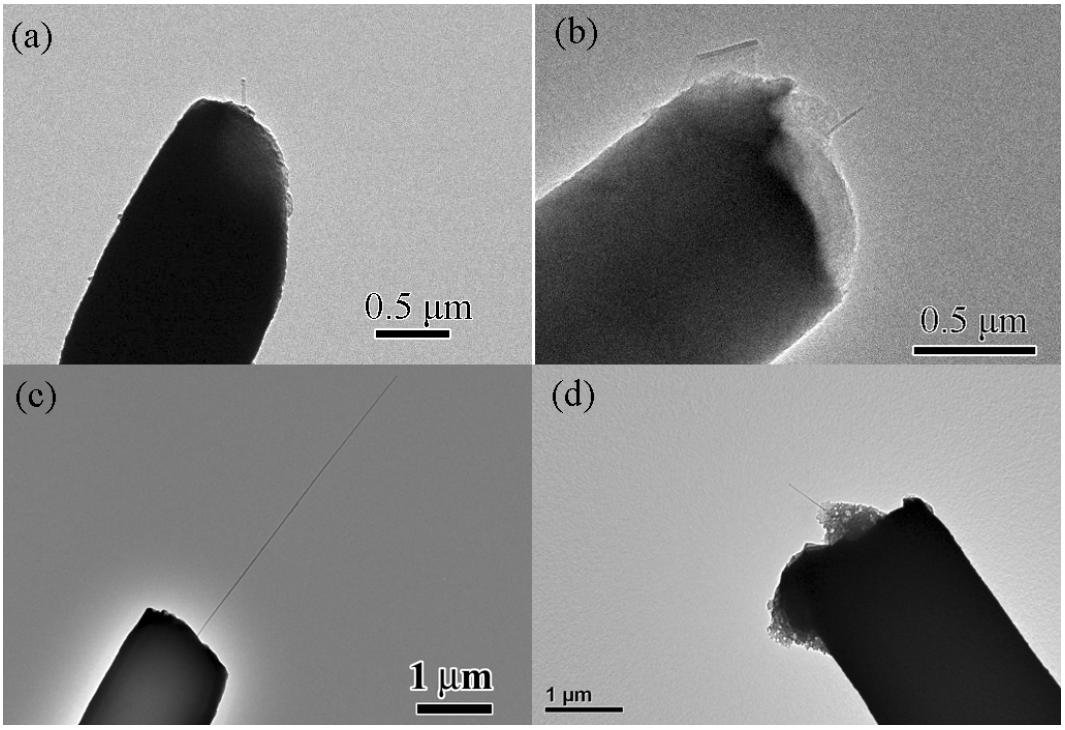

Fig. 4.3.2. Field emission experiments were carried out on four single CNTs. (a) CNT No.1 (b) CNT No.2 (c) CNT No.3 (d) CNT No.4.

Table 4.3.1. Field emission data from four individual MWNTs (CNT No.1 – 4)

CNT No.	l (μm)	d (nm)	$\beta/10^7$ (m^{-1}) $\phi = 5.1 \pm 0.2$ eV	$\beta'/10^7$ (m^{-1})	A (m^2) $\phi = 5.1 \pm 0.2$ eV
1	0.5	24	1.9 ± 0.2	1.7	$(1.3 \pm 0.4)\times10^{-18}$
2	0.5	12	1.09 ± 0.09	3.3	$(3.2 \pm 0.7)\times10^{-17}$
3	4.4	24	1.04 ± 0.07	1.7	$(4.3 \pm 0.1)\times10^{-15}$
4	1.1	8	1.2 ± 0.1	5	$(3 \pm 2)\times10^{-14}$
4(cleaned)	1.1	8	1.2 ± 0.1	5	$(1.4 \pm 0.9)\times10^{-14}$

According to the Fowler-Nordheim equation for field emission, the slope of the F-N plot is $-6.44\times10^{7}\phi^{3/2}/\beta$. The β factor was calculated from the slope of the three F-N plots given in Fig. 4.3.1(b) with an assumption that the work function is 5.0 ± 0.2 eV [26,27,28,29]. The three β factors are calculated and listed in Table. 4.3.1. The error bar of the field enhancement factor β consists of two parts. The first part is the error induced by the fitting of the F-N plots. The second part is induced by the uncertainty of the work function of the carbon nanotube. The true error bars have been calculated and listed in Table. 4.3.1. To eliminate the complexity of the absorbed species, the CNT No. 4 has been cleaned by heating it at 1200ºC. The F-N plots before and after cleaning are shown in Fig. 4.3.1(c). It was found that after cleaning, the slope of the F-N plot only changed 2%. Thus the measured field enhancement factors of CNT No. 1 - 3 are still valid even though no cleaning was performed.

For an isolated emitter with a hemispherical tip on a cylinder, $\beta' = 1/(5r)$ is a good approximation where r is the radius of curvature of the tip [30]. Using this approximation, the field enhancement factors β' have been predicted and compared to the experimental values β. It is found that this approximation can introduce a factor of 4 errors, which suggests that $\beta' = 1/(5r)$ is not suitable for the fiber-CNT structures. This discrepancy is attributed to two reasons: (a) the nanotube measured here has an open end and (b) the field enhancement from the micron-sized carbon fiber was not considered.

4.4 An empirical Model to Calculate Field Enhancement Factor

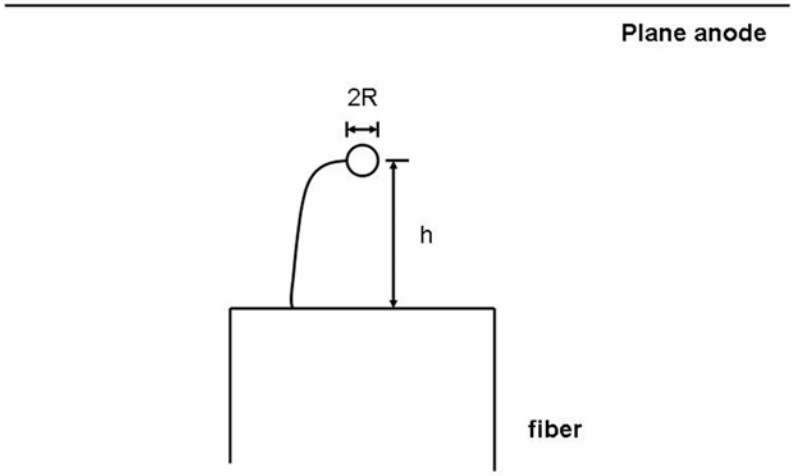

Fig. 4.4.1 The "floating sphere on emitter-plane potential" model. A same diameter cylinder is used to substitute carbon fiber. A sphere with a diameter 2*R* (*R* is the radius of carbon nanotube cap and *h* is the nanotube length) is positioned *h* from the top plane of the cylinder. This sphere is connected with the fiber so that the sphere and the fiber have the same potential.

In order to better understand the field enhancement factor β of the fiber-CNT emitter, a cylinder to plane geometry model is built. Here we use a same diameter cylinder to substitute a fiber with a flat top cross section. For the morphology of CNT No. 3 (Fig. 4.3.2(c)), the diameter of cylinder is 1.4 μm. Although the overall electric field around the cylinder is neither uniform nor parallel, the near-axis field can be treated as parallel, but the field is not uniform. We can use a 'floating sphere on emitter-plane potential' model (Fig. 4.4.1) [22] to estimate semi-analytically the electric field at the apex of a closed nanotube. First, a sphere is positioned at the cylinder axis and h from cylinder top. Considering the size of the sphere (about 10 nm), we can assume that the electric field F_M around the sphere is uniform and parallel. The field created by the induced surface charge density can be described by a dipole located at the center of the sphere, and the dipole generates a field $F_{d,a} = 2F_M$ at the apex of the sphere. The potential difference $\Delta\phi$ between the sphere and the cylinder top can be removed by placing a charge Q at the center of sphere. This charge Q also will create a potential variation across the cylinder top. To correct this, we have to put an image charge Q_{im} ($-Q$) at a distance h behind the cylinder top plane. We must mention that these two charges will create a potential variation on the side surfaces of the cylinder. Considering the cylinder diameter and h are much larger than the sphere radius R, this potential variation is small. In order to reduce the complexity, this potential variation is ignored. To keep the potential of sphere equal to that of cylinder top,

$$(Q/4\pi\varepsilon_0)(1/R - 1/2h) = \Delta\phi\,, \tag{4.4.1}$$

and

$$(Q/4\pi\varepsilon_0) = \Delta\phi/[2Rh/(2h-R)]\,. \tag{4.4.2}$$

Assuming $R \ll h$, and only considering the second-order expansion, the field contribution from Q and Q_{im} will be

$$F_Q \cong [1 + \frac{R}{2h} + \frac{R^2}{4h^2}]\Delta\phi / h, \tag{4.4.3}$$

and

$$F_{im} \cong -\frac{R\Delta\phi}{4h^2}. \tag{4.4.4}$$

There are other terms which contribute to the electric field at the sphere apex such as the image of a dipole in the cylinder top and the image of charge Q_{im} in the sphere. If $R \ll h$, then both these terms are small in comparison with the terms already considered. So the electric field at the apex of the sphere is

$$F_{apex} = F_M + F_{d,a} + F_Q + F_{im} \cong 3F_M + \frac{\Delta\phi}{h}(0.5 + \frac{h}{R}). \tag{4.4.5}$$

Then the field enhancement factor β will be

$$\beta \cong [3F_M + \frac{\Delta\phi}{h}(0.5 + \frac{h}{R}]/V, \tag{4.4.6}$$

where V is the voltage applied between the cylinder and the planar anode. This formula is not an analytical result, but it can be used to predict some field emission properties of the fiber-CNT structure. When the length of a nanotube is small, numerical calculations show that F_M and $\frac{\Delta\phi}{h}$ will be large; this is due to the field enhancement from the fiber. This explains how two nanotubes with different aspect ratio standing on similar fiber can have almost the same field enhancement factor β, which was observed in experiment. The above formula has been proven to over estimate the field enhancement factor for both closed and open carbon nanotubes.

We have developed an improved model to correlate the β factor with the physical parameters of the fiber-CNT emitter. For a model that has a nanotube standing between two planar electrodes with separation *d*, the electric field at the nanotube tip is [22,31]:

$$F = \gamma_{CNT} F_0 , \tag{4.4.7}$$

where $F_0=V/d$ and γ is a factor that depends on the geometrical attributes of the nanotube such as the cap structure, length *l* and radius *r*. For a capped nanotube [22]

$$\gamma_{CNT} = 1.2(2.15 + l/r)^{0.9} , \tag{4.4.8}$$

and for an open nanotube [31]

$$\gamma_{CNT} = 0.62 \times l/r + 0.14 \times l/w + 7 \tag{4.4.9}$$

where *w* is the wall thickness.

To improve the calculations, here we use a cylinder with a flat top plane and of the same diameter as the carbon fiber as the cathode on which the nanotube is standing. Based on a multistage model, we assume that the electric field at the tip of a nanotube standing between a cylindrical cathode and a planar anode can also be described by [32]

$$F = \gamma_{CNT}\gamma_{fiber}\frac{V}{d} = \gamma_{CNT} F_M , \tag{4.4.10}$$

and from Eq. (4.1.2) β can be expressed as

$$\beta = F/V = \gamma_{CNT} F_M / V , \tag{4.4.11}$$

where F_M is the reference electric field along the cylinder axis when the nanotube is absent. For the geometry shown in Fig. 4.2.2(b), the electric field was numerically calculated by setting V = 300 V (anode is at 0 V) and d = 300 μm using LORENTZE (developed by Integrated Engineering Software Inc.). At the cylinder axis, 4.4 μm from the cylinder top

plane, a value $F_M = 0.98\times10^7$ V/m was obtained. The calculated field enhancement factor β is 1×10^7 m^{-1}, which is very close to the experimental value $(1.04 \pm 0.07)\times10^7$ m^{-1}.

Although Eq. (4.4.11) is an empirical formula, it is also physically appealing. Firstly, the F_M/V term is independent of V, which is confirmed by the calculations. The β factor is not related to the voltage applied between the electrodes. Secondly, F_M / V takes into account both the geometry of fiber and the inter-electrode distance，which will make the β factor vary with the inter-electrode distance. This agrees with the experimental results [32,33].

4.5 Field Emission Microscopy

Field emission microscopy, invented by Müller in 1937 [34], is a useful method to image the field emitter tip surface. The mechanism for FEM can be interpreted as electrons emerging from a surface potential barrier having very little kinetic energy and therefore will follow the lines of force, since the field emitters are conductors and have an equipotential surface. Thus all the lines of force are orthogonal to the emitters' surface and diverge radially outwards from the emitter's tips. Ideally, electrons emitted from a hemispherically capped nanotube tip will reach the spherical conducting phosphor anode and generate a magnified image of the tip. The magnification will be *d/r*, where *d* is inter-electrode distance and *r* is the radius of the nanotube tip. Practically, the nanotube side-walls will reduce the field at the tip and compress the lines of force toward the tube axis direction, reducing the magnification by a factor of 1.5 (Fig. 4.5.1) [29]. Thus, for a hemispherically capped nanotube, the magnification is *d/(1.5r)*.

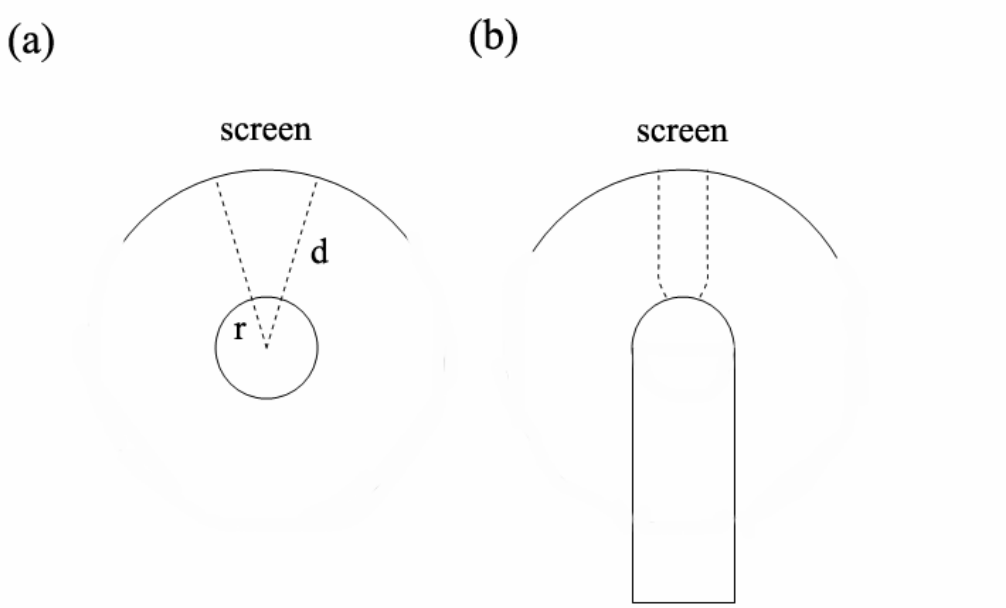

Fig. 4.5.1 Schematic diagram of electron trajectories from (a) a sphere and (b) a hemispherically capped nanotube.

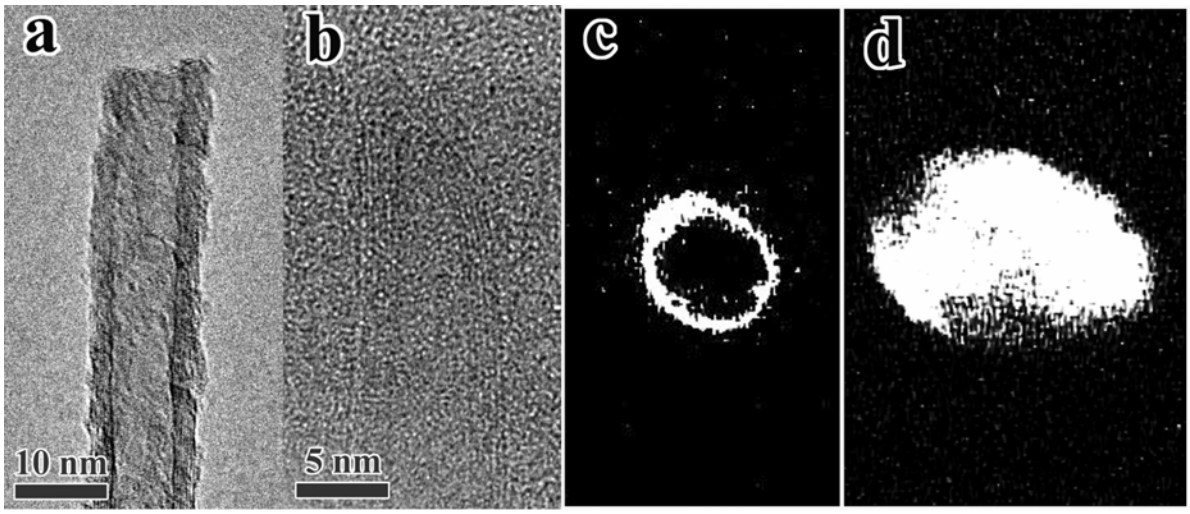

Fig. 4.5.2 HRTEM images of emitters with (a) open and (b) capped nanotubes and the field emission patterns: (c) and (d) were obtained from emitters shown in (a) and (b), respectively.

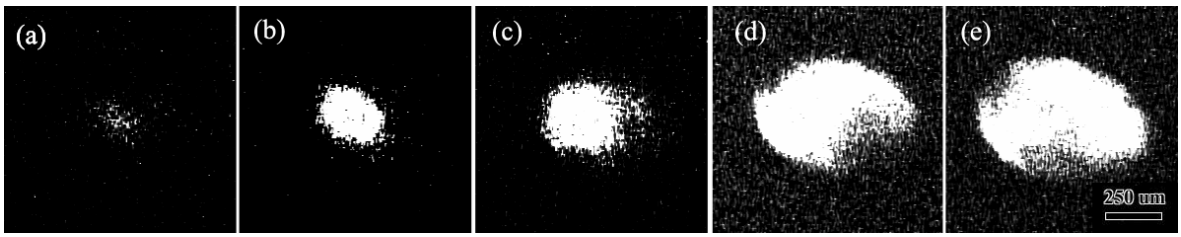

Fig. 4.5.3 Field emission patterns from a single nanotube with a conical cap (Fig.4.5.2b) at (a) 750 V and 5.2 nA, (b) 775 V and 23 nA, (c) 800 V and 35 nA, (d) 825 V and 40 nA, and (e) 875 V and 87 nA.

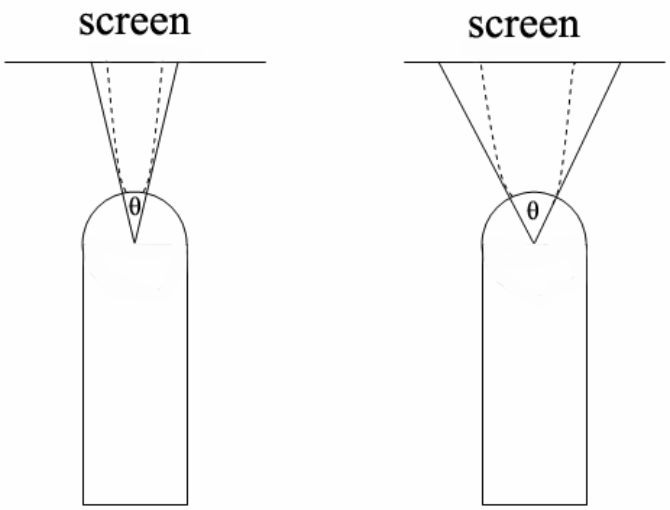

Fig. 4.5.4 Schematic diagram of electron trajectory (dash line) and emission angle θ at low electric field (a) and high field (b).

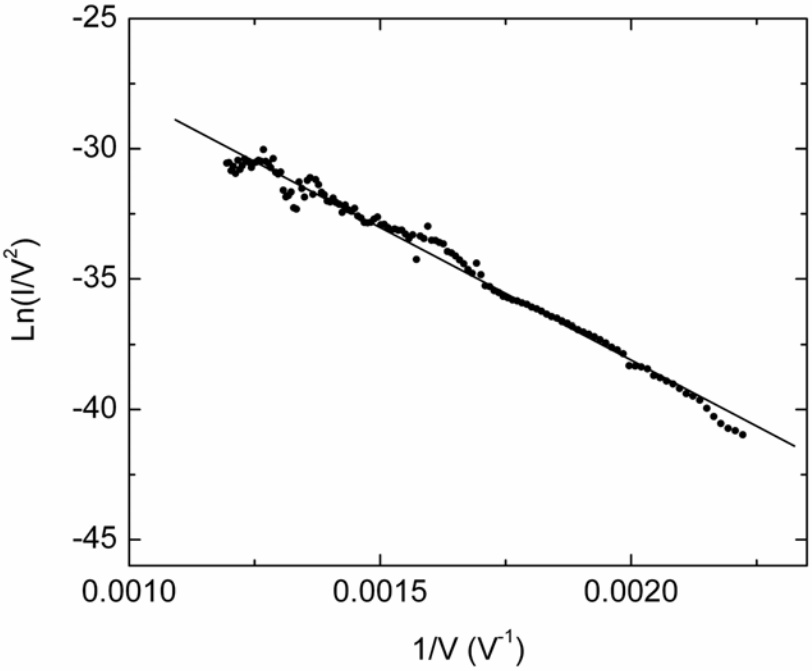

Fig. 4.5.5 F-N plot from a single nanotube (Fig.4.5.2(b)); the field enhancement factor of this nanotube was calculated to be 6.7×10^6 cm^{-1} with a 4.8 eV work function.

We have imaged the tips of two single nanotubes and measured the corresponding field emission patterns. The experiments clearly suggest that electrons emitted from an open end nanotube (Fig. 4.5.2(a)) will form a hollow electron beam and generate a ring pattern on the phosphor screen (Fig. 4.5.2(c)). Other groups also found similar results [35, 36]. On the other hand, a capped nanotube (Fig. 4.5.2(b)) produces a bright spot (4.5.2(d)).

We also studied the relations between the extraction voltages and the emission patterns from a single nanotube (Fig. 4.5.2(b)). It suggests that the electric field at the apex of the cap is most intense and the electrons were extracted from the apex first (Fig. 4.5.3 a, b). As the extraction voltage increases, the electrons will emit from other parts of the cap as well and form a larger field emission pattern. The inter-electrode distance is 500 μm and the estimated radius of the nanotube in Fig. 4.5.2 (b) is 2 nm. By measuring the diameter of the field emission pattern, we can calculate the emission angle within which the electrons are emitted (Fig. 4.5.4). The angle is *1.5L/d*, where *L* is the diameter of the field emission pattern and *d* is the inter-electrode distance. For Fig. 4.5.3(b,d), the emission angles were calculated to be 57° and 89° at 775 V and 875 V, respectively. The linear fit of the F-N plot (Fig. 4.5.5) was used to calculate the field enhancement factor, which was found to be 6.7×10^{6} cm^{-1} with a 4.8 eV work funciton. The electric fields at 775 V and 875 V were 0.52 V/Å and 0.59 V/Å and the corresponding emission angles were 57° and 89°, respectively.

4.6 Lifetime and Stability

The lifetime measurements of single carbon nanotubes have been reported in several papers [8,9]. The longest lifetime test was reported to be over 16 months at a current of 100 nA under a vacuum level of 10^{-10} Torr and at a temperature of 800 K [8]. Due to the

extremely small dimensions, carbon nanotubes are sensitive to the absorbed molecules. The emission fluctuation can be interpreted as that when a gas molecule is absorbed on the tip of a nanotube, the work function will change which results in a large current fluctuations. A key to maintain a stable emission current is the initial cleaning and maintaining a high vacuum level of ~10^{-10} Torr. Practically, nanotubes can be cleaned by heating them at ~ 1000 K under a high vacuum. It was also reported that a long nanotube can be heated up to 2000 K by field emission induced heating. This self-heating can drive absorbed molecules away and maintain a clean nanotube surface [37].

We tested the emission stability and lifetime of a single carbon nanotube. The experiment was carried out in a vacuum chamber operated at 10^{-7} – 10^{-8} Torr. A 2 MΩ resistor was added into the circuit to act as a ballast resistor. The time step for current measurement was 10 sec. No obvious current drop was observed in 100 hours (Fig. 4.6.1).

Fig. 4.6.2 shows the stability measurement in three hours. The maximum drift (I_{max}-I_{min})/I_{ave} was 6.5% over this period of time. During the 3 hours, 1080 current data points were collected and the distribution of current was plotted in Fig. 4.6.3. A Gaussian fit was made and the peak position was found to be 386.9 nA with a full width at half maximum (FWHM) 5.1 nA. Instead of using the maximum drift to represent the stability, we use the FWHM divided by the peak value to indicate the stability, which is 1.3% during the three hours. We also studied the short term stability in a one hour period and found that the maximum current drift was 3.6% over the 1 hour. The Gaussian fit indicated the peak value was 387.2 nA and the FWHM was 3.4 nA which gives the stability of 0.9% in 1 hour.

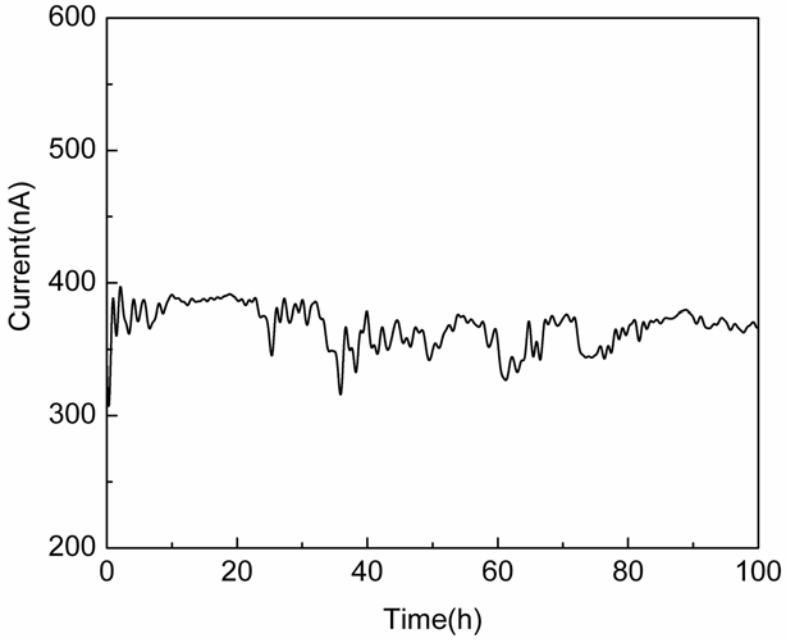

Fig. 4.6.1 Lifetime and stability test on a single carbon nanotube field emitter.

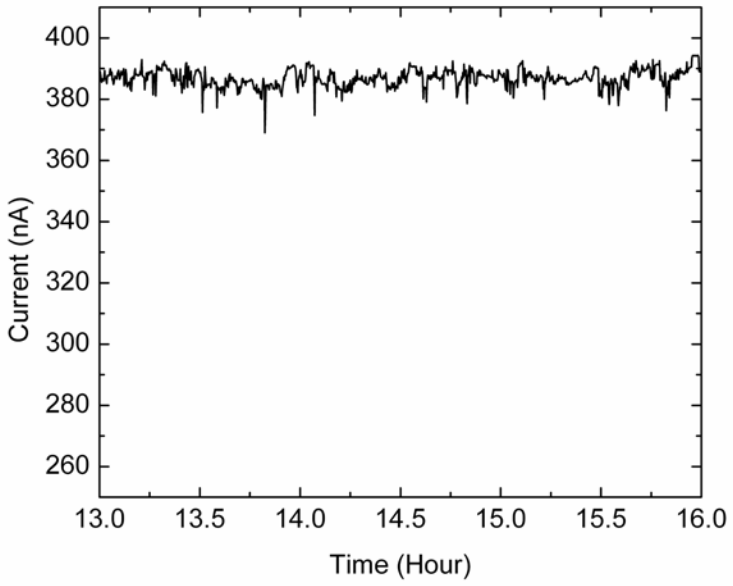

Fig. 4.6.2 Emission current stability measurement, showing 6.5 % drift over a three hours period.

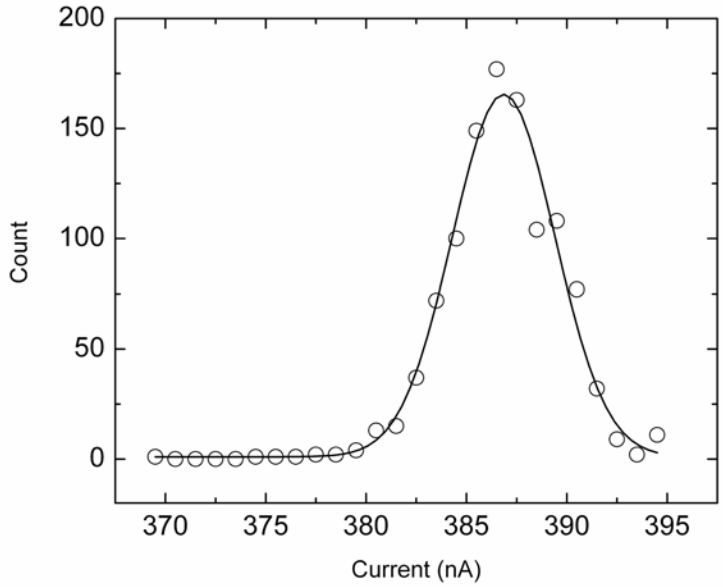

Fig. 4.6.3 Current distribution of 1081 data points over 3 hours (hollow circle) and a Gaussian fit is indicated by solid line with a peak position at 386.9 nA and a FWHM 5.1 nA.

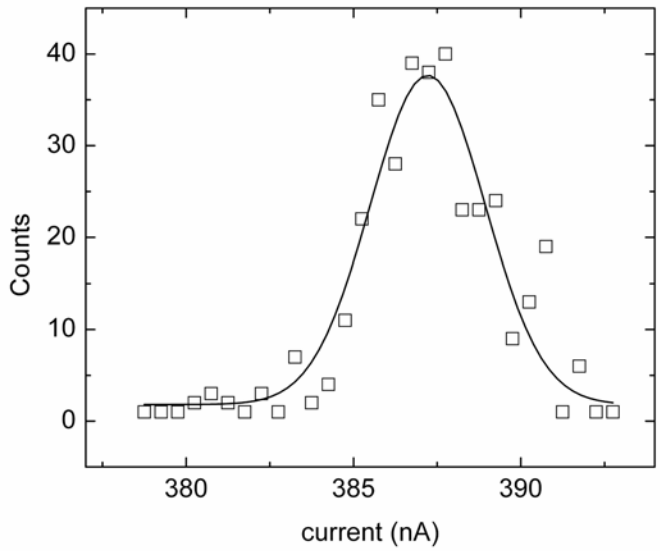

Fig. 4.6.4 Current distribution of 360 data points over 1 hour (hollow square) and a Gaussian fit is indicated by solid line with a peak position at 387.2 nA and a FWHM 3.4 nA.

4.7 Brightness Measurement

One important property of carbon nanotube field emitters is its high brightness [10]. The brightness is the current density in a unit solid angle [38]:

$$B = \frac{dI}{d\Omega}\frac{1}{\pi r_v^2}, \tag{4.7.1}$$

where r_v is the radius of the virtual source. The virtual source is the area from where electrons seem to have originated when traced back from the trajectory [39]. In practical use, brightness is usually normalized on extraction voltage U to give the reduced brightness B_r:

$$B_r = \frac{dI}{d\Omega}\frac{1}{\pi r_v^2}\frac{1}{U}. \tag{4.7.2}$$

Reduced brightness is very important for the future applications of carbon nanotube in high precision analytical instrument such as the transmission electron microscope (TEM). At high magnification, a high brightness will provide a higher beam intensity to make high resolution imaging feasible.

The virtual source size of carbon nanotubes can be measured using the Fresnel fringe method [40]. The first nanotube brightness measurement was done in a point electron microscope [10]. For a nanotube with a hemispherical cap, the radius of the virtual source size is slightly less than the physical radius of the nanotube. For a flat capped nanotube or an open nanotube, the virtual source size is approximately equal to the radius of the nanotube [8].

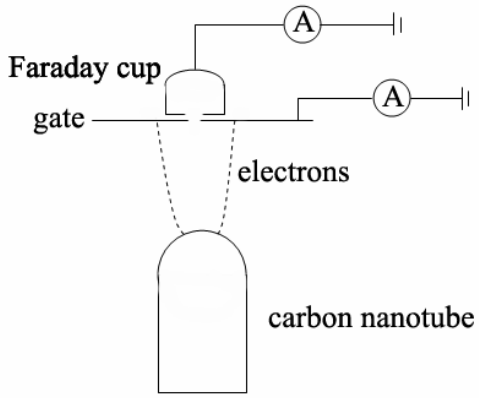

Fig. 4.7.1 Apparatus for measurement of angular current density.

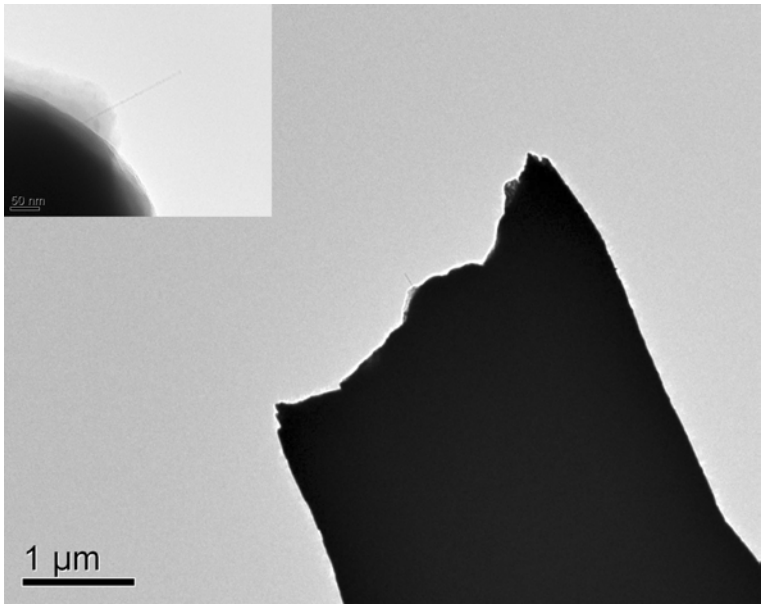

Fig. 4.7.2 Low magnification TEM image of a single carbon nanotube extruding from a carbon fiber. Inset image is high magnification TEM image from which the diameter of the nanotube is measured (~ 5 nm).

The measurements of angular current density were carried out in an apparatus shown schematically in Fig. 4.7.1. A carbon nanotube was carefully positioned 2 cm away from an anode. A phosphor screen with 1 mm or 2 mm diameter aperture serves as the gate and a Faraday cup was used to collect the electrons traveling through the aperture. The angular current density can be expressed as:

$$I_r = \frac{dI}{d\Omega} = \frac{I}{2\pi\{1-\cos[\tan^{-1}(r_{ape}/d)]\}}, \tag{4.7.3}$$

where r_{ape} is the radius of the aperture and d is the inter-electrode distance.

For the single carbon nanotube shown in Fig. 4.7.2, a total emission current of 3.2 μA and the Faraday cup (2mm aperture) current of 90 nA were obtained at 2400 V. Under this condition, the calculated angular current density was 1.1×10^{-5} ASr^{-1}. For carbon nanotubes, the optimal operating current is around 1 μA at 1700 V. At this optimum condition, the Faraday cup current is 30 nA and the calculated angular current density is 3.8×10^{-6} ASr^{-1}. From the TEM image, the estimated diameter of the nanotube is about 5 nm. Therefore the maximum reduced brightness and optimal condition reduced brightness were 2.4×10^{8} $ASr^{-1}m^{-2}V^{-1}$ and 1.1×10^{8} $ASr^{-1}m^{-2}V^{-1}$, respectively. The reduced brightness measured from two CNTs is listed in Table 4.7.1.

As shown in Fig. 4.7.3, there is a linear relationship between the Faraday cup current and the total current. The Faraday cup current can be expressed as:

$$I_{cup} = 0.013 I_{total}. \tag{4.7.4}$$

The slope of the linear fit is directly related to the alignment between the carbon nanotube and the aperture. In this case, the nanotube is not exactly aligned with the aperture and we expect that a higher slope should be achieved.

Table 4.7.1 The optimal reduced brightness B_{rOPT} and maximum brightness B_{rMAX} of CNT No. 5, 6 determined from the optimal total current (~ 1 μA)and maximum total current (2 – 3 μA).

CNT No.	$r_v \sim r$ (nm)	optimal I_r (ASr^{-1})	Br_{MAX} ($ASr^{-1}m^{-2}V^{-1}$)	Br_{OPT} ($ASr^{-1}m^{-2}V^{-1}$)
5	~ 2.5	3.8×10^{-6}	2.4×10^{8}	1.1×10^{8}
6	~ 2.8	1×10^{-5}	N/A	2.9×10^{8}

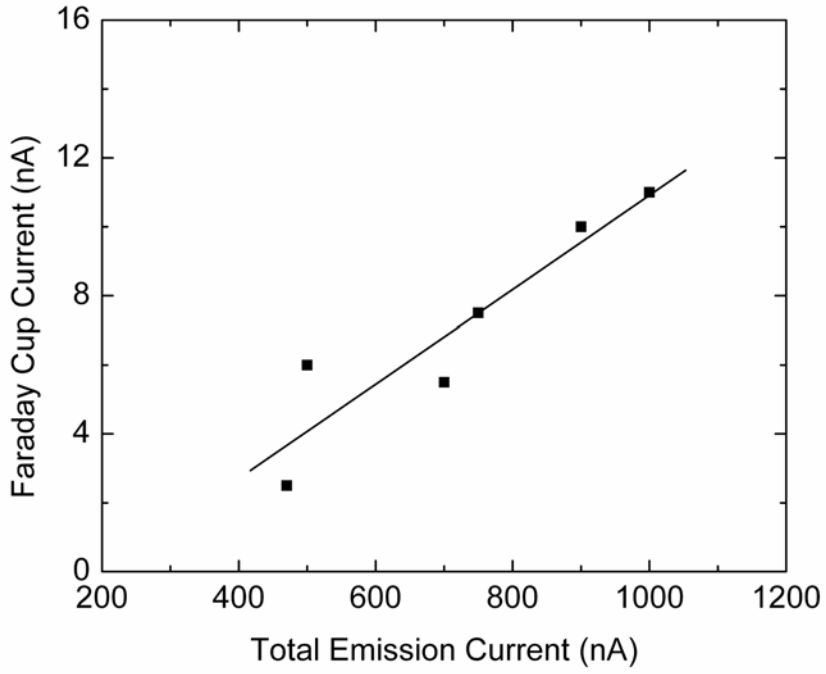

Fig. 4.7.3 Faraday cup current at the corresponding total emission current and a linear fit.

4.8 In-situ TEM Field Emission Measurement from a Single CNT

In order to make the fiber-CNT structure a good field emitter, the fiber should be a good conductor and the fiber-support contact should also be good. The resistance measurements of a single fiber were carried out in a TEM (JEM-2010F) operated at 120 kV under the vacuum of 10^{-7} Torr. The fiber-CNT structure was attached to a 0.35 mm gold wire, which is fixed to the frame of the holder, to serve as the cathode. Another electro-chemically etched gold tip was used as anode. The gold tip was mounted onto a 3D piezo-driven stage of an in-situ probing holder (from Nanofactory Instrument AB). The gold tip was carefully approached to the other end of the CNT until they were in contact. The current was measured as a function of voltage. The I-V curve displays a linear behavior (Fig. 4.8.1). The resistance of the carbon fiber was measured to be 77 $k\Omega$. This resistance is two orders of magnitude lower than that of MWNT. This result also suggests that the fiber-support contact is good.

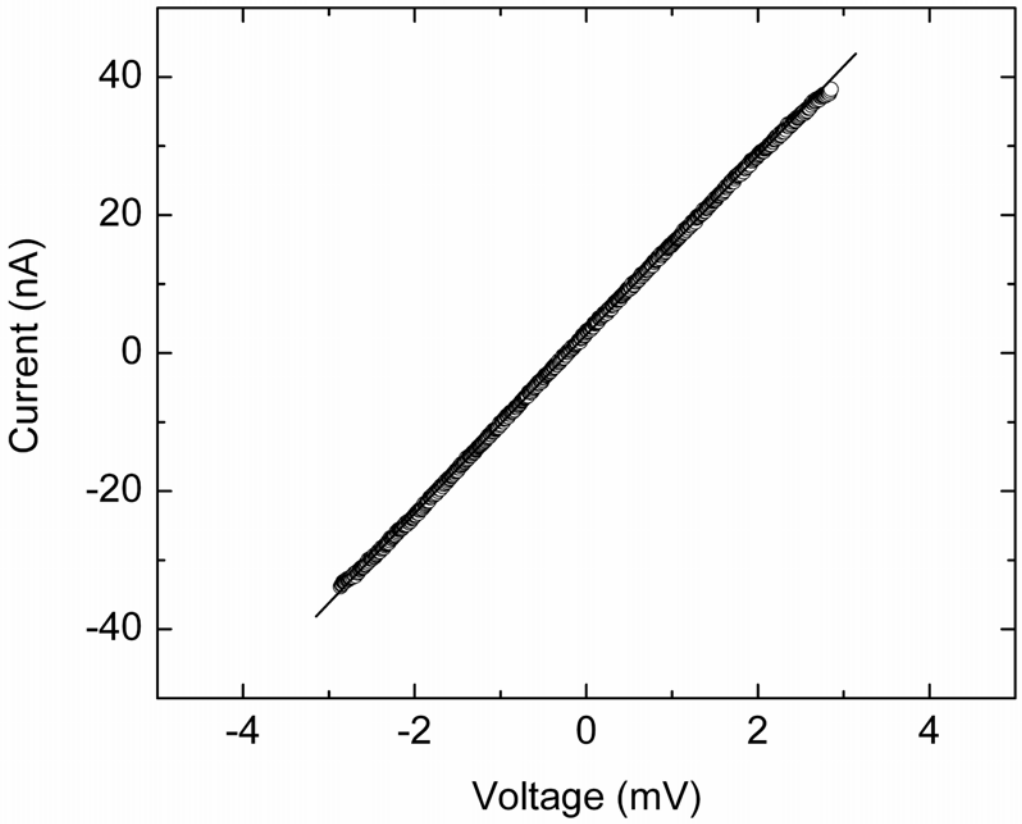

Fig. 4.8.1. Characteristic I-V behavior of a carbon fiber.

In-situ TEM field emission experiment can also help us to understand the failure mechanism. The in-situ field emission measurements were carried out on a single CNT shown in Fig. 4.8.2. The carbon nanotube is 3 nm in diameter and 1.5 μm in length. In the field emission process, it was observed that the CNT is bent by the electrostatic forces. The tilt angle of the nanotube was found to be 4.7º. Then the lateral bending amplitude is $l\theta = 0.12$ μm. The lateral bending force could be calculated by the Hooke's law [41]

$$P = ky \tag{4.8.1}$$

with

$$k = \frac{3\pi r^4 Y}{4l^3}, \tag{4.8.2}$$

where r is the nanotube radius, l is the nanotube length and Y is its Young's Modulus. Assuming the CNT has a Young's modulus 2 TPa [42], the bending force was calculated to be 8.5×10^{-13} N. If the CNT is not well-aligned, the electrostatic force can break the CNT.

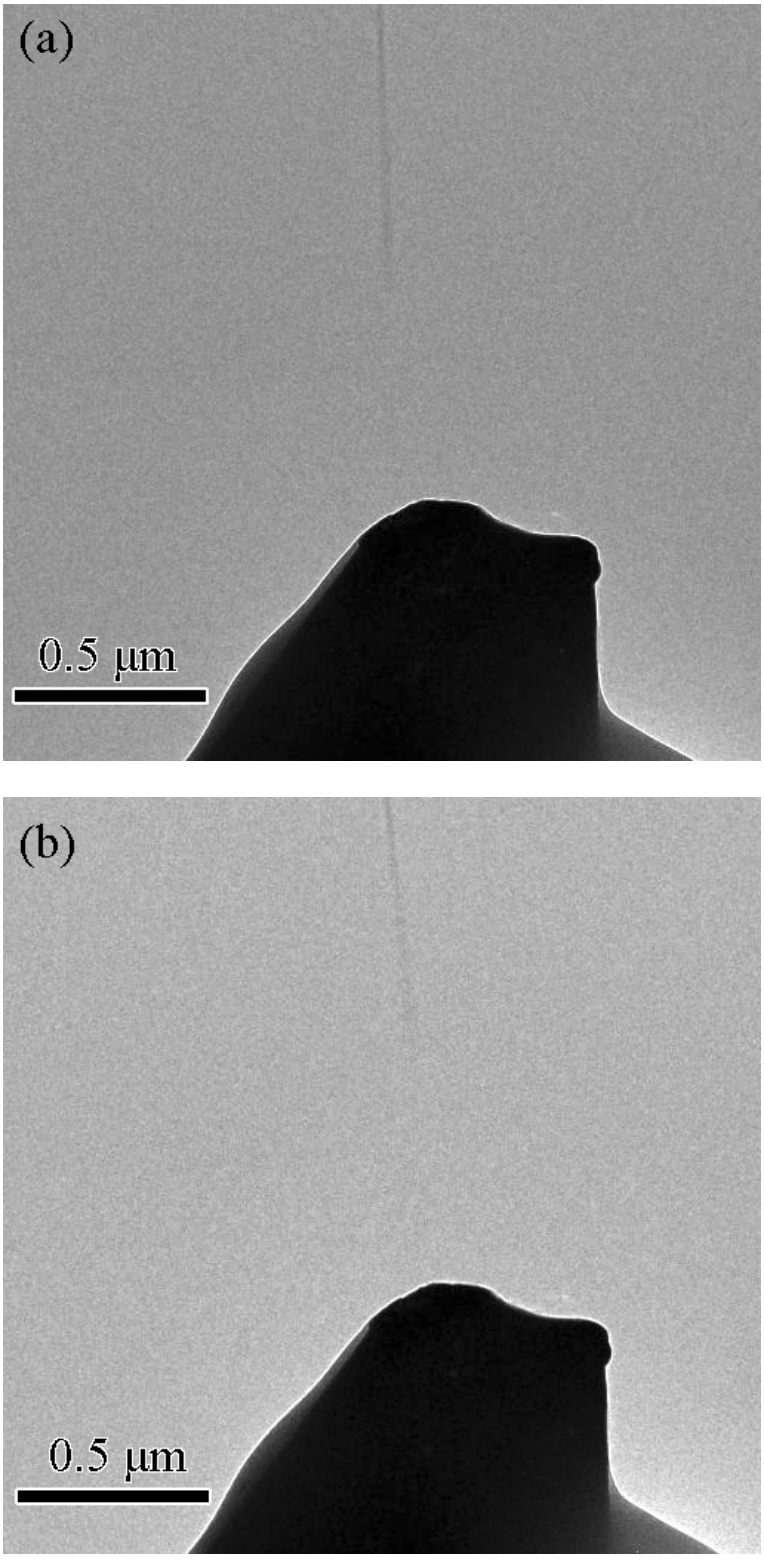

Fig. 4.8.2 (a) TEM image of a CNT extruding from a carbon fiber. (b) The corresponding CNT was bent 4.7º by the electric field during the field emission process.

4.9 References

[1] L. A. Chernozatonskii, Y. V. Gulyaez, Z. Y. Kosakovskaya, I. N. Sinitsyn, G. V. Torgashov, Yu. F. Zakharchenko, E. A. Fedorov, and V. P. Val'chuk, *Chem. Phys. Lett.* **75**, 3129 (1995).

[2] W. A. de Heer, A. Chatelain, and D. Ugarte, *Science* **270**, 1179 (1995).

[3] A. G. Rinzler, J. H. Hafner, P. Nikolaev, L. Lou, S. G. Kim, D. Tomanek, P. Nordlander, D. T. Colbert, and R. E. Smalley, *Science* **269**, 1550 (1995).

[4] T. Paulmier, M. Balat-Pichelin, D. Le Queau, R. Berjoan, and J. F. Robert, *Appl. Surf. Sci.* **180**, 227 (2001).

[5] O. Groening, O. M. Kuettel, C. Emmenegger, P. Groening, and L. Schlapbach, *Appl. Phys. Lett.* **69**, 476 (1996).

[6] M. J. Fransen, T. L. van Rooy, and P. Kruit, *Appl. Surf. Sci.* **146**, 312 (1999).

[7] N. de Jonge and N. J. van Druten, *Ultramicroscopy* **95**, 85 (2003).

[8] K. A. Dean and B. R. Chalamala, *Appl. Phys. Lett.* **75**, 3071 (1999).

[9] N. de Jonge and J. M. Bonard, *Phil. Trans. R. Soc. Lond. A* **362,** 2239 (2004).

[10] N. de Jonge, M. Allioux, J. T. Oostveen, K. B. K. Teo, and W. I. Milne, *Phys. Rev. Lett.* **94,** 186807 (2005).

[11] N. de Jonge, *J. Appl. Phys.* **95**, 673 (2004).

[12] N. de Jonge, Y. Lamy, K. Schoots, and T. H. Oosterkamp, *Nature* **420**, 393 (2002).

[13] R. H. Fowler and L. W. Nordheim, *Proc. Roy. Soc. Lond. A* **119**, 173 (1928).

[14] R. D. Young, *Phys. Rev.* **113**, 110 (1959).

[15] C. A. Spindt, I. Brodie, L. Humphrey, and E. R. Westerberg, *J. Appl. Phys.* **47**, 5248 (1976).

[16] N. de Jonge, Y. Lam, and M. Kaiser, *Nano Lett.* **3**, 1621 (2003).

[17] H. Nishijima, S. Akita, and Y. Nakayama, *Jpn. J. Appl. Phys.* **38**, 7247 (1999).

[18] Y. Nakayama, H. Nishijima, S. Akita, K. I. Hohmura, S. H. Yoshimura, and K. Takeyasu, *J. Vac. Sci. Technol. B* **18**, 661 (2000).

[19] J. H. Hafner, C. L. Cheung, T. H. Oosterkamp, and C. M. Lieber, *J. Phys. Chem. B* **106**, 743 (2001).

[20] Y. Wei, C. Xie, K. A. Dean, and B. F. Coll, *Appl. Phys. Lett.* **79**, 4527 (2001).

[21] R. V. Latham, *High Voltage Vacuum Insulation: The Physical Basis* (Academic, London, 1981).

[22] R. G. Forbes, C. J. Edgcombe, and U. Valdre, *Ultramicroscopy* **95**, 57 (2003).

[23] H. Schmid and H. W. Fink, *Appl. Phys. Lett.* **70**, 2679 (1997).

[24] D. B. Williams and C. B. Carter, *Transmission Electron Microscopy-A Textbook for Materials Science* (Plenum Press, New York, 1996), p. 72.

[25] J. M. Bonard, J. P. Salvetat, T. Stöckli, L. Forró, and Châtelain, *Appl. Phys. A* **69**, 245 (1999).

[26] O. Gröning, O. M. Küttel, Ch. Emmenegger, P. Gröning, and L. Schlapbach, *J. Vac. Sci. Technol. B* **18,** 665 (2000).

[27] R. Gao, Z. Pan, and Z. L. Wang, *Appl. Phys. Lett*. **78**, 1757 (2001).

[28] N. de Jonge, M. Allioux, M. Doytcheva, and M. Kaiser, *Appl. Phys. Lett.* **85,** 1607 (2004).

[29] Z. Xu, X. D. Dai, E. G. Wang, and Z. L. Wang, *Appl. Phys. Lett.* **87**, 163106 (2005).

[30] R. Gomer, *Field Emission and Field Ionization* (Harvard University Press, Cambridge, 1961), p. 32.

[31] G. C. Kokkorakis, J. A. Roumeliotis, and J. P. Xanthakis, *J. Appl. Phys.* **95**, 1468 (2004).

[32] J. Y. Huang, K. Kempa, S. H. Jo, S. Chen, and Z. F. Ren, *Appl. Phys. Lett.* **87**, 053110 (2005).

[33] J. M. Bonard, K. A. Dean, B. F. Coll, and C. Klinke, *Phys. Rev. Lett.* **89**, 1976021 (2002).

[34] R. H. Good, Jr., and E. W. Müller, *Handbuch der Physik* (Springer-Verlag, Berlin, 1956) Vol. **21**, p. 176.

[35] Y. Saito, K. Hamaguchi, K. Hata, K. Uchida, Y. Tasaka, F. Ikazaki, M. Yumura, A. Kasuya, and Y. Nishina, *Nature* **389**, 554 (1997).

[36] K. Hata, A. Takakura, and Y. Satio, *Surf. Sci.* **490**, 296 (2001).

[37] S. T. Purcell, P. Vincent, C. Journet, and V. T. Binh, *Phys. Rev. Lett.* **88**, 105502 (2002).

[38] P. W. Hawkes and E. Kasper, *Principles of Electron Optics II: Applied Geometrical Optics* (Academic Press, London, 1996).

[39] J. F. Hainfeld, *Scan. Electron Microsc.* **1**, 591 (1977).

[40] J. C. H. Spence, W. Qian, and M. P. Silverman, *J. Vac. Sci. Technol. A* **12**, 542 (1994).

[41] E. W. Wang, P. E. Sheehan, and C. M. Lieber, *Science* **277,** 1971 (1997).

[42] M. M. J. Treacy, T. W. Ebbesen, and J. M. Gibson, *Nature* **381** 678 (1996).

Chapter 5. Thermal Field Emission in Transition Zone from a Single Carbon Nanotube

5.1 Introduction

Thermal field emission has been widely studied in the past few decades [1-5]. A comprehensive review has been given in Chapter 2. But there are still some areas between the intermediate region and the field emission region that are not covered by any analytical equations [6]. To the author's best knowledge, the most reliable thermal field emission measurements of tungsten tips were done by Dyke and Dolan using an electronic pulse technique to reduce the surface migration. Since their discovery [7], carbon nanotubes have been proved to be a promising candidate for future field emission electron source applications [8-10]. Due to its sp^2 covalent bonds, a carbon nanotube can withstand high temperature up to more than 2000 K under high electric field up to 6×10^7 V/cm [11] and also the surface migration is minimized [12], which together make it a good material for studying the electron emission at both high field and high temperature. In this Chapter, we will study the thermal field emission properties of a single carbon nanotube. The emission theory in the transition zone between the thermionic emission and the field emission will be re-examined and compared with the experimental results.

5.2 WKB Approximation

The Wentzel-Kramers-Brillouin approximation or the WKB approximation was developed in 1926 [13,14,15]. The approximation was commonly used when the Schrödinger equation can not be reduced to one of the standard mathematical physics equations. For the Schrödinger wave equation

$$i\hbar\frac{\partial\psi}{\partial t} = -\frac{\hbar^2}{2m}\nabla^2\psi + V(r)\psi\,, \tag{5.2.1}$$

where $\hbar$ is Planck's constant divided by 2π, m is the mass of the particle and $V(r)$ is the potential energy of the particle. The solution ψ can be written as

$$\psi(r,t) = AExp[\frac{iW(r,t)}{\hbar}] \tag{5.2.2}$$

on the condition that *W(r,t)* satisfies

$$\frac{\partial W}{\partial t} + \frac{1}{2m}(\nabla W)^2 + V - \frac{i\hbar}{2m}\nabla^2 W = 0\,. \tag{5.2.3}$$

In the classical limit ($\hbar \to 0$), Eq. (5.2.3) is the same as the Hamilton equation in classical dynamics. Then *W(r,t)* can be written as:

$$W(r,t) = S(r) - Et\,. \tag{5.2.4}$$

Assuming the eigenfunction is $u(r)\exp[-iEt/\hbar]$, $u(r)$ can be obtained as

$$u(r) = A\exp[\frac{iS(r)}{\hbar}], \tag{5.2.5}$$

and *S(r)* must satisfy the following equation:

$$\frac{1}{2m}(\nabla S)^2 - [E - V(r)] - \frac{i\hbar}{2m}\nabla^2 S = 0\,. \tag{5.2.6}$$

The Schrödinger equation in one dimension now can be expressed in $u(r)$

$$\frac{d^2u(x)}{dx^2} + k^2(x)u = 0\,, \qquad k^2 > 0 \tag{5.2.7}$$

$$\frac{d^2u(x)}{dx^2} - K^2(x)u = 0\,, \qquad K^2 > 0 \tag{5.2.8}$$

where k and K are both positive and can be expressed as

$$k(x) = \frac{1}{\hbar}\{2m[E - V(x)]\}^{\frac{1}{2}} \text{ when } V(x) < E\,, \tag{5.2.9}$$

$$K(x) = \frac{1}{\hbar}\{2m[V(x) - E]\}^{\frac{1}{2}} \text{ when } V(x) > E\,. \tag{5.2.10}$$

If Eq. (5.2.5) is plugged into Eq. (5.2.7), Eq. (5.2.7) becomes

$$i\hbar S'' - S'^2 + \hbar^2 k^2 = 0\,. \tag{5.2.11}$$

Expanding S in the power of $\hbar$

$$S = S_0 + S_1\hbar + S_2\hbar^2 + S_3\hbar^3\,, \tag{5.2.12}$$

and plugging it into Eq. (5.2.10), the following series of equations can be obtained

$$\begin{aligned} &-S_0'^2 + 2m(E - V) = 0, \\ &iS_0'' - 2S_0'S_1' = 0. \end{aligned} \tag{5.2.13}$$

S_0, S_1,….. can be obtained by solving Eq. (5.2.13)

$$S_0(x) = \pm\hbar\int^x k(x')dx'\,,\ S_1(x) = \frac{1}{2}i\ln[k(x)]\,, \tag{5.2.14}$$

where x_1 and x_2 are the turning points ($k = 0$). Then the solution to the Schrödinger wave equation can be approximately obtained as:

$$u(x) = Ak^{-\frac{1}{2}}\exp[\pm i\int^x kdx]\,,\ V(x) < E \tag{5.2.15}$$

or

$$u(x) = BK^{-\frac{1}{2}} \exp[\pm\int^{x} K dx],\ V(x) > E\ . \tag{5.2.16}$$

By this approximation, the transmission function for a particle of energy W traversing a potential barrier from x_1 to x_2 is given as [16]

$$D(F,W) = \exp[-2\int_{x_1}^{x_2} |k(x)| dx]\ . \tag{5.2.17}$$

Although the WKB approximation can be very useful in solving Schrödinger equation, it is only valid when a certain criterion is met. In order to get the solution $u(x)$ (Eq. (5.2.15), the second term in Eq. (5.2.12) must be far smaller compared to the first term. The ratio $\hbar S_1/S_0$ is small if $\hbar S_1^{'}/S_0^{'}$ is small. Thus this approximation can be expected to be valid over the range of x where

$$\left|\frac{\hbar S_1^{'}}{S_0^{'}}\right| = \left|\frac{k^{'}}{2k^2}\right| << 1\ . \tag{5.2.18}$$

Since the de Broglie wavelength is $2\pi/k$, then Eq. (5.2.18) can be rewritten as:

$$\frac{\lambda}{4\pi}\left|\frac{dk}{dx}\right| << k\ . \tag{5.2.19}$$

This condition suggests that the fractional momentum change over $\lambda/4\pi$ is far less than unity. Therefore the condition for the WKB approximation to be valid is that the momentum should be nearly constant over many wavelengths.

Although the WKB approximation is a convenient method to obtain the transmission function, it has some limitations. Firstly, at the turning point where $k = 0$, the WKB approximation violates the assumption that the momentum should be nearly constant over many wavelengths. This can be solved using a connection equation when the turning point region is small compared to the whole length of the barrier. The second limitation is that, when the kinetic energies of electrons are near the top of the barrier, the two turning points

are very close, in which case the connection equation will not work. In this case, the transmission function is not valid either. Also when the kinetic energies of electrons are higher than the top of the barrier, the transmission function should equal to unity and WKB approximation breaks down.

The WKB transmission function is quite accurate within ± 0.5 eV of the Fermi level [16]. When the energy of electrons is near the top of the barrier, the WKB approximation is not accurate enough. Miller and Good have developed a parabolic WKB-type approximation to solve this problem [17,18]. The transmission function produced by this approximation is

$$D(F,W) = \{1 + \exp[-2i\hbar^{-1}\int_{x_1}^{x_2} p(x)dx]\}^{-1}, \tag{5.2.20}$$

where x_1 and x_2 are points where $p^2(x) = 0$. Eq. (5.2.20) only works when $W < W_l$ [19], where

$$W_l = -\frac{\sqrt{2}}{2}(e^3F)^{1/2}. \tag{5.2.21}$$

The transmission function can be treated as unity if $W > W_l$. The integral is

$$-2i\hbar^{-1}\int_{x_1}^{x_2} p(x)dx = -2i\hbar^{-1}\int_{x_1}^{x_2} \{2m[W + \frac{e^2}{4x} + eFx]\}^{1/2} dx. \tag{5.2.22}$$

If we define

$$y = (e^3F)^{1/2}/|W|, \tag{5.2.23}$$

then Eq. (5.2.22) can be solved as

$$
\begin{aligned}
-2i\hbar^{-1}\int_{x_1}^{x_2} p(x)dx &= -2i\hbar^{-1}\int_{x_1}^{x_2}\{2m[W+\frac{e^2}{4x}+eFx]\}^{1/2}dx \\
&= -2i\hbar^{-1}(2m)^{1/2}\int_{1-(1-y^2)^{1/2}}^{1+(1-y^2)^{1/2}}[\frac{(e^3F)^{1/2}}{-y}+\frac{e^2}{4x}+eFx]^{1/2}dx \\
&= -\sqrt{2}i\hbar(2m)^{1/2}(e^3F)^{1/4}y^{-1/2}\int_{1-(1-y^2)^{1/2}}^{1+(1-y^2)^{1/2}}[-2+\frac{y^2}{2yF^{1/2}e^{-1/2}x}+2yF^{1/2}e^{-1/2}x]^{1/2}dx \\
&= (4/3)\sqrt{2}\left(\frac{F\hbar^4}{m^2e^5}\right)^{-1/4}y^{-3/2}v(y)
\end{aligned}
\tag{5.2.24}
$$

where

$$
v(y) = -\frac{3i}{4\sqrt{2}}\int_{1-(1-y^2)^{1/2}}^{1+(1-y^2)^{1/2}}[-2+\frac{y^2}{\rho}+\rho]d\rho\,, \tag{5.2.25}
$$

and

$$
\rho = 2yF^{1/2}e^{-1/2}x\,. \tag{5.2.26}
$$

The transmission function is

$$
D(F,W) = \{1+\exp[(\frac{4\sqrt{2}}{3}\left(\frac{F\hbar^4}{m^2e^5}\right)^{-1/4}y^{-3/2}v(y)]\}^{-1},\ \text{if } W<W_l \tag{5.2.27}
$$

and

$$
D(F,W) = 1,\ \text{if } W>W_l\,. \tag{5.2.28}
$$

The current density is

$$
\begin{aligned}
J(F,T,\zeta) &= e\int_{-\infty}^{\infty} D(F,W)N(T,\zeta,W)dW \\
&= \frac{4\pi mkTe}{h^3}\int_{-\infty}^{W_l}\frac{\ln\{1+\exp[-(W-\zeta)/kT]\}}{1+\exp[\frac{4\sqrt{2}}{3}\left(\frac{F\hbar^4}{m^2e^5}\right)^{-1/4}y^{-3/2}v(y)]}dW \\
&+ \frac{4\pi mkTe}{h^3}\int_{W_l}^{\infty}\ln\{1+\exp[-(W-\zeta)/kT]\}dW,
\end{aligned}
\tag{5.2.29}
$$

where

$$N(T,\zeta,W)=\frac{4\pi mkT}{h^3}\int_{W_l}^{\infty}\ln\{1+\exp[-(W-\zeta)/kT]\}dW \tag{5.2.30}$$

is the electron supply function and ζ is the Fermi energy. A more detailed discussion can be found in reference 19.

5.3 Thermal Field Emission in the Transition Zone

The general current density is [19]

$$\begin{aligned}J(F,T,\zeta)=&\frac{kT}{2\pi^2}\int_{-\infty}^{W_l}\frac{\ln\{1+\exp[-(W-\zeta)/kT]\}}{1+\exp[\frac{4}{3}\sqrt{2}F^{-\frac{1}{4}}y^{-\frac{3}{2}}v(y)]}dW\\&+\frac{kT}{2\pi^2}\int_{W_l}^{\infty}\ln\{\{1+\exp[-(W-\zeta)/kT]\}dW.\end{aligned} \tag{5.3.1}$$

In Eq. (5.3.1) the Hartree units are used. That is, J is redefined to mean the current density divided by $m^3e^9\hbar^{-7}$ = 2.37×10^{14} A/cm^2; F to mean the electric field divided by $m^2e^5\hbar^{-4}$ = 5.15×10^9 V/m; and ζ, kT, W, W_a, W_l to mean the corresponding energies divided by $me^4\hbar^{-2}$ = 27.2 eV. Under a moderate field and high temperature condition, the second term can be discarded and leads to:

$$J(F,T,\zeta)=\frac{kT}{2\pi^2}\int_{-\infty}^{W_l}\frac{\ln\{1+\exp[-(W-\zeta)/kT]\}}{1+\exp[\frac{4}{3}\sqrt{2}F^{-\frac{1}{4}}y^{-\frac{3}{2}}v(y)]}dW \tag{5.3.2}$$

Applying the approximation

$$\{1+\exp[\frac{4}{3}\sqrt{2}F^{-\frac{1}{4}}y^{-\frac{3}{2}}v(y)]\}^{-1}=\exp[-\frac{4}{3}\sqrt{2}F^{-\frac{1}{4}}y^{-\frac{3}{2}}v(y)], \tag{5.3.3}$$

the general current density function becomes

$$J(F,T,\zeta)=\frac{kT}{2\pi^2}\int_{-\infty}^{W_t}\ln\{1+\exp[-(W-\zeta)/kT]\}\exp[-\frac{4}{3}\sqrt{2}F^{-\frac{1}{4}}y^{-\frac{3}{2}}v(y)]dW \qquad (5.3.4)$$

In order to analytically evaluate this integral, another approximation needs to be adopted.

$$\ln\{1+\exp[-(W-\zeta)/kT]\}=0.7\exp[-0.8(W-\zeta)/kT] \qquad (5.3.5)$$

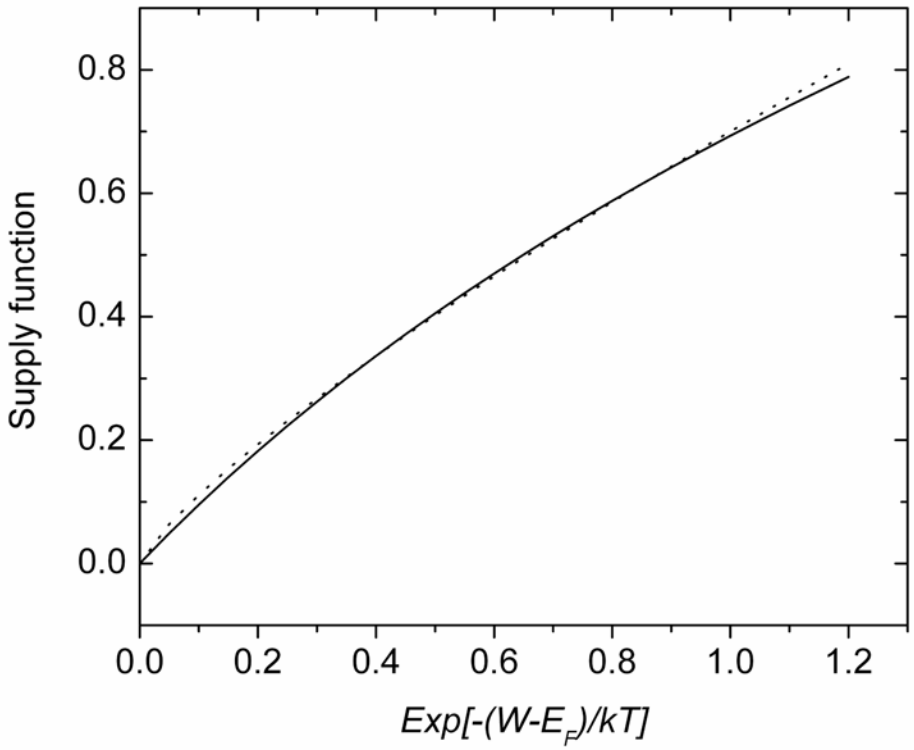

Fig. 5.3.1 The exact values of supply function (left-side of Eq. (5.3.5), solid line) and approximated value of supply function (right-side of Eq. (5.3.5), dot line). The maximum error generated by this approximation is less than 1% between $\exp[-(W-\zeta)/kT]=0.35$ and $\exp[-(W-\zeta)/kT]=1$.

The exact values of the two functions have been plotted in Fig. 5.3.1. Between $\exp[-(W-\zeta)/kT]=0.35$ and $\exp[-(W-\zeta)/kT]=1$, the maximum error introduced by this approximation is less than 1%. After plugging Eq. (5.3.5) into Eq. (5.3.4), the current density can be described as:

$$J(F,T,\zeta)=0.7\frac{kT}{2\pi^2}\int_{-\infty}^{W_l}\exp[-0.8\frac{W-\zeta}{kT}-\frac{4}{3}\sqrt{2}F^{-\frac{1}{4}}y^{-\frac{3}{2}}v(y)]dW\,. \tag{5.3.6}$$

The reason we adopt this approximation is that the current density integral can be conveniently evaluated using the saddle point method.

First, $-0.8\frac{W-\zeta}{kT}-\frac{\sqrt{2}v(y)}{3F^{1/4}y^{3/2}}$ has only one maximum and it can be expanded as

$$-0.8\frac{W-\zeta}{kT}-\frac{\sqrt{2}v(y)}{3F^{1/4}y^{3/2}}=-b+d(W-\eta)^2, \tag{5.3.7}$$

with

$$\eta=-\frac{0.08F^2}{(kT)^2t^2(F^{1/2}/-\eta)}, \tag{5.3.8}$$

$$b=0.8\frac{\eta-\zeta}{kT}-\frac{4\sqrt{2}(-\eta)^{3/2}v(F^{1/2}/-\eta)}{3F}, \tag{5.3.9}$$

and

$$d=\frac{\sqrt{2}(-\eta)^{3/2}v(F^{1/2}/-\eta)}{2F(\eta^2-F)} \tag{5.3.10}$$

where η is the energy at which Eq.(5.3.7) has its maximum value. Since the majority of this integral is limited in a finite range, the upper limit W_l can be extended to infinity. Then the current density can be obtained as:

$$J(F,T,\zeta) = 0.7\frac{kT}{2\pi^2}\int_{-\infty}^{\infty} Exp[-0.8\frac{W-\zeta}{kT} - \frac{4}{3}\sqrt{2}F^{-\frac{1}{4}}y^{-\frac{3}{2}}v(y)]dW$$
$$= \frac{0.7kT}{2\pi^2}(\frac{\pi}{d})^{1/2} Exp[-b], \tag{5.3.11}$$

where the following relationship has been used

$$\int_{-\infty}^{\infty} \exp[-dx^2]dx = (\frac{\pi}{d})^{1/2} . \tag{5.3.12}$$

Using Eq. (5.3.9) and Eq. (5.3.10), the current density is

$$J(F,T,\zeta) = \frac{0.7F}{2\pi}(\frac{kTt}{2\pi})^{\frac{1}{2}} \exp[-\frac{0.8\phi}{kT} + \frac{0.064\Theta(y)F^2}{3(kT)^3}], \tag{5.3.13}$$

where

$$3t(y) = 4s(y) - v(y), \tag{5.3.14}$$

and

$$\Theta = 3t^{-2} - 2vt^{-3}, \tag{5.3.15}$$

and the arguments of *v(y)* and *t(y)* are $y = F^{1/2}/\eta$. The exact values of functions *v(y)*, *s(y)*, *t(y)*, and *Θ(y)* are given in Appendix A. Eq. (5.3.13) is written in the Hartree unit and can be converted into

$$J(F,T,\zeta) = 3.64[Tt(y)]^{\frac{1}{2}} \exp[-\frac{0.8\phi}{8.62\times10^{-5}T} + 2.53\times10^{-5}\frac{0.064\Theta(y)F^2}{T^3}] \text{ Acm}^{-2} \tag{3.16}$$

for *F* in V/cm, ϕ in eV, and *T* in Kelvin.

Due to the complexity of function *Θ(y)*, the relationship between the current density, field, temperature and work function is not straightforward. By a numerical method, we can obtain

$$\Theta(y) \cong 0.96 + 1.485y^{\frac{4}{3}} . \tag{5.3.17}$$

Using this approximation, Eq. (5.3.16) can be rewritten as

$$J = 3.64[Tt(y)]^{1/2} F \exp[-\frac{0.8\phi}{8.62\times10^{-5}T} + \frac{62.6}{T^{1/3}} + 2.43\times10^{-5}\frac{F^2}{T^3}] \text{ Acm}^{-2} \qquad (5.3.18)$$

for F in V/cm, ϕ in eV, and T in Kelvin. If we divide both side of Eq. (5.3.18) by F, and apply natural logarithm, the equation becomes

$$\ln\left(\frac{J}{F}\right) = 2.43\times10^{-5}\frac{F^2}{T^3} + \frac{62.6}{T^{1/3}} - \frac{0.8\phi}{8.62\times10^{-5}T} + \ln\{3.64[Tt(y)]^{1/2}\}. \qquad (5.3.19)$$

Since *t(y)* is a slow varying function, a plot of *Ln(J/F) vs.* F^2 will generate a straight line. Practically, we can rewrite Eq (5.3.19) in terms of the current I and the extraction voltage V,

$$\ln\left(\frac{I}{V}\right) = 2.43\times10^{-5}\frac{\beta^2}{T^3}V^2 + \frac{62.6}{T^{1/3}} - \frac{0.8\phi}{8.62\times10^{-5}T} + \ln\{3.64A\beta[Tt(y)]^{1/2}\} \qquad (5.3.20)$$

A *Ln(I/V) vs.* V^2 plot will generate a line with a slope of $2.45\times10^{-5}\beta^2/T^3$. If the field enhancement factor of the emitter is known, the temperature of the emitter can be calculated from the slope of the *Ln(I/V) vs.* V^2 plot.

5.4 Boundary Conditions

The boundary for Eq. (5.3.16) can be found by requiring that the majority of the integral of Eq. (5.3.4) falls in the range where the approximation (Eq.(5.3.3) and Eq. (5.3.5)) holds. Eq. (5.3.5) is fairly accurate over the range:

$$0.35 < Exp[-(W-\zeta)/kT] < 1.1 \qquad (5.4.1)$$

and it can also be used for greater W value. The condition on W so that Eq. (5.3.5) can be used is given by

$$W > \zeta. \qquad (5.4.2)$$

In the neighborhood of $W \geq \zeta$, the current density integrand roughly behaves like

$$\exp[-W(\frac{0.8}{kT}-c)], \tag{5.4.3}$$

where

$$c=\frac{2\sqrt{2}\phi^{\frac{1}{2}}t(F^{1/2}/-\eta)}{F}. \tag{5.4.4}$$

The condition for Eq. (5.3.3) is given by [19]

$$W<-F^{1/2}-\pi^{-1}F^{3/4}. \tag{5.4.5}$$

In the neighborhood of $-F^{1/2}-\pi^{-1}F^{3/4}$, the current density integrand roughly behaves like

$$\exp[-W(\frac{0.8}{kT}-\pi F^{-3/4})]. \tag{5.3.6}$$

The majority of the current density integral falls in the following range

$$(\frac{0.8}{kT}-c)^{-1}<W-\eta<(\frac{0.8}{kT}-\pi F^{-3/4})^{-1}. \tag{5.4.7}$$

Combining Eq. (5.4.2) and Eq. (5.4.5) with Eq. (5.4.7), the boundaries for Eq. (5.3.16) is then

$$-\frac{0.08F^2}{(kT)^2t^2}>-\phi+\frac{kT}{ckT-0.8}, \tag{5.4.8}$$

and

$$-\frac{0.08F^2}{(kT)^2t^2}<-F^{1/2}-\frac{F^{3/4}}{\pi}-\frac{1}{\frac{0.8}{kT}-\frac{\pi}{F^{3/4}}}. \tag{5.4.9}$$

Both Eq. (5.4.8) and Eq. (5.4.9) are plotted (with a 4.8 eV work function) and labeled as *E* and *F*, respectively, in Fig. 5.4.1(a). Eq. (5.3.16) is valid in the whole shaded area, which is here named extended intermediate region because of a similar approach was used to obtain the expression for the intermediate region. The importance of Eq. (5.3.16) is that it passes the boundary $F_2\cong 9.4\times10^3\phi^{1/2}T$ [6], where the T-F equation (Eq. (2.2.4)) totally breaks down (*p*

= 1) and connects the intermediate region with the field emission region. This equation also covers most of the part between $p = 0.7$ and $p = 1$, where the field emission theory is not accurate enough.

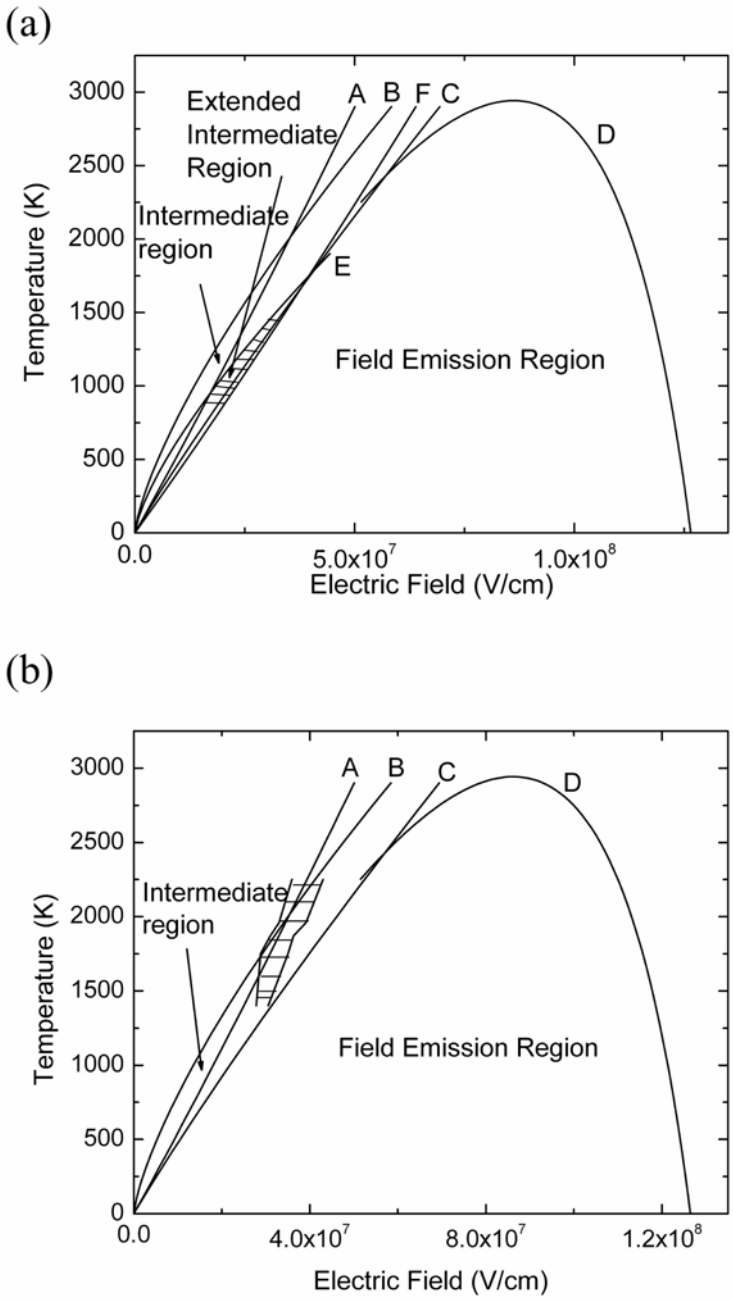

Fig. 5.4.1 (a) The boundaries of intermediate region (A, B) and field emission region (C, D) for a 4.8 eV work function calculated from Eq. (62), Eq. (69), Eq. (58), Eq. (57), respectively, given in reference 19 and the boundaries E and F for Eq. (5.3.16) are calculated from Eqs. (5.4.9) and (5.4.8), respectively. The shaded area is labeled as the extended intermediate region, in which Eq. (5.3.16) is valid. (b) Experimentally measured intermediate region is indicated by the shaded area.

5.5 Experimental

The detailed procedure to prepare a single nanotube field emitter has been given in Chapter 4. Instead of using a copper ribbon, we used a 0.1 mm diameter tungsten wire as a supporting structure. The TEM image of the emitter is shown in Fig. 5.5.1. The tungsten supporting wire with a fiber-CNT attached to the tip was point welded to a hair-pin tungsten heating filament. Then the whole structure was mounted into a field emission chamber in which a heating circuit was set up to heat the filament up to 2000 K. The apparatus is shown schematically in Fig. 5.5.2.

Before the measurement, the field emission chamber was vacuumed and baked for four days. After the vacuum level reached 10^{-8} Torr, the heating filament was slowly heated up. At the beginning, the vacuum became worse (~10^{-7} Torr) due to degassing and decomposition of the carbon glue which was used to assure the firm attachment of fiber-CNT structure. After an hour, the vacuum level dropped back to 10^{-8} Torr. The I-V curves of thermal field emission between 1200 K and 2200 K were measured. The stabilities of emission current at different temperatures were also studied.

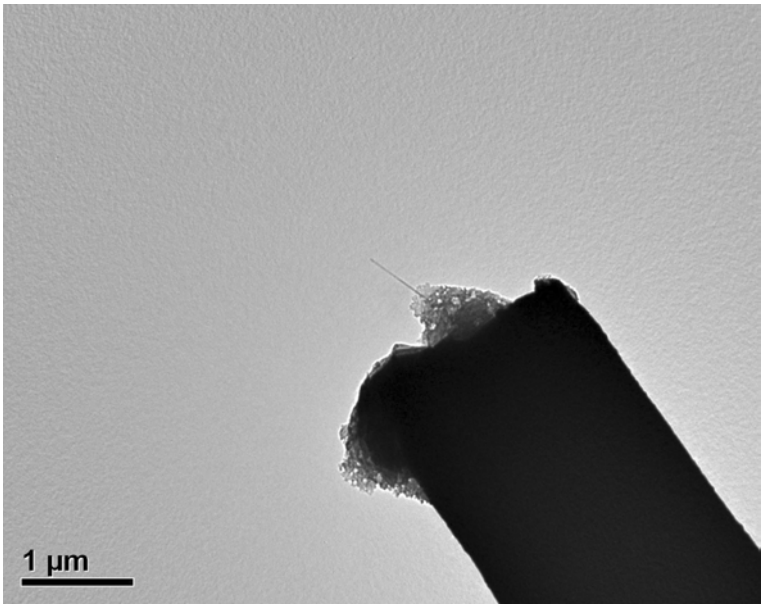

Fig. 5.5.1 Low magnification TEM image of an individual MWNT (with 8 nm diameter and 1.1 μm length) extruding from a carbon fiber.

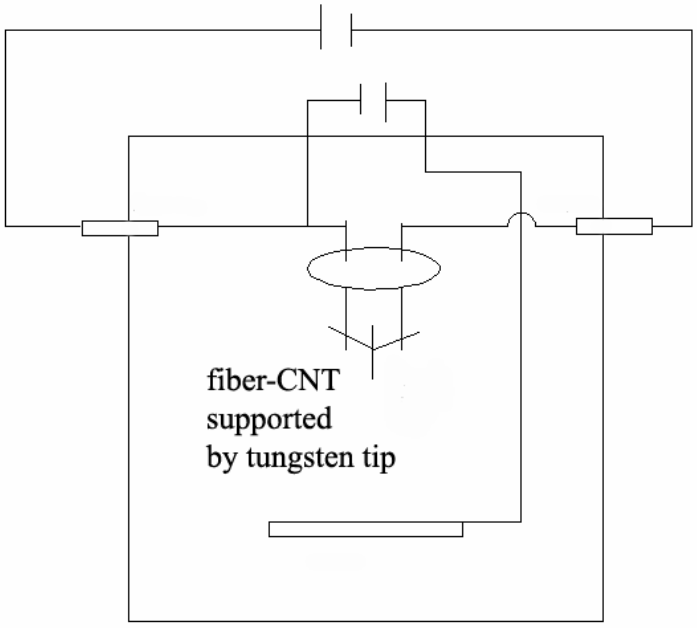

Fig. 5.5.2 Thermal field emission measurement apparatus.

5.6 Results and Discussion

In order to test Eq. (5.3.18), the field enhancement factor must first be found. Cold field emission measurements were carried out with a single carbon nanotube shown in Fig. 5.5.1 to determine the field enhancement factor β. The emission current was measured as a function of the extraction voltage at room temperature. The data follow a straight line in the F-N plot (Fig. 5.6.1). Since the slope of the F-N plot is $-6.44\times10^{7}\phi^{3/2}/\beta$ (Eq.(4.1.5)), the field enhancement factor is calculated to be 1.15×10^{7} m^{-1} with a 4.8 eV work function [20]. In a carbon nanotube, since the carbon atoms are covalently bonded to three other carbon atoms, the field enhancement factor does not change under high temperature. To prove this, field enhancement was measured to be 1.16×10^{7} m^{-1} after the nanotube cooled down to room temperature, which suggests that the field enhancement factor did not change in the process of thermal field emission measurement. Fig. 5.6.1 also shows that, before the thermal field emission and after the thermal field emission, the F-N plots have different y-intercepts which suggest that the emission area had changed. After thermal field emission measurement, the emission area

$$A=\frac{\phi}{1.5\times10^{-6}\beta^{2}}Exp[y_{\text{int}}-\frac{10.4}{\phi^{1/2}}]\ \text{cm}^2 \tag{5.6.1}$$

where ϕ is the work function in eV, β is the field enhancement factor in cm^{-1}, and y_{int} is the y-intercept of the F-N plot. It was found that the emission area was reduced from 1.4×10^{-14} m^2 to 3.1×10^{-16} m^2. At high temperature the adsorbed gas molecules and amorphous carbon could be removed and the CNT tip surface was annealed. This process reduced the emission area.

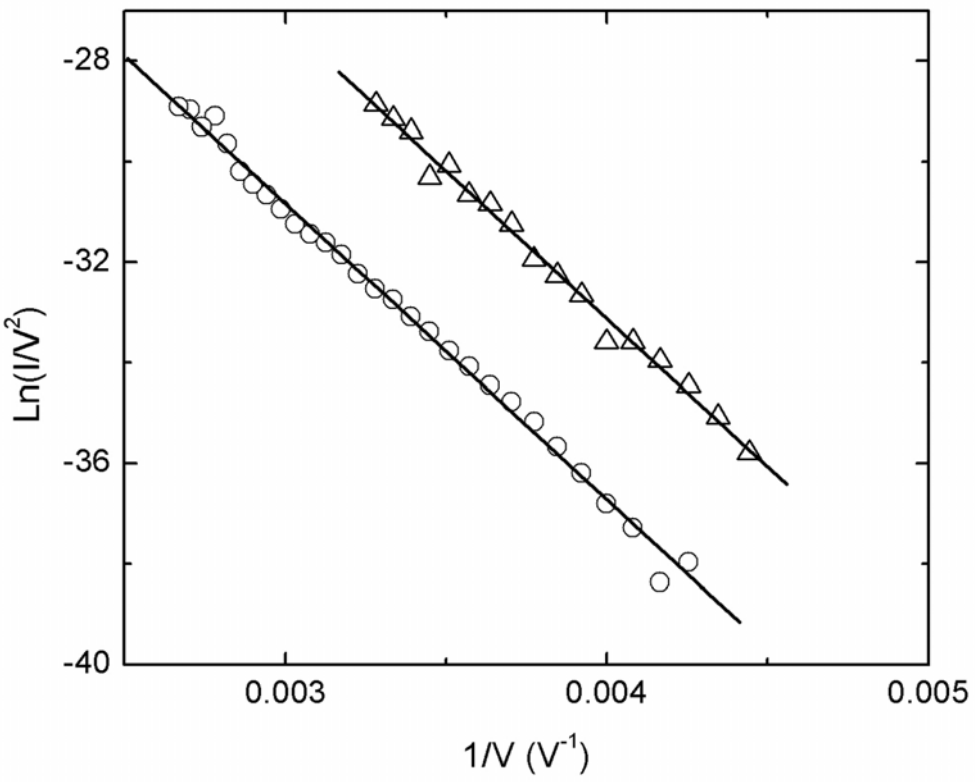

Fig. 5.6.1 Cold field emission measurement on an individual carbon nanotube at room temperature. Triangle is the F-N plot before thermal field emission measurement and a linear fit suggests that the field enhancement factor is 1.15×10^7 m^{-1}. Circle is the F-N plot after thermal field emission measurement and a linear fit of the Fowler-Nordheim theory suggests that the field enhancement factor is 1.16×10^7 m^{-1}.

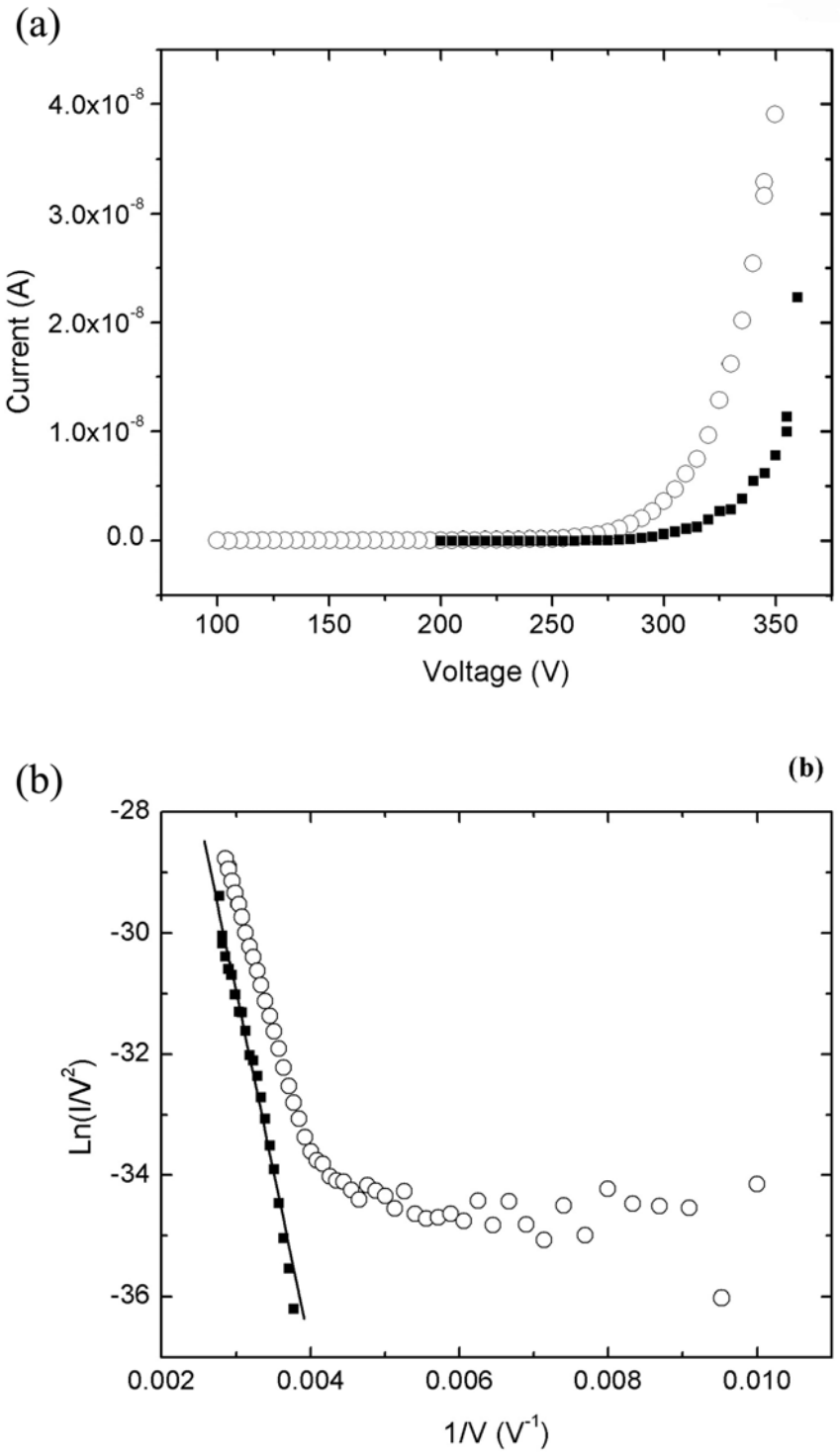

Fig. 5.6.2 (a) I-V curve of cold (solid squares) and thermal field emission (open circles) from an individual nanotube. (b) F-N plot and linear fitting for the cold field emission.

Thermal field emission measurements were also carried out on the same nanotube (Fig. 5.3.1). First the tungsten heating filament was heated to above 1000 K. After the temperature was stabilized, the emission current was measured as a function of the extraction voltage. The I-V curves and the corresponding F-N plots are shown in Fig. 5.6.2. It shows that, at low field less than 3.5×10^7 V/cm, the F-N plot of thermal field emission deviates dramatically from a straight line. But at high field above 4×10^7 V/cm, the thermal field emission behaves like field emission. In order to better understand the thermal field emission of a single nanotube, a *Ln(I/V) vs.* V^2 plot was made (Fig.5.6.3). Between 2.9×10^7 V/cm and 3.5×10^7 V/cm, the data follow a linear relationship which suggests that, in this region, the electron emission is governed by the Murphy-Good equation [19]:

$$J = \frac{F}{2\pi}\left(\frac{kTt(y)}{2\pi}\right)^{1/2}\exp\left[-\frac{\phi}{kT}+\frac{F^2\Theta(y)}{24(kT)^3}\right]. \tag{5.6.2}$$

The details of Eq. (2.2.11) can be found in Chapter 2. If the approximation (Eq. (5.3.17))

$$\Theta(y)\cong 0.96+1.485y^{\frac{4}{3}} \tag{5.6.3}$$

is plugged into Eq. (2.2.11), then a more straightforward equation in the intermediate region is obtained,

$$J = 5.2F(Tt)^{\frac{1}{2}}\exp\left(-\frac{\phi}{8.62\times10^{-5}T}+\frac{67.4}{T^{1/3}}+\frac{4.74\times10^{-5}F^2}{T^3}\right)\ \text{Acm}^{-2} \tag{5.6.4}$$

for F in V/cm, ϕ in eV, and T in K. Practically we can rewrite this equation as

$$I = 5.2\beta VA(Tt)^{\frac{1}{2}}\exp\left(-\frac{\phi}{8.62\times10^{-5}T}+\frac{67.4}{T^{1/3}}+\frac{4.74\times10^{-5}\beta^2}{T^3}V^2\right), \tag{5.6.5}$$

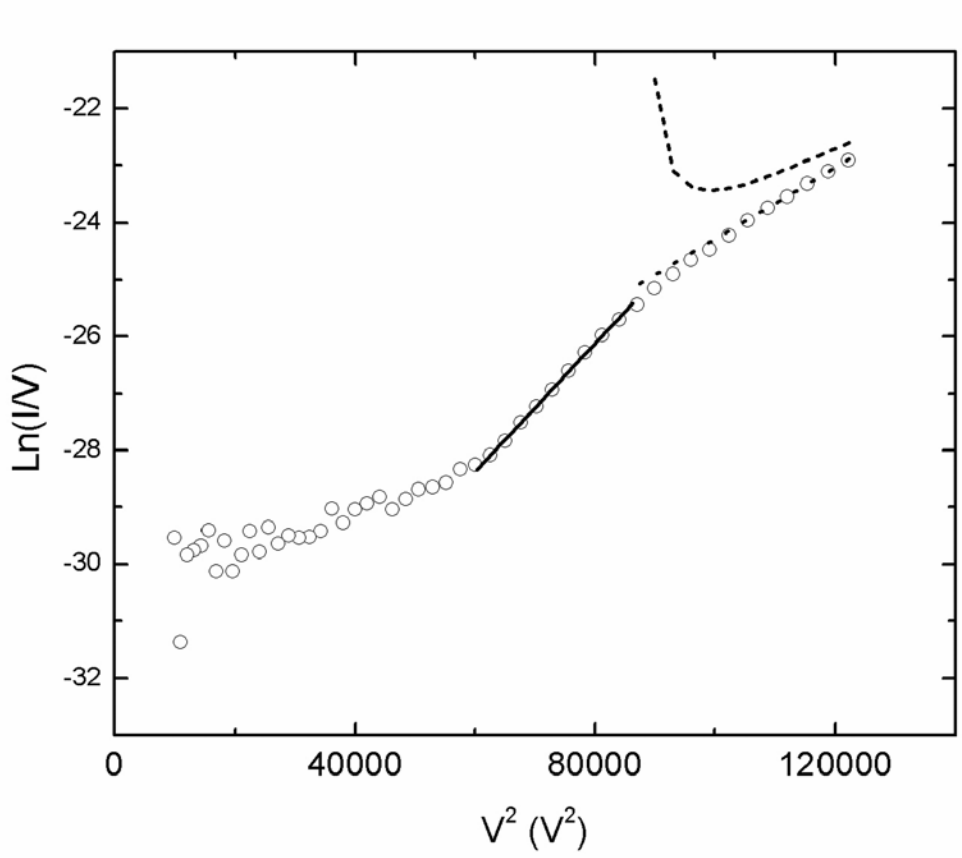

Fig. 5.6.3 Thermal field emission measurement of a single carbon nanotube shown in Fig. 5.5.1. In the Ln(I/V) vs. V^2 plot, hollow circles are the experiment data. Solid line is a linear fit from Eq. (5.6.2). Broken line is calculated from Eq. (2.2.4). The dotted line is a liner fit from Eq. (5.3.19) in the extended intermediate region between 3.5×10^7 V/cm and 4×10^7 V/cm.

where A is the emission area. Eq. (5.6.5) suggests that the emission data follow a straight line with a slope $4.74\times10^{-5}\beta^2/T^3$ in the intermediate region. The temperature at the apex of the carbon nanotube was calculated to be 1770 K using

$$T_{M-G} = (4.74\times10^{-5}\beta^2/slope)^{1/3}. \tag{5.6.6}$$

If this temperature was plugged in the field emission equation which counts the temperature effect:

$$J(T,F,\phi) = J(0,F,\phi)\frac{\pi kT/d}{\sin(\pi kT/d)}, \tag{5.6.7}$$

where

$$d = \frac{heF}{4(2m\phi)^{1/2}t(y)} = \frac{9.76\times10^{-9}F}{\phi^{1/2}t(y)}, \tag{5.6.8}$$

the simulated current density agrees well with experimental results when the electric field is around 4×10^7 V/cm, and where $p = kT/d = 0.9$. A higher accuracy is expected at $p \sim 0.7$. Between 3.5×10^7 V/cm and 4×10^7 V/cm, there is gap which is not covered by the Murphy-Good equation (Eq.(5.6.2)) or field emission equation (Eq. (5.6.7)). As expected from Eq. (5.3.18), the data also follow a linear relationship. The temperature of the carbon nanotube apex is calculated from (Eq. (5.3.19)) and it is 1730 K which agrees well with the calculated values from the Murphy-Good equation. It can be concluded that the electron emission mechanism between the field emission region and the intermediate region is described well by the newly established Eq. (5.3.18).

By measuring field emission at different temperatures, we can experimentally find the intermediate zone boundary. Fig. 5.4.1(b) shows the experimentally measured boundaries by calculating the temperature and finding the field range in which the *Ln(I/V) vs.* V^2 plot follws a linear relationship. The experimentally determined boundary for the intermediate region is

broader than the theoretically predicted one (Fig. 5.4.1(b)).. We also found that Eq. (2.2.11) can be applied up to 2200 K, which is higher than the predicted temperature limit 1800 K. In *Ln(I/V) vs.* V^2 plot, the emission data from both the intermediate region and the extended intermediate region follow a linear relationship.

5.7 Stability of Thermal Field Emission

We have measured the thermal field emission stability of a single carbon nanotube (Fig. 5.5.1). The stability measurements were carried out in a vacuum of 10^{-8} Torr. At each measurement, the temperature of the heating filament was kept constant. The emission temperature was calculated using the method described in Section 5.6.

The emission stability measurement at 1800 K shows a maximum current change (I_{max}-I_{min}) of 2.4 nA. We intentionally kept the emission current at a small value to reduce the risk of structure damage. At 1800 K, 253 current data points were collected and the distribution of current was plotted in Fig. 5.7.2. A Gaussian fit was made and the peak position was found to be 13.3 with a FWHM 0.1 nA. Then the stability (FWHM/peak) is 0.8%. Compared with our best cold field emission current distribution width ~ 3.4 nA (Section 4.6), the current distribution width of thermal field emission at 1800 K is one order of magnitude lower than cold field emission.

The emission stability at 1100 K was also studied. The maximum current change (I_{max}-I_{min}) is 18.7 nA. The Gaussian fit of current distribution shows a FWHM of 4.8 nA. This suggests that the emission stability could be improved by letting the nanotubes emit electrons at a higher temperature between 1700 K and 1800 K.

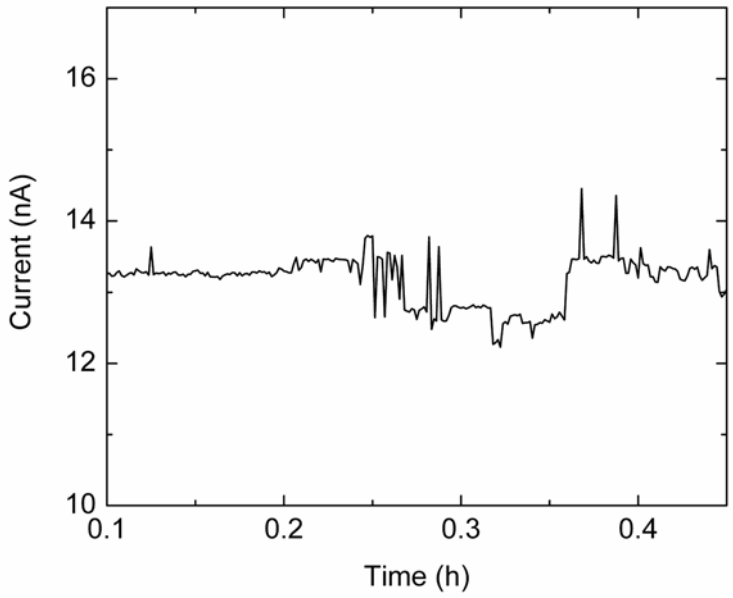

Fig. 5.7.1 Emission current stability measurement showing a maximum current change of 2.4 nA.

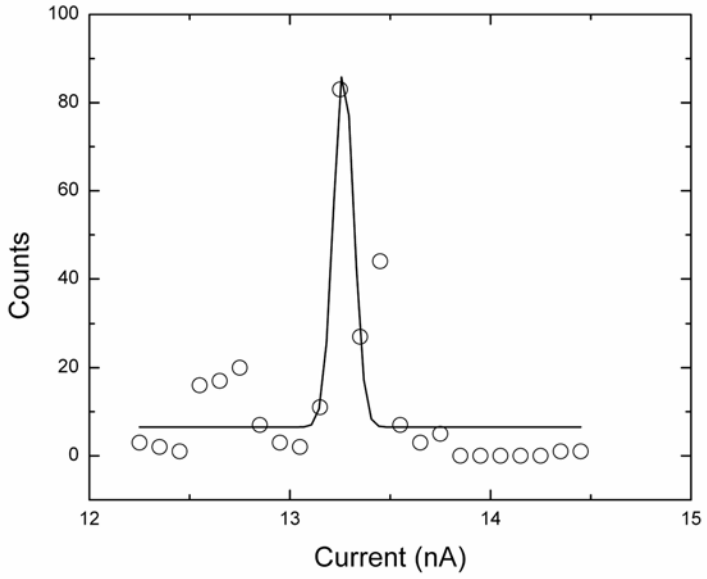

Fig. 5.7.2 Current distribution of 253 data points over 0.35 hours (hollow circles) and a Gaussian fit is indicated by the solid line with a peak position 13.3 nA and FWHM 0.1 nA.

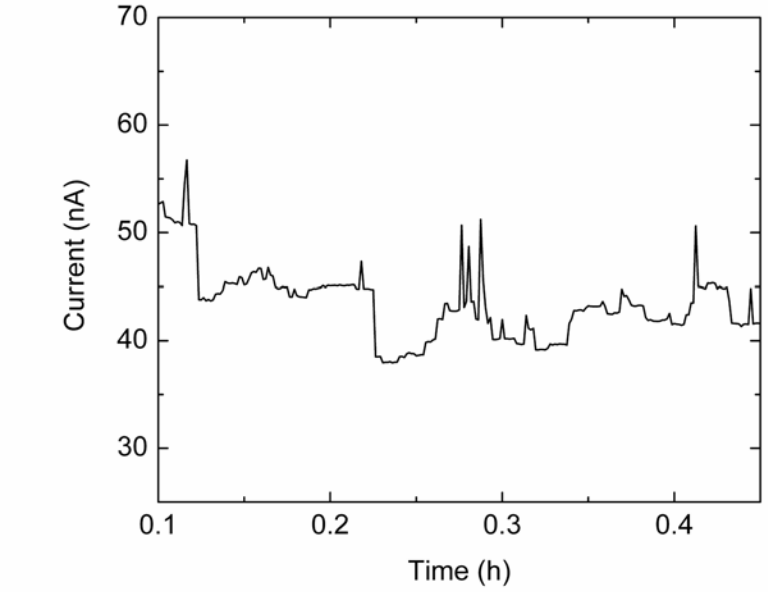

Fig. 5.7.3 Emission current stability measurement showing a maximum current change of 18.7 nA.

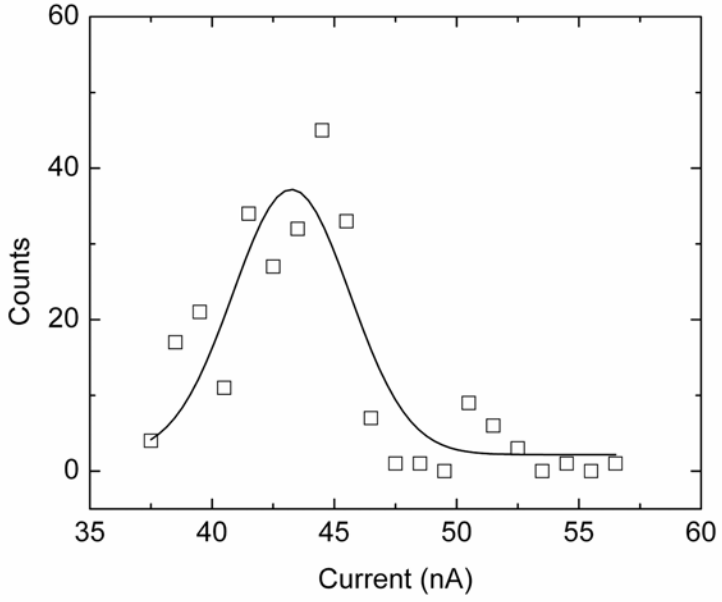

Fig. 5.7.4 Current distribution of 253 data points over 0.35 hour (hollow circles) and a Gaussian fit is indicated by the solid line with a peak position 43.2 nA and FWHM 4.8 nA.

5.8 References

[1] A. Sommerfeld and H. Bethe, *Handbuch der Physik* (Springer-Verlag, Berlin, 1933), Vol. **24**, p. 442.

[2] E. Guth and C. Mullin, *Phys. Rev.* **61,** 339 (1942).

[3] W. W. Dolan and W. P. Dyke, *Phys. Rev.* **95**, 327 (1954).

[4] E. L. Murphy and R. H. Good, JR., *Phys. Rev.* **102**, 1464 (1956).

[5] S. G. Christov, *Phys. Status Solidi* **17**, 11 (1966).

[6] L. W. Swanson and A.E. Bell, in *Advances in Electronics and Electron Physics*, edited by L. Marton (Academic Press, New York and London, 1973), Vol. **32**, p. 303.

[7] S. Iijima, *Nature* **354,** 56 (1991).

[8] N. de Jonge, Y. Lamy, K. Schoots, and T. H. Oosterkamp, *Nature* **420,** 393 (2002).

[9] J. M. Bonard, J. P. Salvetat, T. Stöckli, L. Forró, and A. Châtelain, *Appl. Phys. A* **69,** 245 (1999).

[10] M. J. Fransen, Th. L. Van Rooy, and P. Kruit, *Appl. Surf. Sci.* **164,** 312 (1999).

[11] S. T. Purcel, P. Vincent, C. Journet, and V. T. Binh, *Phys. Rev. Lett.* **88**, 1055021 (2002).

[12] N. de Jonge and J. M. Bonard, *Phil. Trans. R. Soc. Lond. A* **362**, 2239 (2004).

[13] G. Wentzel, *Zeits. Physik* **38**, 518 (1926).

[14] H. A. Kramers, *Zeits. Physik* **39**, 828 (1926).

[15] L. Brillouin, *Comptes Rendus* **183**, 24 (1926).

[16] J. W. Gadzuk and E. W. Plummer, *Rev. Mod. Phys.* **45**, 487 (1973).

[17] E. C. Kemble, *The Fundamental Principles of Quantum Mechanics* (McGraw-Hill, New York, 1952).

[18] S. C. Miller, Jr. and R. H. Good, Jr., *Phys. Rev.* **91**, 174 (1953).

[19] E. L. Murphy and R. H. Good, Jr., *Phys. Rev.* **102**, 1464 (1956).

[20] R. Gao, Z. Pan, and Z. L. Wang, *Appl. Phys. Lett.* **78**, 1757 (2001).

Chapter 6. Field Emission Properties of a Cs-Doped Single Carbon Nanotube

6.1 Introduction and Motivation

Carbon nanotubes have many advantages to serve as a field emission point electron source such as high brightness, low turn-on field, narrow energy distribution, good stability, and long lifetime. Compared with the tungsten cold field emission electron source, one great advantage is that carbon nanotubes do not need to be flashed every two hours and can emit electrons continuously over a few hundred hours [1,2]. Carbon nanotubes can also offer a brightness three orders of magnitude higher than the regular thermionic electrons sources such as the hair pin tungsten and LaB_6. These characteristics make carbon nanotubes a most promising candidate to be used as a point electrons source in high precision analytical instruments such as TEM and SEM [3]. Despite all these excellent field emission properties, carbon nanotubes have a disadvantage that the work function of a carbon nanotube is too high (4.6 - 5 eV) [4,5,6] compared with the low work function materials such as LaB_6 (~ 2.4 eV) [7] and the Schottky emitters (~ 2.8 eV) [8]. From the F-N theory, we can expect that a high work function makes it more difficult for electrons to escape from the potential barrier. More accurately, the relation between current density, electric field and work function is [9,10]:

$$J(T=\mathbf{0},F,\phi)=\mathbf{1.5}\times\mathbf{10}^{-\mathbf{6}}\frac{F^{\mathbf{2}}}{\phi}\exp[\frac{\mathbf{10.4}}{\phi^{\mathbf{1/2}}}]\exp[-\mathbf{6.44}\times\mathbf{10}^{\mathbf{7}}\frac{\phi^{\mathbf{3/2}}}{F}]\ \text{Acm}^{-2} \qquad (6.1.1)$$

for F in V/cm ans ϕ in eV. If we compare the current densities with different work functions under the same electric field, the following relationship can be obtained

$$\frac{J(\phi_1)}{J(\phi_2)} = \frac{\phi_2}{\phi_1}\exp[\mathbf{10.4}\frac{\phi_2^{1/2} - \phi_1^{1/2}}{(\phi_1\phi_2)^{1/2}}]\exp[-\frac{\mathbf{6.44\times10^7}}{F}(\phi_1^{3/2} - \phi_2^{3/2}]. \quad (6.1.2)$$

If the work function of a field emitter is reduced from 5 eV to 3 eV (20%), the current density will increase six orders of magnitude. Reversely, if both emitters want to reach the same current density, a much lower electric field is needed for the low work function emitter.

In order to make carbon nanotubes a better field emitter, a reduction on their work function will be a good option. In 1997, Lee et al. [11] and Rao et al. [12] reported that alkali metal (K and Rb) and halogen (Br_2 and I) doping of SWNT bundles showed an increase in electrical conductivity. Suzuki et al. reported that Alkali metals (K) could be intercalated into the adjacent shells of MWNTs if defects were present [13]. In their work, the valence band excitation spectra showed additional humps which were not observed in the unintercalated nanotubes. Further more, it was found the Cs intercalation reduced the work function of MWNT from 4.4 eV to 2.2 eV [14]. Suzuki et al. also found the Cs intercalation reduced the work function of SWNT bundles from 4.8 eV to 2.4 eV [15] The field emission measurement from a Cs-intercalated SWNT film was done by Wadhawan et al [16], who obtained a similar result as Suzuki et al. [15].

For carbon nanotube bundles, the Cs intercalation may form a bulk Cs metal on the bundle surface. Therefore the electrons may be emitted from the bulk metal instead of carbon nanotube and the measured work function could be the same as Cs. A measurement on a single Cs-doped MWNT will reduce this ambiguity. Although the field emission measurements from a Cs-doped SWNT film have shown that the work function decreased by a factor of 2, it is still not clear how alkali metal doping would change the work function of a

single CNT. In this work, we will fabricate a single CNT emitter and study the field emission properties of single Cs-doped CNT.

6.2 In-situ Cs Doping and Characterization of Field Emission

The detailed procedure to prepare a single nanotube field emitter has been given in Chapter 4. The TEM images of the emitters are shown in Fig. 6.2.1(a) and Fig. 6.2.2(a). A fiber-CNT structure was attached to a 0.1 mm diameter tungsten supporting wire to serve as the cathode. A flat tungsten plate was used as the anode. The whole structure was mounted into a field emission chamber in which a heating circuit was set up. The apparatus is shown schematically in Fig. 6.2.3.

A Cs metal dispenser (from Saes Getters) was used as the Cs source. When the dispenser was heated to above 600°C by letting a 5 A current going through it, the Cs atoms were released from the dispenser. This dispenser was carefully positioned so that the Cs atoms could be deposited on the single nanotube field emitter.

Before the measurement, the field emission chamber was vacuumed and baked for four days. After the vacuum level reached 10^{-8} Torr, the cold field emission measurements were first carried out multiple times to make sure that the I-V curves were reproducible. Then the Cs dispenser was slowly heated up. At the beginning, the vacuum usually became worse ($\sim 10^{-7}$ Torr) due to degassing. After the heating current reached 4.5 A, stop increasing the current and keep it at 4.5 A until the vacuum drops back to 10^{-8} Torr. At this current, the Cs atoms are not released. After the vacuum is stable, the current was increased to 5 A and was

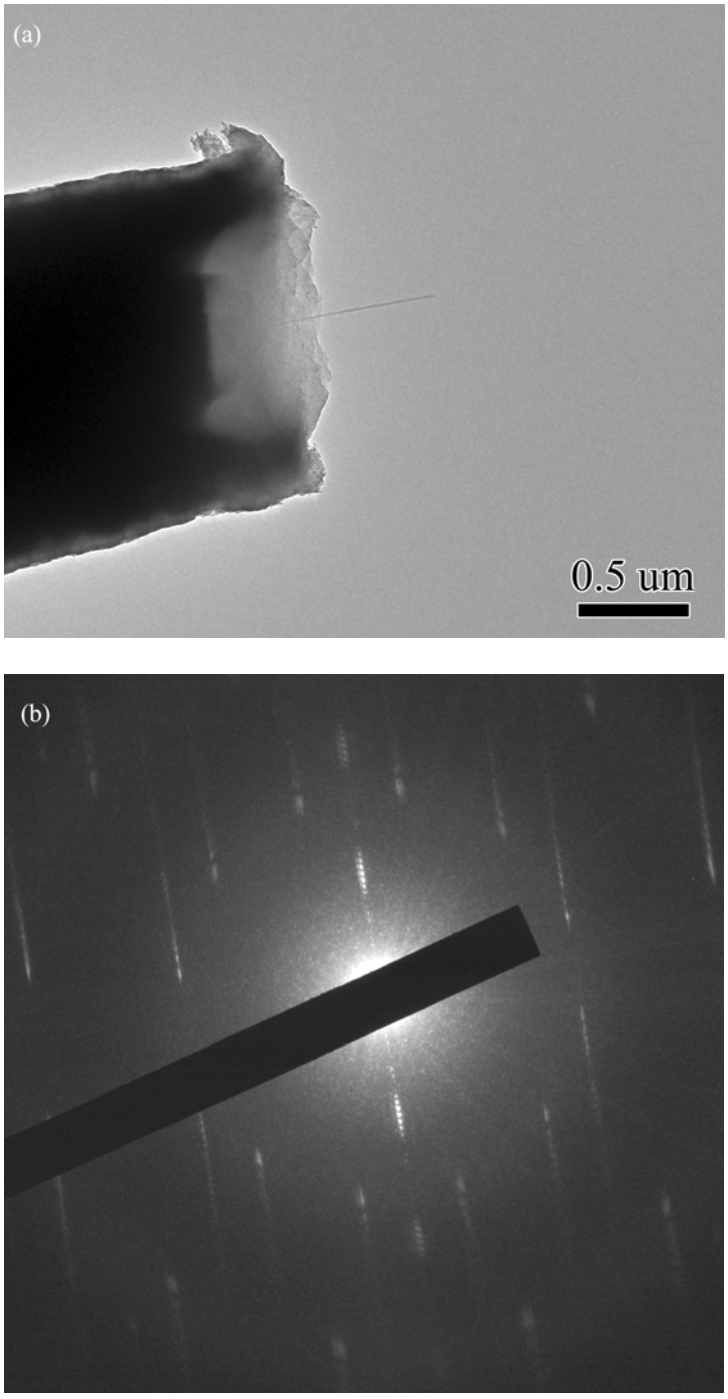

Fig. 6.2.1. (a) Low magnification TEM image of a single MWNT extruding from a carbon fiber with a 1.3 μm diameter. The inner and outer diameter of this MWNT was estimated to be about 4 nm and 8 nm, respectively. (b) The corresponding nanobeam electron diffraction pattern. This pattern suggests all the shells have close v/u ratios.

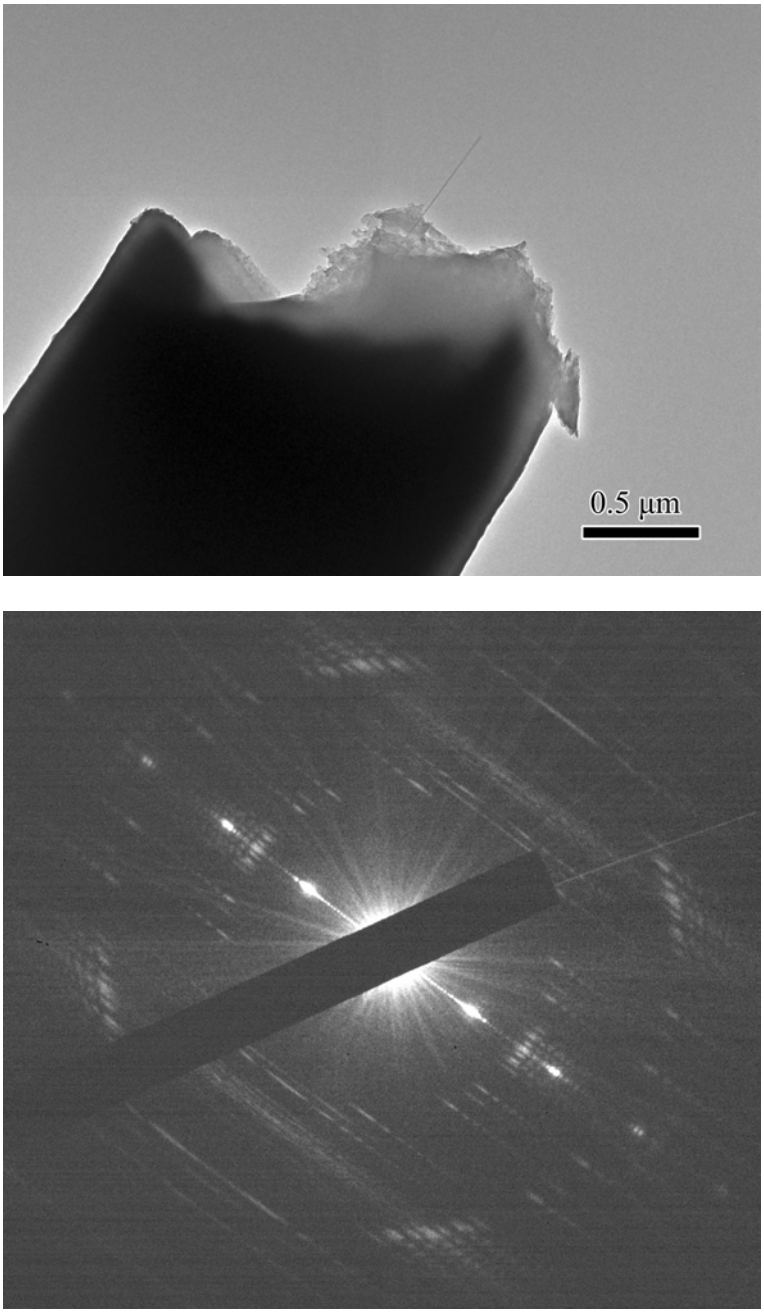

Fig. 6.2.2. (a) Low magnification TEM image of a single MWNT extruding from a carbon fiber with 2.0 μm diameter. The inner and outer diameters of this MWNT are estimated to be about 6 nm and 14 nm, respectively. (b) The corresponding nanobeam electron diffraction pattern. This pattern suggests this carbon nanotube should have more than 10 shells.

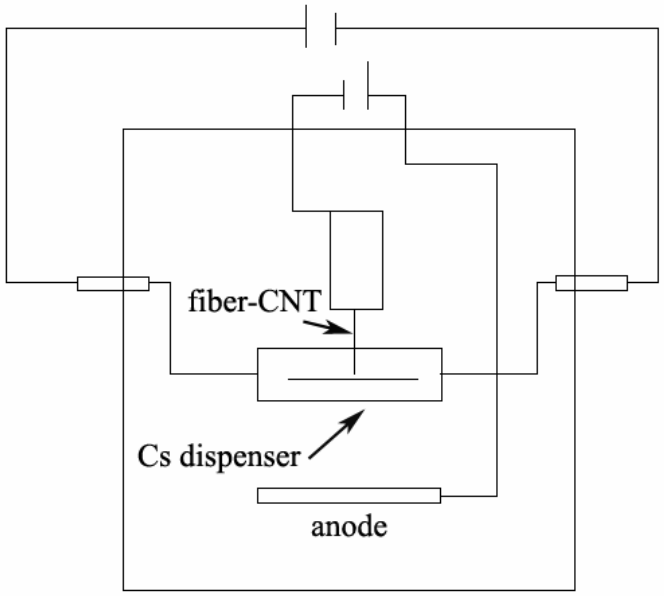

Fig. 6.2.3. Schematic of the Cs doping and field emission measurement apparatus. The fiber-CNT structure is supported by a 0.1 mm tungsten wire. The Cs dispenser is positioned below the CNT and the Cs atoms will be released from the slot indicated by a dark line.

kept at this value for 3 min. Then the heating current was turned off. The emission current was measured as a function of extraction voltage. Then the carbon nanotube was doped with Cs for another 3 min and followed by another measurement of the characteristics of field emission

6.3 Determination of the Carbon Nanotube Structure

The atomic structure of the MWNT in Fig. 6.2.1(a) has been characterized in Chapter 3.4 basing on the nanobeam electron diffraction pattern. The detail structure has been given in Table 6.3.1. The atomic structure of the MWNT shown in Fig. 6.2.2(a) was not characterized due to the fact that it has a large diameter and more than 10 shells. The inner and outer diameter can be estimated to be 6 nm and 14 nm, respectively, from the high magnification TEM images.

Table 6.3.1 Atomic structure of the MWNT shown in Fig. 6.2.1(a) determined from the electron diffraction pattern shown in Fig. 6.2.1(b).

Shell No.	*v*/*u*	(*u*, *v*)	Diameter (nm)	Helicity	Metallicity
1	0.4091	(44, 18)	4.326	16.39°	M
2	0.3846	(52, 20)	5.040	15.61°	S
3	0.3793	(58, 22)	5.606	15.44°	M
4	0.3846	(65, 25)	6.300	15.61°	S
5	0.3889	(72, 28)	6.996	15.75°	S

The work function of a nanotube is still an open question. There are several experimental results available. These experimental results showed a great diversity and sometimes can be controversial.

The local Kelvin Probe method has been used to study the work function of a single carbon nanotube tip [4]. When a gold ball is connected with a nanotube, some static charges will show up at the tip of the nanotube to balance the work function difference. If an oscillating voltage $V_{ac}cos2\pi ft$ is applied to the nanotube, a mechanical resonance can be introduced. A direct voltage V_{dc} is also applied to the nanotube so that the resonance amplitude can be adjusted to zero. The force acting on the nanotube is

$$\begin{aligned} F = \alpha^2\beta\{&[(W_{Au} - W_{NTT} + eV_{dc})^2 + e^2V_{ac}^2/2 \\ &+ 2eV_{ac}(W_{Au} - W_{NTT} + eV_{dc})\cos 2\pi ft \\ &+ e^2V_{ac}^2/2\cos 4\pi ft\}, \end{aligned} \tag{6.3.1}$$

where W_{Au} and W_{NTT} are the work functions of gold and carbon nanotube tip respectively. A resonance happens when the oscillation frequency is approaching the intrinsic resonance frequency f_0 the nanotube. The intrinsic resonance frequency can be obtained as [4]

$$f_0 = \frac{1.875^2}{8\pi}\frac{1}{L^2}\sqrt{\frac{(D^2 + D_1^2)E_b}{\rho}}, \tag{6.3.2}$$

where D is the outer diameter, D_1 is the inner diameter, ρ is the volume density, L is its length, and E_b is the bending modulus of the nanotube. By adjusting V_{dc}, the resonance amplitude can be reduced to zero if the condition $W_{Au} - W_{NTT} + eV_{dc} = 0$ is satisfied. Then the work function of the nanotube tip will be $W_{NTT} = W_{Au} + eV_{dc}$. It showed that 75% MWNTs have a work function around 4.6 - 4.8 eV in the diameter range between 14 nm and 55 nm. Also some high work functions of about 5.5 eV for MWNTs have been observed. It is believed that the high work function is due to their semiconducting electronic structures. But

this is still not clear because, theoretically, a large diameter semiconducting nanotube has a rather small band gap and behaves like a conductor.

Another method to measure the work function of a single nanotube tip is related to the field emission process. During the field emission process, the current can be measured as a function of the extraction voltage and the energy distribution can also be measured at a certain extraction voltage V. From the F-N plot, the slope b

$$b = 6.44 \times 10^{-7} \frac{\phi^{3/2}}{\beta} \tag{6.3.3}$$

is directly related to the field enhancement β and the work function ϕ. Also the energy distribution of the emitted electrons is given by [17]:

$$J(E) = \frac{\mathbf{4}\pi med}{h^{\mathbf{3}}} \frac{\exp[E/d]}{\mathbf{1} + \exp[E/kT]} \tag{6.3.4}$$

with

$$d = 9.76 \times 10^{-11} \frac{eF}{(\phi/e)^{1/2}}, \tag{6.3.5}$$

where e is electric charge of the electron, k is Boltzmann constant, F is electric field, and E is the energy of electrons. The parameter d can be obtained by fitting the energy spectrum. Combining Eq. (6.3.3) and Eq. (6.3.5), the work function from the tip of a single carbon nanotube can be obtained as [5]:

$$\phi = -1.64 \frac{bd}{V}, \tag{6.3.6}$$

where V is the extraction voltage at which the energy spectrum is measured. By this method de Jonge has measured the work functions from several single nanotubes and the results are 5.1 ± 0.2 eV. The nanotubes that de Jonge measured have rather small diameters (2 - 4 nm) [5].

The ultraviolet photoemission spectroscopy has also been used to study the work functions of SWNT bundles and MWNTs. In most cases, these results are the work functions of the nanotubes' sidewalls. Suzuki et al. have studied the work functions from a aligned MWNT film. In their work [6], the work function from MWNTs was determined to be 4.6 eV. This was an average value over a large number of MWNTs. They also found that the work function of aligned MWNTs was 4.4 eV. The work function of SWNT has also been studied by this method and was found to be around 4.8 eV, which is larger than the work function of MWNTs [14].

Zhao et al. have reported a comprehensive calculation of the work functions of carbon nanotubes and bundles by the generalized gradient approximation (GGA) method [18]. Zhao et al found that the work functions of metallic nanotubes were independent on the chirality. The work functions of both zigzag and armchair nanotubes follow the same linear relationship with the inverse of diameter

$$W = -\frac{0.104}{D} + 4.83 \text{ eV} \tag{6.3.7}$$

for D in Å. The work function of semiconducting SWNTs is higher than the metallic ones when the Fermi level is put at the top of the valence band. It decreases linearly with 1/D and reach a limit of 4.73 eV at $D \rightarrow \infty$. This strong dependence on nanotube diameter is attributed to the decrease of the band gap with the tube diameter [19]. If the Fermi level is put at the middle of the band gap, then the dependence of work function on diameter for semiconducting nanotubes will be weak.

Another group calculated the work functions of SWNTs using the local density approximation (LDA). They found that the work functions for SWNTs of diameter larger than 1 nm are 4.66 eV for both metallic and semiconducting SWNTs [19].

In our case, the outermost shell has a diameter 6.996 nm and is determined to be semiconducting. A 4.8 eV work function is assigned to the whole nanotube by considering the theoretically predicted value and experimentally measured results. We believe the error will be less than 0.2 eV. Practically, the work functions also depend on the tip morphology and cleanness [21]. Recently, it was reported that amorphous carbon present at a nanotube tip can reduce the work function by 0.2 eV [20].

6.4 Results and Discussion

Field emission measurements were carried out on the nanotubes shown in Fig. 6.2.1(a) and Fig. 6.2.1(a) at room temperature. The Fowler-Nordheim (F-N) theory describes the field emission process by giving the relationship between the current density through a potential barrier and the applied voltage and the metal surface work function:

$$J(T=\mathbf{0},F,\phi)=\mathbf{1.5}\times\mathbf{10}^{-\mathbf{6}}\frac{F^{\mathbf{2}}}{\phi}\exp[\frac{\mathbf{10.4}}{\phi^{\mathbf{1/2}}}]\exp[-\mathbf{6.44}\times\mathbf{10}^{\mathbf{7}}\frac{\phi^{\mathbf{3/2}}}{F}], \tag{6.4.1}$$

and

$$F=\beta V, \tag{6.4.2}$$

where ϕ is the work function and β is the field enhancement factor. In an F-N plot, the slope is simply $-6.44\times10^{7}\phi^{3/2}/\beta$. Since the field enhancement factor β is constant, the slope of the F-N plot is only proportional to $\phi^{3/2}$. By comparing the slope of the F-N plot from a Cs-doped carbon nanotube with clean nanotubes, the work function of the doped carbon nanotube can be obtained. First, the field emission was measured three times to ensure that the F-N plot is reproducible. All three measurements agree very well and give a

field enhancement factor 5.4×10^6 m^{-1} and 3.3×10^6 m^{-1}, respectively, with a 4.8 eV work function.

Due to its extremely small dimensions, it is hard to precisely measure the concentration of the Cs concentration on the carbon nanotube. Here we used the deposition time to indicate the concentration of Cs. Several sets of field emission data at different deposition times (5 min, 20 min) were plotted as $Ln(I/V^2)$ *vs.* $1/V$ to allow a comparison with the undoped nanotube (Fig. 6.4.1(a)). As the deposition time increased, the slopes of the F-N plots dropped dramatically, indicating that the work function had been reduced. The ratio of slope for undoped nanotube and the slope for the nanotube exposed to Cs for 20 min is 1.43. Since the predicted work function for the clean MWNT is 4.8 eV, then after 20 min deposition of Cs, the work function of this nanotube was reduced to 3.78 eV. We also measured the work function of another Cs-doped MWNT, the work function was reduced from 4.8 eV to 3.7 eV (Fig. 6.4.1(b)). We have noticed that this result was different from the result reported in Reference 14. Our result is slight higher than the theoretically predicted work function of 3.4 eV for the Cs intercalated carbon nanotube bundles [18] and 60% larger than the experimental result 2.2 eV for the Cs-intercalated SWNT bundles [14].

In the process of Cs doping, we believe that the Cs atoms were mostly deposited on the outer wall and the tip of the carbon nanotube. From the charge transfer theory, the Fermi energy of the MWNT will be shifted 1.1 eV toward to the vacuum level. Although the outer shell is semiconducting, the small band gap due to its large diameter can still make this shell emit electrons like conductors. The band gap of a single walled nanotube is $E_g = 2\gamma_0 a_{C-C}/d$, where $\gamma_0 = 3 \;\; eV$ and a_{C-C} is nearest neighbour C-C distance (0.142 nm) [19]. For the outermost shell, $E_g = 0.12 \;\; eV$, which is comparable to the thermal energy of

the electrons at the room temperature [21]. Experimentally, the electron emission from this nanotube follows the F-N theory.

In conclusion, the atomic structure of a five-wall carbon nanotube has been identified. The work function for this nanotube has been predicted to be 4.8 eV basing on GGA calculation and experimental results. The Cs deposition on a single MWNT has a significant effect on the field emission properties. We found that the work function of this nanotube was reduced from 4.8 eV to 3.78 eV and 3.7 eV, respectively, due to the Cs doping.

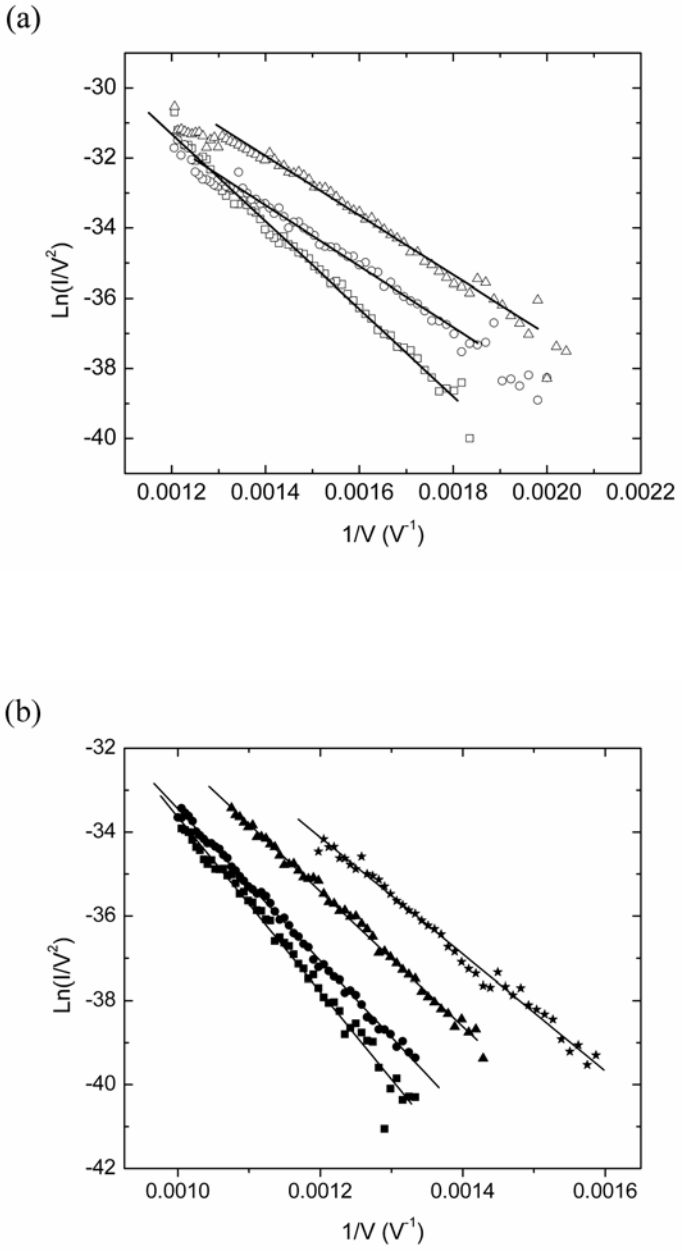

Fig. 6.4.1. (a) F-N plots of the electron emission data from the single MWNT (Fig. 6.2.1(a)) at different deposition time (squares - undoped nanotube, circles - 5 min doping, and triangles – 20 min doping). (b) F-N plots of the electron emission data from the single MWNT (Fig. 6.2.2(a)) at different deposition time (solid squares – undoped nanotube, solid circles – 5 min doping, solid triangles – 8 min doping, solid stars – 15 min doping).

6.5 References

[1] K. A. Dean and B. R. Chalamala, *Appl. Phys. Lett.* **75**, 3071 (1999).

[2] N. de Jonge and J. M. Bonard, *Phil. Trans. R. Soc. Lond. A* **362,** 2239 (2004).

[3] N. de Jonge, Y. Lamy, K. Schoots, and T. H. Oosterkamp, *Nature* **420**, 393 (2002).

[4] R.Gao, Z. Pan, and Z. L. Wang, *Appl. Phys. Lett.* **78**, 1757 (2001).

[5] N. de Jonge, M. Allioux, M. Doytcheva, and M. Kaiser, *Appl. Phys. Lett.* **85**, 1607 (2004).

[6] S. Suzuki, Y. Watanabe, T. Kiyokura, K. G. Nath, and T. Ogino, *Phys. Rev. B* **63**, 245418 (2001).

[7] J. M. Lafferty, *J. Appl. Phys.* **22**, 299 (1951).

[8] L. W. Swanson and N. A. Martin, *J. Appl. Phys.* **46**, 2029 (1975).

[9] R. H. Fowler and L. W. Nordheim, *Proc. Roy. Soc. Lond. A* **119**, 173 (1928).

[10] I. Brodie and C. A. Spindt, *Advances in Electronics and Electron Physics* (Academic Press, San Diego, 1992), Vol. **83**, p. 11.

[11] R. S. Lee, H. J. Kim, J. E. Fischer, A. Thess, and R. E. Smalley, *Nature* **388**, 255 (1997).

[12] A. M. Rao, P. C. Eklund, S. Bandow, A. Thess, and R. E. Smalley, *Nature* **388,** 257 (1997).

[13] S. Suzuki and M. Tomita, *J. Appl. Phys.* **79,** 3739 (1995).

[14] S. Suzuki, Y. Watanabe, T. Kiyokura, K. G. Nath, T. Ogino, S. Heun, W. Zhu, C. Bower, and O. Zhou, *Surf. Rev. Lett.* **9**, 431 (2002).

[15] S. Suzuki, C. Bower, Y. Watanabe, and O. Zhou, *Appl. Phys. Lett.* **76**, 4007 (2000).

[16] A. Wadhawan, R.E. Stallcup, and J. M. Perez, *Appl. Phys. Lett.* **78**, 108 (2001).

[17] J. W. Gadzuk, *Phys. Rev. B* **1**, 2110 (1970).

[18] J. J. Zhao, J. Han, and J. P. Lu, *Phys. Rev. B* **65**, 193401 (2002).

[19] M. S. Dresselhaus and P. C. Eklund, *Adv. Phys.* **49**, 705 (2000).

[20] B. Shan and K. Cho, *Phys. Rev. Lett.* **94**, 236602 (2005).

[21] Z. Xu, X. D. Bai, E. G. Wang, and Z. L. Wang, *Appl. Phys. Lett.* **87**, 163106 (2005).

Chapter 7. Summary and Conclusions

No doubt carbon nanotubes are one of the most fascinating materials. This nano-metric dimension 1D material has shown great potential in future nanoelectronics applications. Many research efforts have been devoted to this field and we are glad to be part of it.

Fabrication

One obstacle to large scale deployment of carbon nanotubes in applications is that it is very hard to handle due to their small dimensions. In this work, we have used a two-step CVD method to fabricate single carbon nanotubes. By this method, a single carbon nanotube is grown in the core of a micron-size carbon fiber, which has good conductivity. This fiber-CNT structure is easy to handle and can be used in many applications such as the field emission point electron source. This two-step CVD method can be used to synthesize single MWNT field emitters in large scale. More than 10000 carbon fibers with a single MWNT wrapped in the core can be grown on a 1×1 cm^2 alumina plate.

Structure Characterization

The structure characterization was carried out with multiple methods including SEM, TEM, NBD and FEM. The SEM method has been used to reveal the cross section of the fiber. The

carbon fiber is composed of a multi-layer structure. A single carbon nanotube extrudes from the core of the carbon fibers. HRTEM imaging revealed that the carbon layers wrapping the CNT are made of many nanometer-size graphite domains of different orientations, which are connected by amorphous carbon. The HRTEM images also revealed that the nanotubes usually have two shells to more than 20 shells. A diameter distribution has been obtained with a peak at about 6 nm. About 70% of the nanotubes have a diameter less than 10 nm. Due to the high synthesis temperature, the nanotube side-walls have good crystallinity, which will improve the emission lifetime. To achieve a high brightness, the nanotube length needs to be controlled to reduce the thermal vibrations. In this work, we have developed an in-situ cutting technique to control the nanotube length. In a JEM-2010F TEM (operated at 200 KV with a field emission gun), a very fine high energy electron probe (7 Å diameter) was used to cut the MWNTs. We also used the NBD method to determine the atomic structure of MWNT even without HRTEM images. With a small condenser aperture, a fine and parallel electron beam has been formed and used to illuminate the MWNT. The NBD diffraction patterns composed of discrete layer lines were obtained. The atomic structure was determined from the layer line spacings and the scattering intensities. The atomic structure of a five-wall carbon nanotube has been determined and the field emission properties of this nanotube also have been measured.

Electron Emission from a Single Carbon Nanotube

We have tested the field emission properties of these fiber-CNT structures. The I-V curves measured from a single nanotube follows the F-N theory. The maximum current we extracted from a single nanotube is between 3 μA to 4 μA. An empirical model has been developed to

estimate the field enhancement factor of the fiber-CNT structure. The lifetime stability measurement shows that this structure can emit electrons at 370 nA for more than 100 hours without significant current drops. The best stability is 3.6% drift per hour. A current distribution in 1 hour has also been obtained. The Gaussian fit shows that this current distribution has a peak at 387 nA and has an FWHM of 3.4 nA. The maximum brightness measured from a single carbon nanotube is 2.9×10^{8} $ASr^{-1}m^{-2}V^{-1}$. A higher value is expected with a better alignment.

We have re-examined the thermal field emission theory and found that a gap between field the emission zone and the intermediate region has not been covered by either the F-N theory or the Murphy-Good theories. We have developed a new equation to describe the current density dependence on the electric field, temperature and work function. Further more, we have proved this equation by measuring the thermal field emission from a single MWNT. The experimental results agree well with the newly developed equation. At the same time, the boundary of the intermediate region was experimentally determined and compared with the theoretically predicted one. We have also measured the thermal field emission stability, which has much smaller fluctuations comparing with the cold field emitters.

To make carbon nanotube a better field emitter, we have successfully reduced its work function from 4.8 eV to 3.7 eV by depositing Cs atoms on the the sidewall and tip of a single five-wall carbon nanotube. This doping process has also reduced the turn-on field of the doped carbon nanotubes.

In conclusion, we have accomplished the fabrication of single carbon nanotube field emitters. Detailed structure characterization has been performed using on multiple techniques including SEM, TEM, NBD and FEM. We determined the atomic structure of a five-wall

nanotube using the NBD method. Finally both the cold field emission properties and the thermal field emission properties of this fiber-CNT structure have been studied. We have also doped the single CNTs to enhance the field emission properties of the fiber-CNT structure. Through this work, we show that the fiber-CNT structure can be used in high precision analytical instruments such as the TEM and SEM, where high brightness electron point source is required.

Appendix A. Table of Functions *v(y)*, *s(y)*, *t(y)*, and *Θ(y)*

Table I. Values of function *v(y)*.

y	*v(y)*	*y*	*v(y)*	*y*	*v(y)*
0.00	1.00000	0.34	0.84057	0.67	0.48967
0.01	0.99973	0.35	0.83234	0.68	0.47671
0.02	0.99903	0.36	0.82395	0.69	0.46362
0.03	0.99795	0.37	0.81539	0.70	0.45041
0.04	0.99652	0.38	0.80668	0.71	0.43708
0.05	0.99477	0.39	0.79780	0.72	0.42362
0.06	0.99272	0.40	0.78876	0.73	0.41005
0.07	0.99037	0.41	0.77957	0.74	0.39635
0.08	0.98774	0.42	0.77021	0.75	0.38253
0.09	0.98484	0.43	0.76071	0.76	0.36859
0.10	0.98168	0.44	0.75105	0.77	0.35454
0.11	0.97827	0.45	0.74124	0.78	0.34036
0.12	0.97460	0.46	0.73128	0.79	0.32607
0.13	0.97070	0.47	0.72117	0.80	0.31166
0.14	0.96655	0.48	0.71092	0.81	0.29714
0.15	0.96218	0.49	0.70051	0.82	0.28250
0.16	0.95759	0.50	0.68997	0.83	0.26775
0.17	0.95277	0.51	0.67928	0.84	0.25288
0.18	0.94774	0.52	0.66845	0.85	0.23790
0.19	0.94249	0.53	0.65747	0.86	0.22280
0.20	0.93704	0.54	0.64636	0.87	0.20760
0.21	0.93138	0.55	0.63511	0.88	0.19228
0.22	0.92552	0.56	0.62372	0.89	0.17685
0.23	0.91946	0.57	0.61220	0.90	0.16131
0.24	0.91321	0.58	0.60054	0.91	0.14567
0.25	0.90677	0.59	0.58874	0.92	0.12991
0.26	0.90013	0.60	0.57681	0.93	0.11404
0.27	0.89331	0.61	0.56475	0.94	0.09807
0.28	0.88631	0.62	0.55256	0.95	0.08199
0.29	0.87913	0.63	0.54024	0.96	0.06580
0.30	0.87176	0.64	0.52779	0.97	0.04951
0.31	0.86422	0.65	0.51521	0.98	0.03311
0.32	0.85651	0.66	0.5025	0.99	0.01661
0.33	0.84862			1.00	0.00000

Table II. Values of function *s(y)*.

y	*s(y)*	*y*	*s(y)*	*y*	*s(y)*
0.00	1.00000	0.34	0.97896	0.67	0.92173
0.01	0.99998	0.35	0.97773	0.68	0.91948
0.02	0.99993	0.36	0.97647	0.69	0.91721
0.03	0.99983	0.37	0.97518	0.70	0.91490
0.04	0.99970	0.38	0.97385	0.71	0.91257
0.05	0.99953	0.39	0.97249	0.72	0.91021
0.06	0.99933	0.40	0.97110	0.73	0.90782
0.07	0.99908	0.41	0.96967	0.74	0.90540
0.08	0.99880	0.42	0.96822	0.75	0.90296
0.09	0.99849	0.43	0.96673	0.76	0.90049
0.10	0.99813	0.44	0.96521	0.77	0.89798
0.11	0.99774	0.45	0.96365	0.78	0.89546
0.12	0.99732	0.46	0.96207	0.79	0.89290
0.13	0.99685	0.47	0.96045	0.80	0.89032
0.14	0.99635	0.48	0.95881	0.81	0.88771
0.15	0.99582	0.49	0.95713	0.82	0.88507
0.16	0.99525	0.50	0.95542	0.83	0.88240
0.17	0.99464	0.51	0.95368	0.84	0.87971
0.18	0.99400	0.52	0.95191	0.85	0.87699
0.19	0.99332	0.53	0.95011	0.86	0.87425
0.20	0.9926	0.54	0.94827	0.87	0.87147
0.21	0.99185	0.55	0.94641	0.88	0.86867
0.22	0.99107	0.56	0.94452	0.89	0.86585
0.23	0.99025	0.57	0.94259	0.90	0.86300
0.24	0.98939	0.58	0.94064	0.91	0.86012
0.25	0.98850	0.59	0.93866	0.92	0.85721
0.26	0.98758	0.60	0.93664	0.93	0.85428
0.27	0.98662	0.61	0.93460	0.94	0.85132
0.28	0.98563	0.62	0.93253	0.95	0.84834
0.29	0.9846	0.63	0.93043	0.96	0.84533
0.30	0.98354	0.64	0.92830	0.97	0.84230
0.31	0.98245	0.65	0.92614	0.98	0.83924
0.32	0.98132	0.66	0.92395	0.99	0.83615
0.33	0.98016			1.00	0.83300

Table III. Values of function *t(y)*.

y	*t(y)*	*y*	*t(y)*	*y*	*t(y)*
0.00	1.00000	0.34	1.02509	0.67	1.06575
0.01	1.00006	0.35	1.02620	0.68	1.06708
0.02	1.00022	0.36	1.02731	0.69	1.06840
0.03	1.00046	0.37	1.02844	0.70	1.06973
0.04	1.00076	0.38	1.02957	0.71	1.07107
0.05	1.00112	0.39	1.03072	0.72	1.07241
0.06	1.00153	0.40	1.03188	0.73	1.07375
0.07	1.00199	0.41	1.03304	0.74	1.07509
0.08	1.00249	0.42	1.03422	0.75	1.07643
0.09	1.00304	0.43	1.03540	0.76	1.07778
0.10	1.00362	0.44	1.03659	0.77	1.07913
0.11	1.00424	0.45	1.03779	0.78	1.08049
0.12	1.00489	0.46	1.03900	0.79	1.08184
0.13	1.00557	0.47	1.04021	0.80	1.08320
0.14	1.00629	0.48	1.04144	0.81	1.08456
0.15	1.00703	0.49	1.04267	0.82	1.08592
0.16	1.00780	0.50	1.04390	0.83	1.08729
0.17	1.00860	0.51	1.04515	0.84	1.08865
0.18	1.00942	0.52	1.04639	0.85	1.09002
0.19	1.01026	0.53	1.04765	0.86	1.09139
0.20	1.01112	0.54	1.04891	0.87	1.09276
0.21	1.01201	0.55	1.05018	0.88	1.09414
0.22	1.01292	0.56	1.05145	0.89	1.09551
0.23	1.01384	0.57	1.05273	0.90	1.09689
0.24	1.01479	0.58	1.05401	0.92	1.09965
0.26	1.01673	0.60	1.05659	0.93	1.10103
0.27	1.01772	0.61	1.05788	0.94	1.10241
0.28	1.01874	0.62	1.05919	0.95	1.10379
0.29	1.01976	0.63	1.06049	0.96	1.10517
0.30	1.02080	0.64	1.06180	0.97	1.10656
0.31	1.02185	0.65	1.06311	0.98	1.10795
0.32	1.02292	0.66	1.06443	0.99	1.10933
0.33	1.02400			1.00	1.11070

Table IV. Values of function $\Theta(y)$.

y	$\Theta(y)$	y	$\Theta(y)$	y	$\Theta(y)$
0.00	1.00000	0.34	1.29425	0.67	1.83222
0.01	1.00054	0.35	1.30837	0.68	1.85001
0.02	1.00195	0.36	1.32267	0.69	1.86785
0.03	1.00410	0.37	1.33717	0.70	1.88573
0.04	1.00694	0.38	1.35185	0.71	1.90365
0.05	1.01042	0.39	1.36670	0.72	1.92161
0.06	1.01449	0.40	1.38172	0.73	1.93961
0.07	1.01913	0.41	1.39690	0.74	1.95764
0.08	1.02431	0.42	1.41224	0.75	1.97570
0.09	1.03001	0.43	1.42773	0.76	1.99379
0.10	1.03620	0.44	1.44336	0.77	2.01190
0.11	1.04287	0.45	1.45913	0.78	2.03004
0.12	1.04999	0.46	1.47504	0.79	2.04821
0.13	1.05755	0.47	1.49108	0.80	2.06639
0.14	1.06553	0.48	1.50724	0.81	2.08460
0.15	1.07392	0.49	1.52352	0.82	2.10282
0.16	1.08269	0.50	1.53992	0.83	2.12105
0.17	1.09185	0.51	1.55642	0.84	2.13930
0.18	1.10137	0.52	1.57303	0.85	2.15756
0.19	1.11124	0.53	1.58975	0.86	2.17583
0.20	1.12145	0.54	1.60656	0.87	2.19410
0.21	1.13199	0.55	1.62346	0.88	2.21238
0.22	1.14285	0.56	1.64045	0.89	2.23067
0.23	1.15401	0.57	1.65753	0.90	2.24896
0.24	1.16547	0.58	1.67469	0.91	2.26725
0.25	1.17721	0.59	1.69193	0.92	2.28554
0.26	1.18923	0.60	1.70924	0.93	2.30383
0.27	1.20152	0.61	1.72662	0.94	2.32212
0.28	1.21406	0.62	1.74407	0.95	2.34040
0.29	1.22685	0.63	1.76159	0.96	2.35868
0.30	1.23988	0.64	1.77916	0.97	2.37695
0.31	1.25315	0.65	1.79679	0.98	2.39521
0.32	1.26664	0.66	1.81448	0.99	2.41347
0.33	1.28034			1.00	2.43180